Transitions in Eruption Style at Silicic Volcanoes:

From Stable Domes to Pyroclastic Flows and Explosive Plumes

by

Brett B. Carr

A Dissertation Presented in Partial Fulfillment
of the Requirements for the Degree
Doctor of Philosophy

Approved July 2016 by the
Graduate Supervisory Committee:

Amanda Clarke, Chair
Ramón Arrowsmith
Allen McNamara
Manoochehr Shirzaei
Stanley Williams

ARIZONA STATE UNIVERSITY

August 2016

ABSTRACT

Silicic volcanoes produce many styles of activity over a range of timescales. Eruptions vary from slow effusion of viscous lava over many years to violent explosions lasting several hours. Hazards from these eruptions can be far-reaching and persistent, and are compounded by the dense populations often surrounding active volcanoes. I apply and develop satellite and ground-based remote sensing techniques to document eruptions at Merapi and Sinabung Volcanoes in Indonesia. I use numerical models of volcanic activity in combination with my observational data to describe the processes driving different eruption styles, including lava dome growth and collapse, lava flow emplacement, and transitions between effusive and explosive activity.

Both effusive and explosive eruptions have occurred recently at Merapi volcano. I use satellite thermal images to identify variations during the 2006 effusive eruption and a numerical model of magma ascent to explain the mechanisms that controlled those variations. I show that a nearby tectonic earthquake may have triggered the peak phase of the eruption by increasing the overpressure and bubble content of the magma and that the frequency of pyroclastic flows is correlated with eruption rate. In 2010, Merapi erupted explosively but also shifted between rapid dome-building and explosive phases. I explain these variations by the heterogeneous addition of CO_2 to the melt from bedrock under conditions favorable to transitions between effusive and explosive styles.

At Sinabung, I use photogrammetry and satellite images to describe the emplacement of a viscous lava flow. I calculate the flow volume (0.1 km^3) and average effusion rate (4.4 $m^3 s^{-1}$) and identify active regions of collapse and advance. Advance rate was controlled by the effusion rate and the flow's yield strength. Pyroclastic flow

activity was initially correlated to the decreasing flow advance rate, but was later affected by the underlying topography as the flow inflated and collapsed near the vent, leading to renewed pyroclastic flow activity.

This work describes previously poorly understood mechanisms of silicic lava emplacement, including multiple causes of pyroclastic flows, and improves the understanding, monitoring capability, and hazard assessment of silicic volcanic eruptions.

DEDICATION

To my parents, for giving me a lifelong passion

for adventures and asking questions

ACKNOWLEDGMENTS

I first must acknowledge my advisor, Dr. Amanda Clarke, for her guidance and encouragement throughout my graduate studies. My path toward completing this dissertation was filled with intriguing side projects that would become their own chapters. I appreciate that Dr. Clarke allowed me the freedom to develop my own ideas and motivated me to pursue them. I also thank the other members of my committee- Dr. Allen McNamara, Dr. Ramón Arrowsmith, Dr. Manoochehr Shirzaei, and Dr. Stan Williams- for numerous helpful discussions and also for teaching some of my favorite courses at ASU. Dr. Arrowsmith was especially helpful in introducing me to Structure-from-Motion and its vast potential- I'm still sorry I crashed your drone into a volcano. Dr. Loÿc Vanderkluysen has been a valuable friend, mentor, and co-author throughout my work- thanks for introducing me to thermal remote sensing and hanging out at Sinabung with me. I must also thank Dr. Mattia de' Michieli Vitturi for his patience and support.

My summer salary in 2013, 2014, and 2015 and my fieldwork in Indonesia in 2014 was supported in part by summer Ph.D. student research fellowships awarded by the School of Earth and Space Exploration (SESE) and funded by a Graduate College University Block Grant at Arizona State University. The Sinabung Volcano Observatory offered useful field assistance and generously shared data and resources. The Badan Informasi Geospasial and the Center for Volcanology and Geological Hazard Management (CVGHM) in Indonesia provided the base DEM I use in this study. Specifically I must thank Anjar Heriwaseso at CVGHM for his assistance during my time

in Indonesia. The field campaign was facilitated and enhanced by a memorandum of understanding between SESE and the Department of Geologic Engineering at the Universitas Gadjah Mada, and specifically the assistance of Dr. Agung Harijoko. Bima Eko Dhanu was invaluable as a field assistant and translator for two weeks while I was in Sumatra. I also thank SESE undergraduate student Cassandra Collins for assistance with MODIS image acquisition.

I was fortunate to have the support of many friends and fellow graduate students in SESE during my time at ASU. Thanks for the venting, the inspiration, and the understanding. Thank you specifically to my current and former research group members Kirsten, Jean-François, Chelsea, Alexa, and Fabrizio, for sharing in this experience and everything that entails and for loving volcanoes. Thank you ASU Ultimate, for letting me run around for a few hours each week and reminding me to have fun. Finally, I have to thank my fiancé Kristen, you kept me sane, you made anything seem possible, and were relentlessly positive when I needed it most. I could not have done this without you.

TABLE OF CONTENTS

Page

LIST OF TABLES x

LIST OF FIGURES xi

CHAPTER

1 INTRODUCTION 1

2 THE 2006 LAVA DOME ERUPTION OF MERAPI VOLCANO (INDONESIA): DETAILED ANALYSIS USING MODIS TIR 14

2.1 Introduction 15

2.1.1 Recent Merapi Activity 16

2.1.2 Satellite Thermal Remote Sensing 18

2.2 Methods 20

2.2.1 Acquisition of MODIS Images 20

2.2.2 Extrusion Rate Estimate From Thermal Radiance 21

2.2.3 Novel Analysis of Pixel Radiances 25

2.2.4 ASTER Images 27

2.3 Results 28

2.4 Discussion 32

2.5 Conclusions 36

3 EXTRUSION RATE VARIATIONS DURING DOME-FORMING ERUPTIONS: A NUMERICAL MODEL APPROACH TO THE 2006 ERUPTION OF MERAPI VOLCANO (INDONESIA) 50

3.1 Introduction 51

CHAPTER Page

3.1.1 Merapi's Activity 52

3.1.2 Numerical Modeling of Volcanic Conduits 54

3.2 Methods 55

3.3 Results 61

3.4 Discussion 63

3.5 Conclusions 67

4 VOLCANIC CONDUIT CONDITIONS CONTROLLING EFFUSIVE-EXPLOSIVE TRANSITIONS WITH APPLICATION TO THE 2010 ERUPTION OF MERAPI VOLCANO (INDONESIA) 76

4.1 Introduction 77

4.1.1 Transitions Between Explosive and Effusive Activity 78

4.1.2 Recent Merapi Activity 79

4.2 Methods 81

4.3 Results 85

4.4 Discussion 90

4.4.1 Transitions Between Distinct Eruptions 90

4.4.2 Transitions During Eruptions 91

4.4.3 Transitions at Merapi in 2010 92

4.5 Conclusions 94

CHAPTER Page

5 THE EMPLACEMENT OF THE ACTIVE LAVA FLOW AT SINABUNG VOLCANO, SUMATRA, INDONESIA, DOCUMENTED BY STRUCTURE -FROM-MOTION PHOTOGRAMMETRY 108

5.1 Sinabung Volcano and Large Viscous Lava Flows 109

5.2 Measuring Active Domes and Flows 110

5.3 Methods..... 112

5.4 Results..... 115

5.5 Discussion 118

5.6 Conclusions..... 122

6 MECHANISMS OF LAVA FLOW EMPLACEMENT DURING THE EFFUSIVE ERUPTION OF SINABUNG VOLCANO (SUMATRA, INDONESIA) 130

6.1 Introduction..... 131

6.1.1 Current Eruption of Sinabung..... 132

6.1.2 Emplacement of Viscous Lava Flows 133

6.2 Methods..... 135

6.2.1 Satellite Images 135

6.2.2 Flow Models 138

6.3 Results..... 140

6.3.1 Flow Growth 140

6.3.2 Eruption Phases..... 142

6.3.3 Flow Advance Modeling 144

6.4 Discussion 145

CHAPTER Page

6.5 Conclusions 150

7 CONCLUSIONS 160

7.1 A Tale of Two Eruptions: Summary of Study Sites and Techniques .. 160

7.2 Pyroclastic Density Currents (PDCs) 162

7.3 Small-Scale Processes 163

7.4 Volcano-Tectonic Interactions 164

7.5 Future Directions 165

REFERENCES 167

APPENDIX

A DETAILED DESCRIPTION OF STRUCTURE-FROM-MOTION PROCESSING TECHNIQUES 178

A.1 Structure-from-Motion Point Clouds and Georeferencing (Agisoft Photoscan™ 1.0.4) 179

A.2 Point Cloud Alignment and Cloud To Cloud Distances (Cloud Compare) 180

A.3 Digital Surface Model Construction and Analysis (ArcGIS™ 10.2) .. 182

A.4 Volume Computation (Matlab™ 2014b) 183

A.5 Error Determination 183

LIST OF TABLES

Table		Page
2.1	Extrusion Rate and Volume for the 2006 Eruption of Merapi	49
3.1	List of Input Parameters for Merapi	74
3.2	Input Parameters for Each Phase of the 2006 Eruption	75
4.1	Input Parameters for Standard Run and Merapi 2010	107
5.1	Summary of Data for the Four Photogrammetric Models of Sinabung	129
6.1	Phases of the Sinabung Eruption	159
A.1	Photogrammetric Model Data From Agisoft Photoscan Pro™	189
A.2	Cloud Compare Alignments	190
A.3	Vertical Difference Errors Along Sinabung Profiles	191
A.4	Volume Calculation and Error	192

LIST OF FIGURES

Figure		Page
1.1	Silicic Volcanic Activity	9
1.2	Location of Volcanoes Active in the Past 10,000 Years	10
1.3	Effusive Silicic Volcanism	11
1.4	Transitions in Eruption Style	12
1.5	Location of Merapi and Sinabung Volcanoes	13
2.1	Location of Merapi Volcano	39
2.2	Volcanic Activity Style from MODIS Thermal Anomalies	40
2.3	Merapi ASTER Images	42
2.4	MODIS Extrusion Rate and Volume for Merapi	43
2.5	MODIS-derived Activity Style for Merapi	44
2.6	Activity Style for Eruption Phase 5	46
2.7	Observing Changes in Eruption Style with MODIS	47
2.8	PDC Correlation to Eruption Rate	48
3.1	Location of Merapi Volcano	69
3.2	Schematic of the Conduit Model	70
3.3	Model Results for Phase 1-2 Ascent Conditions	71
3.4	Extrusion Rate During the 2006 Eruption	73
4.1	Location of Merapi Volcano	97
4.2	Model Results for Magma Ascent	98
4.3	Variable Effects on Mass Flow Rate	101
4.4	Effects of Multiple Parameters on Mass Flow Rate	102

Figure Page

4.5 Effects of Multiple Parameters on Fragmentation 104

5.1 Location of Sinabung Volcno 123

5.2 Model 4 Dense Point Cloud Point Density 124

5.3 Histograms of Vertical Difference Errors 125

5.4 Photogrammetric Model of Sinabung 126

5.5 Thickness Map and Profiles of the Sinabung Lava Flow 127

5.6 Change Detection at Sinabung by SfM 128

6.1 Location Map of Sinabung Volcano 152

6.2 Flow Advance of the 2014 Sinabung Lava Flow..... 153

6.3 Estimated Thickness of Lava Flow Crust 154

6.4 Radiance of the Sinabung Lava Flow from MODIS Imagery..... 155

6.5 Eruption Rates of the Sinabung Lava Flow 156

6.6 Modeling of the Sinabung Lava Flow Advance 157

6.7 Conceptual Model of the Emplacement of the Sinabung Lava Flow..... 158

A.1 Location of Control Points 186

A.2 Location of Flow and Non-Flow Regions 187

A.3 Average Vertical Difference for Sinabung Profiles..... 188

CHAPTER 1

INTRODUCTION

Volcanic eruptions are violent showcases of the forces driving our dynamic planet. Eruptions can vary from small lava flows to global events capable of changing climate and destroying civilizations. The power of volcanoes has made them part of mythology and legend in cultures around the world, and today hundreds of millions of people still live in harm's way of an eruption (Oppenheimer, 2011). Despite the dangers and natural curiosity that result from volcanic eruptions, much remains to be learned about the processes driving eruptions and the diverse eruption styles that can result when magma reaches the earth's surface. In this dissertation I use a combination of observations and analysis techniques to explain the eruptive behavior at volcanoes erupting more viscous, silicic lava. The work presented here makes contributions to improve the monitoring and understanding of silicic volcanism with the broad goal of helping to reduce the risks from the many hazards related to these eruptions.

For the work presented in this dissertation, I define the term silicic volcanism to refer to eruptions of lava with a silica (SiO_2) weight faction greater than ~55%. This lava is distinguishable from basaltic lavas by its higher viscosity, which results in different types of volcanic features and styles of effusive and explosive activity (Figure 1.1a). Magma with silicic composition is most commonly generated due to subduction processes (Rogers, 2015), and volcanoes erupting silicic lava are found along subduction zones around the world (Figure 1.2). Many of these volcanoes are currently, recently, or potentially active (Siebert et al., 2010), and the risk of their eruptions is compounded by

the fact that the location of these volcanoes often overlaps with some of the most densely populated regions on earth (Figure 1.1b).

Silicic lava can erupt either effusively or explosively. In general, effusive eruptions result when magma ascent rates are slow enough to allow the magma to degas significantly prior to reaching the vent, whereas when gas cannot escape it causes the magma to fragment, resulting in rapid decompression of the gas and an explosive eruptions (Woods & Koyaguchi, 1994; Kozono and Koyaguchi, 2012). Explosive eruptions are characterized by large ash plumes tens of kilometers tall as a result of mass flow rates that can be in excess of 10^8 kg s^{-1} (Sparks, 1986). These eruptions, such as that of Pinatubo Volcano in the Phillipines in 1991 (Hammer et al., 1999), cause widespread ash fall (Sparks, 1986), disruptions to air traffic (e.g. Prata, 2009; Bull & Buurman, 2013; Kristiansen et al., 2015), and large pyroclastic density currents (PDCs) generated by the collapsing eruption column (Cole et al., 2015). These eruptions are generally short-lived, lasting a few hours to days, and eruption sequences are separated by years, decades, or even millennia of quiescence (Siebert et al., 2013).

Effusive eruptions at silicic volcanoes are characterized by extrusion of lava at the vent at volume flow rates from < 1.0 m^3 s^{-1} (Harris et al., 2002) to > 60.0m^3 s^{-1} (Pallister et al., 2013b). The erupted lava can pile up around the vent, forming a lava dome (Figure 1.3a) as at Mount St. Helens in Washington in 1980-1986 (Fink et al., 1990), or slowly move away from the vent to form a thick, blocky lava flow (Figure 1.3b), as at Cordón Caulle Volcano in Chile in 2011-2012 (Tuffen et al., 2013). Effusive eruptions can last from a few weeks to over 100 years (Wolpert et al., 2016), presenting a continuous hazard to the surrounding region. The primary hazard from effusive eruptions is the

collapse of the erupted lava due to either gravitational instabilities (Voight et al., 2000) or explosions caused by gas build-up within the lava (Clarke et al., 2007). The collapses form block-and-ash style pyroclastic flows and accompanying pyroclastic surges, which can have temperatures as high as 400 °C, speeds of 50 – 100 m s^{-1}, and runout distances of many kilometers (Cole et al., 2015). These PDCs can also produce plumes capable of spreading ash over a large area (Brown & Andrews, 2015). The effusion rate is the main controlling factor for a variety of effusive processes. Higher effusion rates have been correlated to increased size and frequency of PDCs (Nakada et al., 1999; Calder et al., 2002) and a preference for forming lava flows instead of lava domes and higher rates of flow advance (Lyman et al., 2004).

A single volcano is not limited to one type of activity or the other. Silicic volcanoes frequently switch styles between eruption events (Figure 1.4), as at Santa Maria Volcano in Guatemala (Harris et al., 2003), Mount St. Helens (Fink et al., 1990), and Kelud Volcano in Indonesia (Kristiansen et al., 2015), among many others. Effusive dome growth also commonly follows explosive activity (Ogburn et al., 2015), as at Chaitén Volcano in Chile in 2008-2009 (Pallister et al., 2013b). Explosive and effusive activity can also occur as different phases within a single eruption sequence, as was observed at Merapi Volcano in Indonesia in 2010 (Pallister et al., 2013a).

Studying active eruptions can be difficult due to the danger of closely approaching a volcanic vent and the unpredictability of eruptions, which both limit the types of observations that can be made. Many frequently active volcanoes have permanent monitoring networks and staffed observatories collecting a variety of data such as seismicity, infrasound, visual and thermal imagery, gas measurements, and

deformation from global positioning systems or tiltmeters. These observations, while extensive, are limited to a single volcano and the study of the activity it presents, which may not always be representative of other systems. Monitoring instruments and techniques can also be mobilized and deployed temporarily at multiple volcanoes, though these methods are then limited by the timing of the instrument deployment and the eruptive activity.

Advances over the past decades in the quality and quantity of satellite remote sensing data now available allows all active volcanoes all over the world to be observed on a daily basis. Various satellite instruments use a wide range of wavelengths to observe ash and gas emissions (e.g. Carn et al., 2008; Prata, 2009), thermal anomalies (e.g. Oppenheimer, 1991; Harris et al, 1997), deformation (e.g. Massonnet & Feigl, 1998; Chaussard et al., 2013; Pritchard et al., 2014), topographic changes (e.g. Poland, 2014; Albino et al., 2015), and pyroclastic deposits (e.g. Charbonnier et al., 2013). Constant observations from these instruments now offer a staggering quantity of current and historical data that can be used to observe and study volcanic activity.

Complications with satellite observations relate to the weather and instrument resolution. The signal from the volcano can be blocked by cloud cover or interfered with by a variety of atmospheric conditions. Instruments that capture data of a location with daily frequency generally have a low resolution of 1 km or greater per pixel (Delgado et al., 2014), which is often too large to capture details at a volcano, especially during a smaller eruption or the interval between eruptions. Instruments with higher resolution of ~100 m or less can observe these details, but have repeat intervals of 1-2 weeks or more (Delgado et al., 2014). The best applications of remote sensing data use multiple

instruments with different resolutions to observe multiple type volcanic activity (e.g. Delgado et al., 2014; Pritchard et al. 2014, Jay et al., 2015).

The development of numerical models for different types of volcanic activity is a vital tool for understanding volcanic activity. Models have been developed for almost every aspect of volcanic eruptions, such as deformation (e.g. Ali & Feigl, 2012), magma flow in a conduit (e.g. Melnik & Sparks, 1999; de' Michieli Vitturi, 2008; Degruyter et al., 2012), PDCs (e.g. Charbonnier & Gertisser, 2012), eruption plumes (e.g. Mastin, 2009), and lava flows (e.g. Harris & Rowland, 2001), among many others. Model applications can include but are not limited to parameter estimation for observed eruptions, variable sensitivity analysis, and forward applications to anticipate possible future activity. Models also provide insight into processes that cannot be observed, such as those in magma storage systems or a volcanic conduit.

My work in this dissertation is motivated by the diversity of silicic volcanic activity and the techniques available to observe, document, and model these eruptions. I combine proven methods with techniques I develop to observe eruptions both remotely and in the field and use numerical models to describe the processes responsible for the activity I document. The chapters that follow address a number of key questions in volcanology, such as:

- How and why do effusive eruptions change and evolve?
- How do lava domes and flows grow and generate PDCs?
- How do volcanoes transition between effusive and explosive styles?
- How can monitoring and observation of these eruptions be improved to aid eruption forecasting and prediction?

My conclusions add new insight to the eruptions at Merapi Volcano in 2006 and 2010 as well as for the first time present a description of the ongoing eruption at Sinabung Volcano in Indonesia (Figure 1.5).

Chapter 2 addresses the variable extrusion rate and PDC activity during the 2006 effusive eruption of Merapi using nighttime satellite thermal images from the Moderate Resolution Imaging Specroradiometer (MODIS). I use established methods to estimate extrusion rate and total volume of magma extruded (e.g. Harris & Ripepe, 2007). I also develop a new method using the size and average radiance of a thermal anomaly to distinguish between dominant activity styles in a satellite thermal image, such as dome growth or PDCs. The nightly frequency of MODIS images allows for frequent observations and the creation of dense time-series of extrusion rate, extruded volume, and eruptive activity that track the varying intensity of the eruption. I show that a large amount of information can be derived from MODIS images despite the 1 km pixel size in the thermal bands.

In **Chapter 3** I apply a numerical model for magma ascent in a volcanic conduit to offer insight on conduit processes related to the variable extrusion rates during the 2006 eruption of Merapi that I document in **Chapter 2**. I first validate the model by using literature values for the Merapi system as input to the model to produce extrusion rates that agree with published values (Ratdomopurbo et al., 2013) and those I estimate in **Chapter 2**. Previous works suggest that the peak extrusion rates of this eruption were triggered by a nearby tectonic earthquake that induced either increased pressure in the system (Walter et al., 2007; Harris & Ripepe, 2007) or release of volatiles into the system (Troll et al., 2012). I test these theories by varying the input values for magma chamber

overpressure and initial volatile mass fraction to show the magnitude of a change in either parameter necessary to result in the observed increase in extrusion rate and thus comment on how the earthquake may have been able to affect the Merapi system. The waning phase of the eruption was characterized by large but infrequent PDC activity (Ratdomopurbo et al., 2013), so I also vary the dome height in the model to demonstrate how dome collapses may affect extrusion rates and eruption duration.

Chapter 4 applies the same conduit ascent model to first address the general case of effusive-explosive transitions in silicic systems and then applies the model to the 2010 eruption of Merapi. I identify a number of key parameters (e.g. volatile weight %, crystal volume fraction, dome height, conduit radius, magma temperature, and chamber overpressure) and isolate them over a series of iterative model runs to show the effect of a single variable on mass flow rate and whether or not magma fragmentation occurs. I also test sets of multiple free variables to investigate the potential compounding effects of multiple parameters varying within a dynamic system. The 2010 eruption of Merapi was much larger than the 2006 eruption and included both explosive and effusive phases. I use the model to offer insight for both the transition from effusive eruption in 2006 to explosive in 2010 and the effusive-explosion transitions that occurred during the 2010 sequence.

Chapter 5 discusses the emplacement of a 3 km long lava flow during the effusive eruption of Sinabung Volcano from 2013 to present. During a field campaign in 2014 I applied the structure-from-motion (SfM) photogrammetry technique to generate multiple 3D and digital elevation models (DEMs) of the lava flow. SfM is a relatively new technique in volcanology and I show that it can be used cheaply and quickly with

standard consumer digital cameras to generate topographic data that previously required specialized equipment and high costs to acquire. I use the DEMs I create to estimate the volume of the lava flow and detect changes in the flow that occurred in the few days between photograph acquisitions. The location and magnitude of the changes I observe are related to flow emplacement and I use this information to describe the processes shaping the flow during and following my field campaign.

In **Chapter 6** I describe the eruption of Sinabung in its entirety using data from multiple remote sensing techniques (e.g. Oppenheimer, 1991; Harris & Ripepe, 2007) and a model of lava flow emplacement (Castruccio et al., 2013). I use visual and thermal satellite images to calculate flow advance rate, estimate a thickness for the flow crust, and estimate effusion rates. The rate of flow advance and the frequency of PDCs generated by collapse of part of the flow vary significantly during the eruption, and I offer explanations for the processes controlling activity in each phase. I show that the emplacement of the lava flow and associated PDCs are related to a variable effusion rate, the mechanism controlling the rate of flow advance, and the underlying topography.

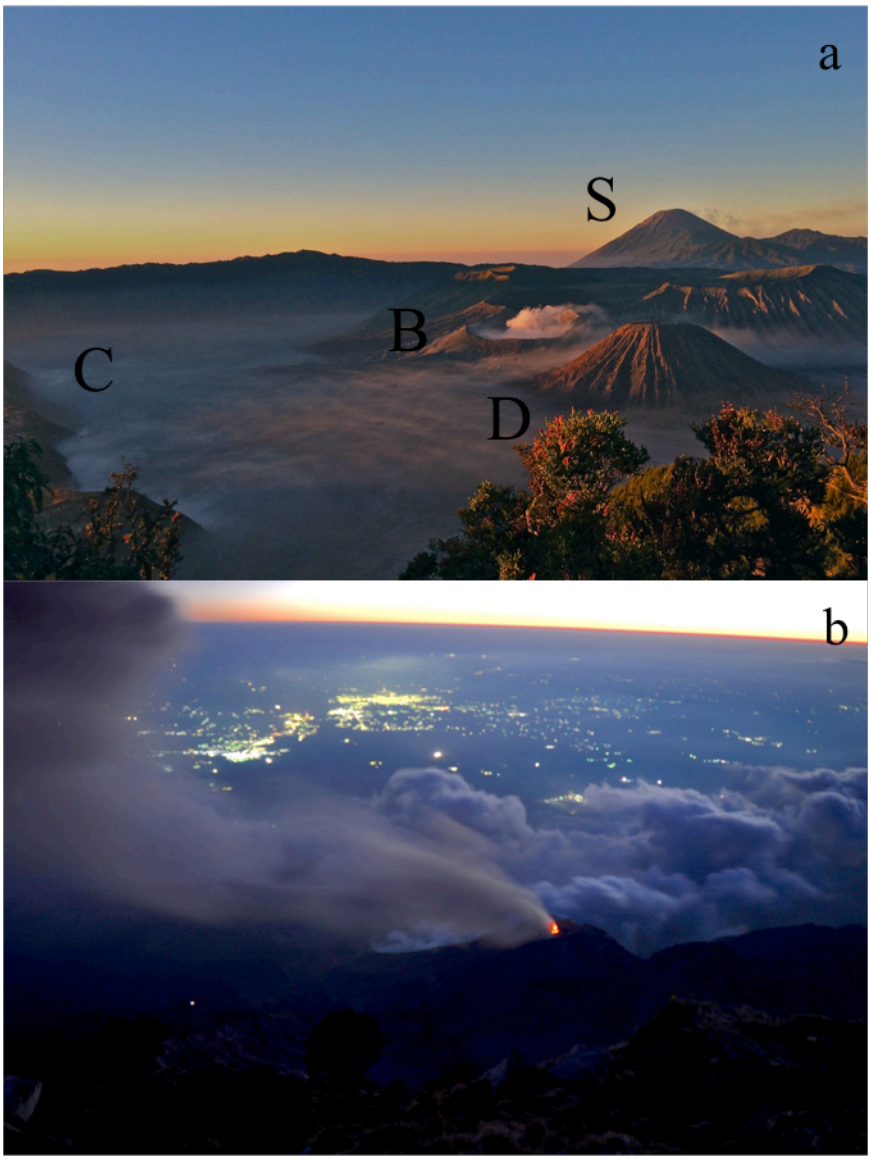

Figure 1.1. Silicic volcanic activity. The Tengger Caldera in East Java, Indonesia (a) shows a variety of silicic volcanic landforms including a lava dome (D), actively degassing Bromo crater (B), the caldera (C), and the active Semeru Volcano (S). A nighttime eruption of Santiaguito Volcano in Guatemala (b) shows incandescent lava at the vent in the foreground while city lights are seen not too far away in the background.

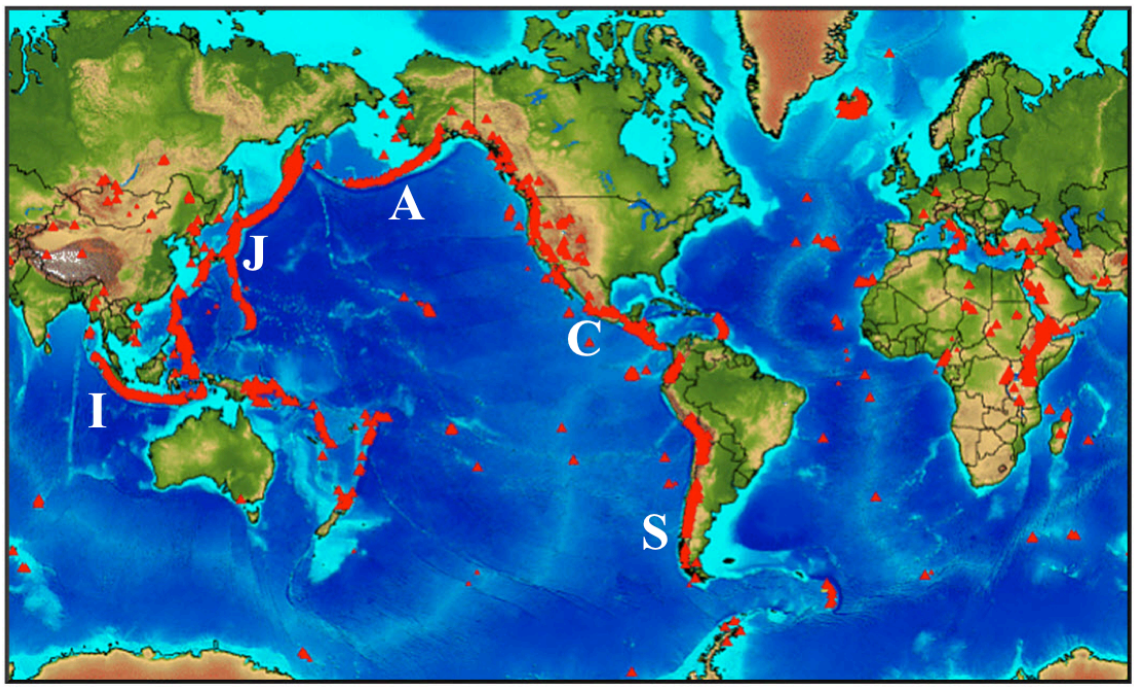

Figure 1.2. Location of volcanoes active in the past 10,000 years. Most silicic volcanoes are located along subduction zone volcanic arcs such as Indonesia (I), Alaska (A), Central (C) and South (S) America, and Japan (J). Map is from the Smithsonian Global Volcanism Program at: http://www.volcano.si.edu/.

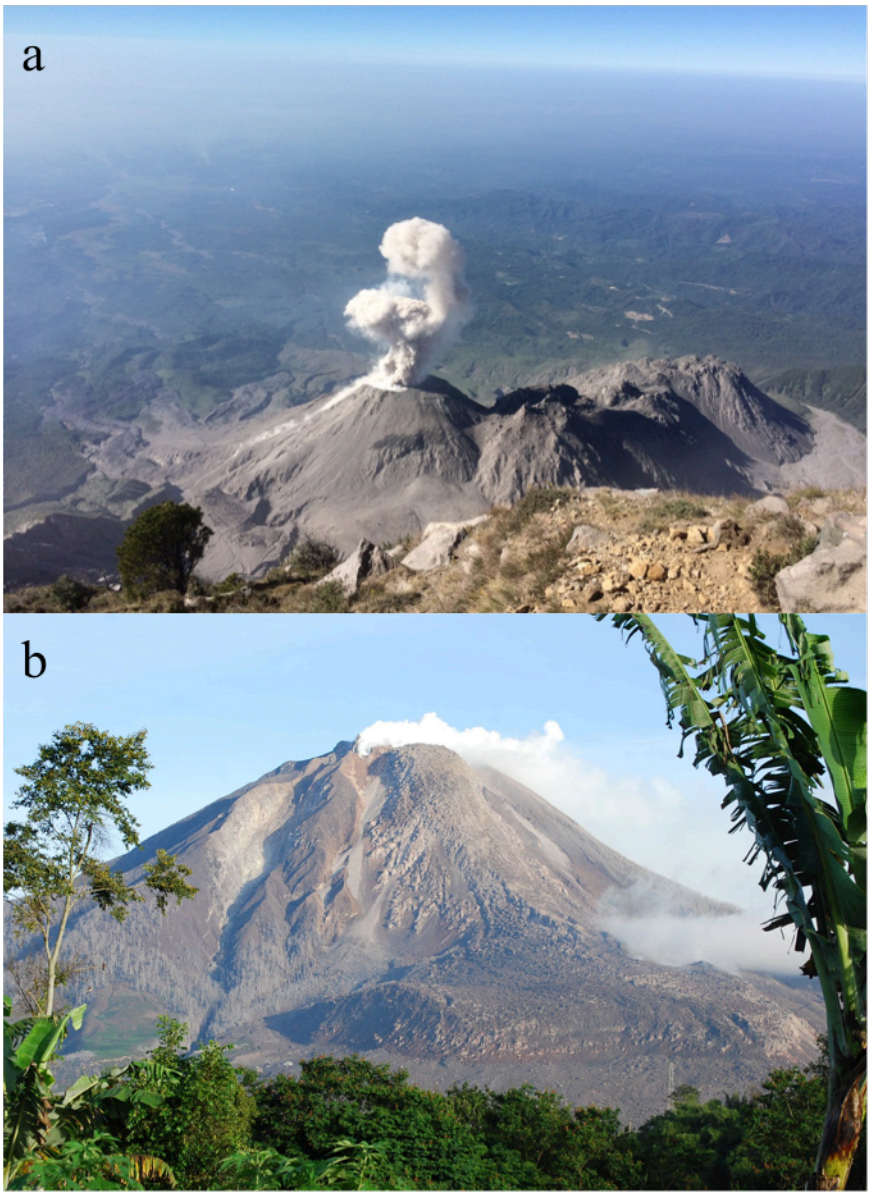

Figure 1.3. Effusive silicic volcanism. Effusion eruptions at silicic volcanoes can produce lava domes as at Santiaguito Volcano (a) and lava flows as at Sinabung Volcano (b).

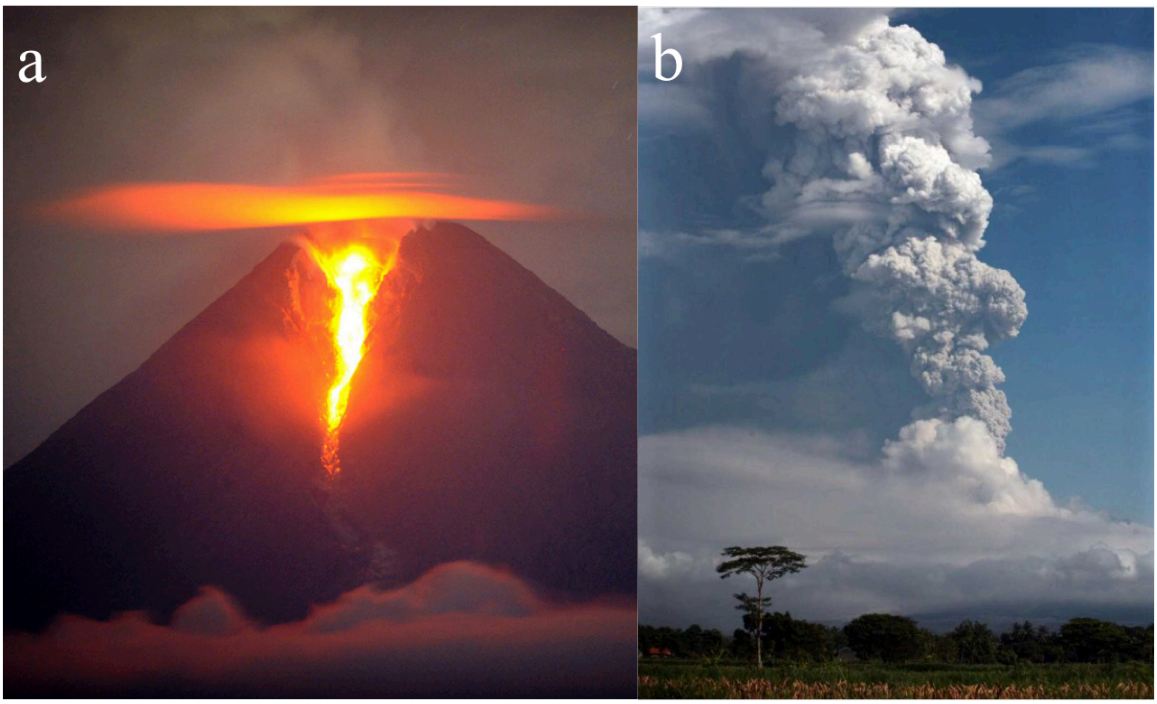

Figure 1.4. Transitions in eruption style. Transitions between effusive (a) and explosive (b) activity can occur at a volcano during a single eruption sequence, as at Merapi Volcano in 2010. Image (a) from http://blogs.sacbee.com/photos/2010/11/mount-merapis-worst-eruption-i.html, image (b) from http://news.monstersandcritics.com/asiapacific/features/article_1596607.php/Mount-Merapi-Eruption-Pictures-November-4th.

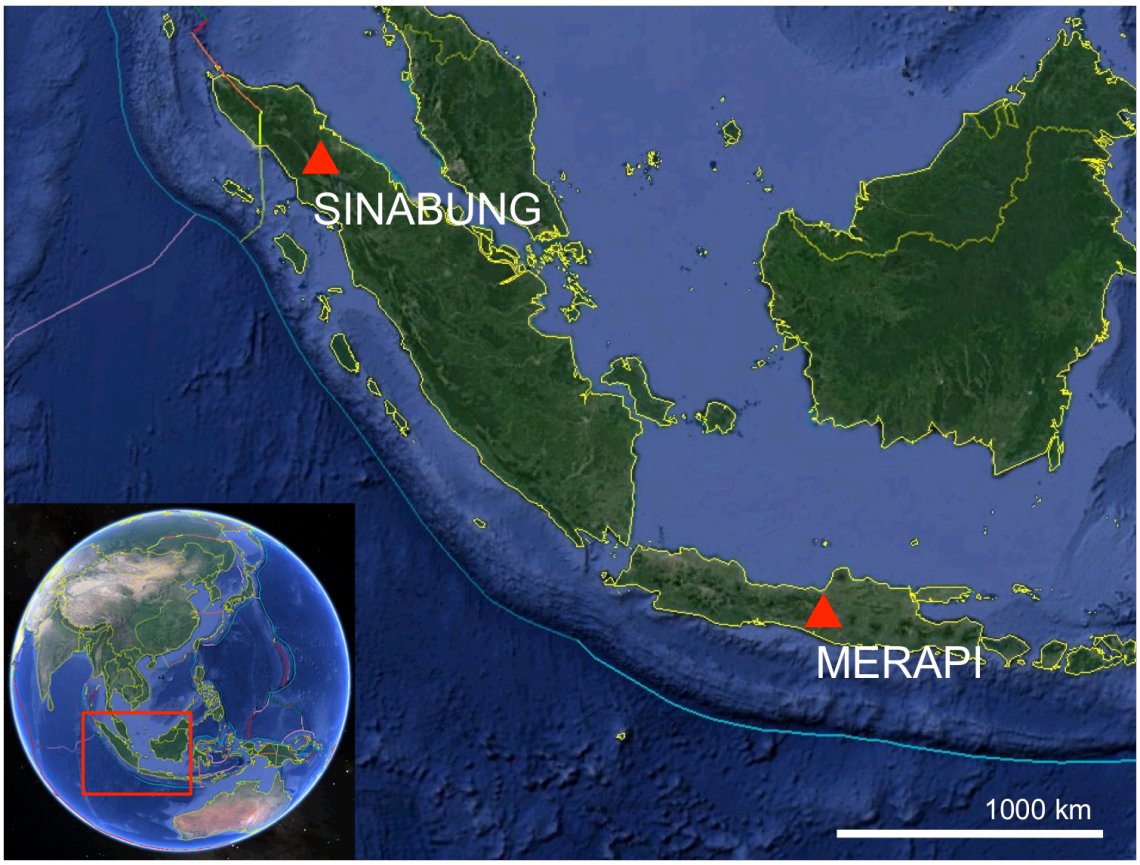

Figure 1.5. Location of Merapi and Sinabung Volcanoes. Sinabung Volcano is located in North Sumatra, Indonesia. Merapi is located in Central Java, Indonesia. Images are © Google Earth™; plate boundaries are from Bird (2003). INSET: Location of main map within Asia.

CHAPTER 2

THE 2006 LAVA DOME ERUPTION OF MERAPI VOLCANO (INDONESIA): DETAILED ANALYSIS USING MODIS TIR

The results from this chapter have been published in a peer-reviewed journal and can be found under the reference below. My co-authors have given me permission to reproduce the work here in my dissertation.

Carr, B. B., A. B. Clarke, L. Vanderkluysen, 2016, The 2006 lava dome eruption of Merapi Volcano (Indonesia): detailed analysis using MODIS TIR. *Journal of Volcanology and Geothermal Research*, 311, 60-71, http://dx.doi.org/10.1016/j.jvolgeores.2015.12.004.

Merapi is one of Indonesia's most active and dangerous volcanoes. Prior to the 2010 VEI 4 eruption, activity at Merapi during the 20th century was characterized by the growth and collapse of a series of lava domes. Periods of very slow growth were punctuated by short episodes of increased eruption rates characterized by dome collapse-generated pyroclastic density currents (PDCs). An eruptive event of this type occurred in May-June, 2006. For effusive eruptions such as this, detailed extrusion rate records are important for understanding the processes driving the eruption and the hazards presented by the eruption. I use thermal infrared (TIR) images from the Moderate Resolution Imaging Spectrometer (MODIS) instrument on NASA's Aqua and Terra satellites to estimate extrusion rates at Merapi Volcano during the 2006 eruption using the method of

Harris & Ripepe (2007). I compile a set of 75 nighttime MODIS images of the eruptive period to produce a detailed time series of thermal radiance and extrusion rate that reveal multiple phases of the 2006 eruption. These data closely correspond to the published ground-based observational record and improve observation density and detail during the eruption sequence. Furthermore, additional analysis of radiance values for thermal anomalies in Band 21 (λ = 3.959 mm) of MODIS images results in a new framework for detecting different styles of activity. I successfully discriminate among slow dome growth, rapid dome growth, and PDC-producing dome collapse. I also demonstrate a positive correlation between PDC frequency and extrusion rate, and provide evidence that extrusion rate can increase in response to external events such as dome collapses or tectonic earthquakes. This study represents a new method of documenting volcanic activity that can be applied to other similar volcanic systems.

2.1. Introduction

Mount Merapi, located in central Java, Indonesia (Figure 2.1), is one of Indonesia's most active and dangerous volcanoes. During the 20th century frequent lava dome growth at the summit presented a near-constant threat of pyroclastic density currents (PDCs) to the densely populated area around the mountain. Large-scale evacuations and fatalities associated with these PDCs were common (Voight et al., 2000). This style of activity, an active lava dome producing frequent PDCs, is commonly known as a "Merapi-type" eruption (Voight et al., 2000).

Documenting the extrusion rate of an active lava dome is critical to understanding the hazards presented by Merapi-type eruptions. Increases in extrusion rate have been

linked to the risk of dome collapses and PDCs (Nakada et al., 1999; Calder et al., 2002) and is an observable quantity that provides insight into deep and shallow subsurface processes (Melnik & Sparks, 1999; 2002; de' Michieli Vitturi et al., 2008; 2010; 2013). Unfortunately, frequent and accurate extrusion rate measurements can be difficult to obtain, especially at remote volcanoes or observatories with limited resources. However, extrusion rate can be derived from satellite thermal infrared (TIR) images that are acquired daily (Harris et al., 1997). High-resolution satellite TIR images can also be used to extract details about volcanic activity, such as locating regions of active dome growth or identifying the collapsing front of a lava lobe (e.g., Oppenheimer et al., 1993; Wooster et al., 2000). Here I combine previously published ground-based observations from the Merapi eruption in 2006 with numerous satellite TIR images from the same time interval and document the different phases of dome growth and collapse in detail by extracting a daily time series of extrusion rate and distinguishing pure dome growth from PDC-producing collapses. In doing so, I also develop a new framework for distinguishing different styles of activity from satellite observations. These data and the techniques developed in this manuscript provide insight into lava dome hazards and the processes controlling them at Merapi and similar volcanoes around the world.

2.1.1. Recent Merapi activity

For much of the 20th century, a series of basaltic-andesite (Hammer et al., 2000) lava domes were active at the summit of Merapi. Long periods of low-level activity were punctuated by eruptive sequences consisting of elevated extrusion rates and multiple gravitational collapse-generated PDCs. Merapi's 20th century eruptions also occasionally

included small explosions, but were rarely classified as larger than VEI 2 (Volcano Explosivity Index; Newhall & Self, 1982). Larger VEI 3 events occurred in 1930-1931 and 1961. Prior to 2010, the most recent periods of elevated extrusion rates and frequent PDCs occurred in 1992, 1994, 1997-1998, 2001, and 2006 (Voight et al., 2000; Ratdomopurbo et al., 2013). The 20th century-averaged eruption rate at Merapi was 0.03 m^3 s^{-1}, while elevated activity associated with Merapi-type events occurred every few years with average eruption rates of 1-4 m^3 s^{-1} (Siswowidjoyo et al., 1995).

The 2006 eruption started with extrusion of lava on or around April 26 (Ratdomopurbo et al., 2013) and began building a new dome (beginning of Phase 1, Table 2.1). The first PDCs occurred on May 11 (beginning of Phase 2, Table 2.1). On May 27 (beginning of Phase 3), a M_w 6.4 earthquake occurred about 50 km SSE of Merapi (Walter et al., 2007), which was followed by an increase in extrusion rate and the frequency of PDCs (Harris & Ripepe, 2007; Walter et al., 2007; Ratdomopurbo et al., 2013). The elevated level of activity continued through June 8 (end of Phase 3, Table 2.1) (Ratdomopurbo et al., 2013), after which the intensity of the eruption decreased (Phase 4, Table 2.1). During Phase 3, the new lava dome was growing over and applying pressure to the southern wall of the summit crater, causing a transition from PDCs dominantly traveling southwest down the Boyong-Krasak drainages to dominantly traveling south down the Gendol drainage (Figure 2.1) (Charbonnier & Gertisser, 2008; Ratdomopurbo et al., 2013). During Phase 4, the crater wall began to collapse until its complete removal on June 14 (beginning of Phase 5, Table 2.1), which led to the largest dome collapse and PDCs of the 2006 eruption. These flows extended up to 7 km from the vent and caused the only two fatalities of the eruption (Charbonnier & Gertisser, 2008). The alert level, as

determined by the Indonesian Center of Volcanology and Geological Hazards Mitigation (CVGHM), was lowered from 4 to 3 (on a 1-4 scale) on July 10th (end of phase 5, Table 2.1) (Global Volcanism Program, 2007). Dome growth and PDCs continued at a decreasing rate until October, when activity returned to background levels (Ratdomopurbo et al., 2013).

In 2010, Merapi's eruption style changed dramatically with a VEI 4 event that produced sustained eruption columns, column collapse-induced PDCs extending 16 km from the vent, and extremely rapid dome extrusion in excess of 25 m^3 s^{-1} (Surono et al., 2012; Komorowski et al., 2013; Charbonnier et al., 2013). The unexpected increase in eruption intensity and the size of the PDCs led to the deaths of over 350 people (Surono et al., 2012). The previous VEI 4 eruption at Merapi occurred in 1872, and eruptions of this size were more common in the two millennia prior that year compared to the past 150 years (Voight et al., 2000; Newhall et al., 2000; Gertisser et al., 2012).

2.1.2. Satellite thermal remote sensing

The quality and quantity of satellite thermal data available for observing volcanic activity have rapidly increased in recent decades (Ramsey & Harris, 2013). Satellite data can supplement ground observations and allow frequent observation of remote and infrequently observed volcanoes (e.g. Harris et al., 2003; Rose & Ramsey, 2009). Combining satellite and ground-based data from well-documented eruptions such as those of Merapi make excellent case studies for constraining the accuracy of current remote sensing methods and for developing new techniques. Increasing the accuracy and expanding the utility of satellite thermal data has the potential to improve understanding

and mitigation of hazards at both well-observed and remote volcanoes (Ramsey & Harris, 2013). Satellite thermal images are available in multiple resolutions and have many different applications. Low spatial resolution images (≥1 km pixel size) with high temporal resolution (daily repeat cycle), such as those from the Advanced Very High Resolution Radiometer (AVHRR) and the Moderate Resolution Imaging Spectroradiometer (MODIS), allow for the creation of dense times series of volcanic activity (e.g., Coppola et al., 2012), while high spatial resolution thermal images (≤100 m pixel size), such as those from the Advanced Spaceborne Thermal Emission Reflection Radiometer (ASTER), allow for the detection of less intense thermal signals and more detailed documentation of thermal features (e.g., Oppenheimer et al., 1993; Wooster et al., 2000).

Pieri & Baloga (1986) developed a technique for extracting extrusion rate from observed thermal radiance. The method assumes a steady-state lava flow where the temperature of the lava at any location is constant in time and that the surface area of the lava flow is cooling-limited. The method was modified by Harris et al. (1997; 2003) and Harris & Ripepe (2007) to include convective and conductive heat loss in addition to radiative heat loss, the latent heat of crystallization of the lava, and the identification and contribution of sub-pixel volcanic thermal sources. The assumptions necessary to estimate extrusion rate from thermal radiance have been validated previously by comparison between values derived from satellite images and those based on field measurements of lava flows with compositions varying from basalt to andesite (Harris et al., 1997; Harris & Baloga, 2009). This study further validates the approach.

2.2. Methods

2.2.1. Acquisition of MODIS TIR images

The MODIS instruments capture four images of every location on earth every day, one daytime and one nighttime image from both the Aqua and Terra satellites (National Aeronautics and Space Administration's (NASA) Earth Observing System program). Each image has a 1 km pixel size in the thermal bands (bands 20-36, $\lambda = 3.660 - 14.385$ μm) and is available online (ladsweb.nascom.nasa.gov). I selected my data from the set of Level 1B nighttime Aqua and Terra MODIS TIR images taken of the island of Java during 2006. Level 1B data are calibrated and geolocated and give at-sensor radiance values in W/(m^2 mm sr). I did not use daytime images in this study to avoid solar thermal interference. The scenes were manually inspected for minimal cloud cover before download. I downloaded qualifying images for all of 2006, including 75 scenes spanning the 2006 Merapi eruption (April 26 – July 10). The images were georeferenced using the MODIS Conversion Toolkit, a free plug-in available for the ENVI™ software (Exelis Visual Information Services). I also used this toolkit to correct for the bow-tie affect that can result in overestimation of thermal anomalies at extreme viewing angles (Coppola et al., 2012).

Georeferenced and corrected MODIS TIR scenes contain atmospheric interference, primarily from the very humid tropical climate in Indonesia that can cause signal noise of similar magnitude to a volcanic thermal anomaly. This interference must be removed in order to observe the desired detail of the thermal anomalies in each image. Some previous studies (e.g., Wooster & Kaneko, 1998; Harris & Ripepe, 2007) utilized an atmospheric model, such as MODTRAN, to calculate an atmospheric transmittance

value for each image. This method is impractical for this study, however, as it requires accurate meteorological data from near the study region, which is difficult to obtain or non-existent for many volcanoes of interest. Instead, this work follows previous studies that have used a background region subtraction to account for atmospheric effects (e.g., Wright et al., 2002; Coppola et al., 2012). Many active volcanoes have inactive neighbors of similar morphology, providing convenient and comparable regions to use as background for the active volcano. For Merapi, I use neighboring Merbabu volcano and limit all of my calculations to regions of interest (ROIs) over each volcano (Figure 2.1). Results are not particularly sensitive to which method is used; using a background subtraction in this study I was able to reproduce the results of Harris & Ripepe (2007) who used an atmospheric model. The method used to account for atmospheric affects should be determined by the availability of a good background region compared to access to the MODTRAN model and quality weather data.

2.2.2. Extrusion rate estimate from thermal radiance

From Pieri & Baloga (1986), the equation for one-dimensional heat transport in a lava flow is

$$\rho C_p \left[\frac{\partial}{\partial t} + u \frac{\partial}{\partial x} \right] T_x h_x w_x = -L_{rad} \tag{2.1}$$

where ρ is lava density, C_p is the specific heat capacity, t is time (in seconds), T is the lava temperature (in Kelvin), u is propagation velocity, L_{rad} is the radiative thermal loss function, and x, h, and w are the length along the flow, height of the flow, and width of the flow, respectively. For L_{rad}, I use the thermally unmixed case from Pieri & Baloga

(1986) for a lava flow with a solid surface radiating at a temperature less than or equal to the solidification temperature of the lava, a good assumption for a lava dome. In this case,

$$-L_{rad} = \varepsilon\sigma T_h^4 w_x \tag{2.2}$$

where ε is the emissivity of the lava surface (for andesite $\varepsilon = 0.98$; Harris & Ripepe, 2007), $\sigma = 5.67 \times 10^{-8}$ W m^{-2} K^{-4} is the Stefan-Boltzmann constant, and T_h is the average radiating temperature of the lava surface. Assuming a steady-state and cooling-limited flow (Harris & Baloga, 2009), eq. 2.1 can be solved for the volume flow rate, $E = uh_x w_x$, by integrating over the length of the flow, or in the case of a lava dome, the radius of the dome. Because of the assumptions associated with this method, I cannot estimate an instantaneous extrusion rate at the time of image acquisition, but rather, I estimate the time-averaged discharge rate required to produce a flow or dome of the observed size for a lava with the given physical properties and temperature (Wright et al., 2001).

Harris et al. (1997) modified eq. 2.1 to include both the latent heat of crystallization ($L = 3.5 \times 10^5$ J/kg) within the lava flow and heat loss due to convection from the flow surface giving volume flow rate E

$$E = \frac{Q_{total}}{\rho\left(C_p \Delta T + L\varphi\right)} \tag{2.3}$$

where Q_{total} is the heat lost by the lava, ΔT is the post-eruptive cooling of the lava, and j is the post-eruptive crystallization. Q_{total} represents the sum of both the radiative heat flux from the lava surface (Q_{rad}) and the convective heat loss (Q_{conv}) from the lava flow surface to the atmosphere,

$$Q_{total} = Q_{rad} + Q_{conv} = A\sigma\varepsilon T_h^4 + Ah_c(T_h - T_{air}) \tag{2.4}$$

where $h_c \approx 50$ $Wm^{-2}K^{-1}$ is the convective heat transfer coefficient for an active lava flow (Harris & Ripepe, 2007; Harris et al., 2003), A is the flow area, and T_{air} is air temperature. As in Harris & Ripepe (2007), I assume surface processes dominate heat loss from the flow and that heat loss by conduction through the base of the dome is insignificant. I correct $\rho = 2600$ kg/m^3 (Dense Rock Equivalent (DRE) for andesite) and $C_p = 1150$ J kg^{-1} K^{-1} for 20% vesicularity and use $\varphi = 0.45$ and $T_{air} = 25$ °C following Harris & Ripepe (2007). Lava surface temperature (T_h) is variable depending on the relative fraction of the dome surface that is occupied by cracks exposing the hot interior of the dome (Harris & Ripepe, 2007) and therefore depends on the exogenous or endogenous style of dome growth or if a recent dome collapse has exposed the dome interior. This fraction is difficult to estimate and is not constant during an eruption, so a range of reasonable values for T_h must be utilized. I use lower and upper limits of T_h = 150 and $T_h = 270$ °C and $\Delta T = 200$ and $\Delta T = 350$ °C from Harris & Ripepe (2007) and Harris et al. (2003), who draw these values from the domes at Merapi and Santiaguito (Guatemala) respectively.

The flow area can be calculated using a two-component temperature model assuming the radiance of each pixel is the combination of two radiating surfaces: 1) the lava surface at $T = T_h$ and 2) the background at $T = T_b$. The pixel fraction occupied by lava in each pixel in an image (p) can be found by

$$L(T_i,\lambda) = pL(T_h,\lambda) + (1-p)(T_b,\lambda) \tag{2.5}$$

where $L(T,\lambda)$ is the Planck function for a blackbody radiating at temperature T and wavelength λ, and T_i is the Planck-derived pixel temperature. For eq. 2.5 I use MODIS Band 21 (central $\lambda = 3.959$ μm) because it is highly sensitive to sub-pixel temperature

anomalies (Harris & Ripepe, 2007). I obtain T_b from Band 32 (central λ = 12.02 μm), as it is less sensitive to sub-pixel anomalies and I can assume this temperature represents the majority non-lava ground cover. I calculate p for each pixel in the defined Merapi and Merbabu ROIs (Figure 2.1). Because a MODIS thermal pixel is 1 km^2, the area is

$$A = \sum_{i=1}^{\#\ pixels\_in\_ROI} 1km^2 \cdot p_i \tag{2.6}$$

Once the area is determined for each ROI, I subtract the background (Merbabu) area from the active (Merapi) area to produce the volcanic-derived thermal anomaly area for Merapi that I then use in eqs. 2.3 and 2.4 to give estimates of heat flux and extrusion rate from the volcano.

It is difficult to obtain well-known values for many of the constants in the equations above and best estimates are used in most cases. The radiating temperature of the lava surface (T_h) has the greatest effect on the resulting extrusion rate measurement over the range of possible values used in this study. Knowing the style of dome growth (endogenous vs. exogenous) exhibited by the dome can narrow the range of possible surface temperatures and improve the precision of extrusion rate estimates. The post-eruptive cooling (ΔT) value also has a large effect, and therefore the following results are presented with both maximum and minimum temperature combinations. Compared to the range of possible temperatures, other variables such as the amount of post-eruptive crystallization, lava density and vesicularity, and uncertainty in radiance values have a negligible effect on estimated extrusion rate.

2.2.3. Novel analysis of pixel radiances

In addition to calculating heat flux and extrusion rate, I developed a new method using the raw Band 21 radiance data to differentiate eruption activity styles. I am able to document characteristic thermal anomaly sizes and radiance intensities and correlate them with independently corroborated styles of eruption activity. In this section I introduce the basic concepts behind three new approaches of using the raw radiance data, and later assess the method within the context of outcomes from the 2006 Merapi data set.

In general, lava domes will have thermal anomalies of relatively small area (1 to 4 pixels) and high intensity compared to PDCs and their deposits, which will produce larger-area anomalies (typically >4 pixels) with lower intensity. Active lava domes and large PDCs are end member activity styles in the case of Merapi. Intermediate styles are common and can include coulees, rock avalanches, and small PDCs. Discriminating amongst these activity styles and the simultaneous occurrence of multiple styles of activity is difficult from satellite data but, as I demonstrate in this work, can be achieved by looking at the number of thermally anomalous pixels in each image ROI and the average radiance of those pixels. Through visual inspection of the images, I use an empirically determined lower bound of 0.5 W/(m^2 μm sr) in Band 21, equivalent to a pixel-integrated temperature of approximately 20 °C, to define thermally anomalous pixels. Figure 2.2a illustrates how different activity styles will appear in distinct regions when the average radiance of thermally anomalous pixels in an image is plotted against the number of anomalous pixels in the same image.

Activity style can also be differentiated by creating two ratios: 1) the average Band 21 radiance of pixels in the active ROI to the average Band 21 radiance of pixels in the background ROI (active:background) and 2) the maximum radiance of a pixel in the active ROI to the average radiance of pixels in the background (max:background) (as in Figure 2.2b). As the number of pixels affected by the thermal anomaly increases, the active:background ratio increases (horizontal axis Figure 2.2b), making it a proxy for the areal extent of the thermal anomaly, such that small values are associated with pure dome growth and large values are associated with extensive and still-hot PDC deposits. As a thermal anomaly increases in intensity, the max:background ratio increases (vertical axis Figure 2.2b), making it a proxy for temperature, such that large values tend to be associated with rapidly-growing lava domes and small values tend to be associated with cooler domes or cooling PDC deposits. The lines in Figure 2.2b are modeled end-member values showing where pure PDC and pure lava dome signals will fall. The dots in Figure 2.2b are modeled values for images with mixed thermal signals, those containing anomalous pixels representing both dome and PDC activity. This method (Figure 2.2b) is not as effective at distinguishing mixed signals associated with simultaneous activity styles as is the pixel count and mean method (Figure 2.2a) because the ratios are not independent of one another - increasing the maximum radiance in a single pixel also increases the average radiance. However, the advantage of this second regime diagram is that the ratios do not rely on a manually determined thermally anomalous radiance lower bound (as in Figure 2.2a). This advantage makes the radiance ratios useful for automated large batch analysis of multiple volcanoes or long-lived eruptions, both cases that, in

order to apply the pixel-mean method, would require multiple manual analyses to identify lower-bound radiances which tend to vary by location and season.

A third way to distinguish different types of activity using Band 21 radiance is by plotting the pixel radiances within the ROI of any single image as a histogram (insets, Figure 2.2a). The bin number of a pixel serves as a basic analog for activity, with pixels associated with cooler PDCs populating the left bins (1-2), warmer coulees or lava avalanches the middle bins (2-4), and hot active domes the right bins (4-5). The histogram peak indicates which is the dominant activity style, whereas pixels in other bins represent contributions to the thermal signal from other processes.

2.2.4. ASTER images

I also downloaded eight ASTER scenes captured during the 2006 Merapi eruption. The 90-meter resolution in the thermal bands (Bands 10-14, λ = 8.1-11.3 μm) is useful for observing more detail in a thermal anomaly, but the repeat interval of 1-2 weeks limits ASTER's utility for obtaining high frequency time series, which are required to observe rapid variations in extrusion rate and eruption style expected over the course of a 2-month burst of dome growth like the 2006 Merapi eruption. I apply similar methods to the ASTER images as those discussed above for MODIS data. Primarily, however, I use thermal images from ASTER Band 10 (λ = 8.291 μm) to make visual comparisons to my MODIS-derived interpretations (Figure 2.3).

2.3. Results

ASTER images acquired during the 2006 Merapi eruption (Figure 2.3) reveal the basic progression of the eruption. A small thermal signature is seen on the summit on April 28th (Figure 2.3a), revealing an active dome, consistent with the early stages of Phase 1 as documented by ground-based observations (Ratdomopurbo et al., 2013). A small PDC deposit is visible on May 14th in a drainage trending southwest from the crater (Figure 2.3b) and a larger deposit is present on May 30th, also to the southwest (Figure 2.3c), consistent with ground-based observations during Phases 2 and 3, respectively (Global Volcanism Program, 2007). By June 6th (end of Phase 3) PDCs were traveling south down the Gendol drainage (Figure 2.3d) as well as continuing toward the southwest, and by June 15th (beginning of Phase 5) most activity was focused to the south (Figure 2.3e), including the largest PDC of the eruption that occurred on June 14th (whose hot deposit can be seen in the June 15th ASTER image). Images on June 22nd (Figure 2.3f), July 1st (Figure 2.3g), and July 8th (Figure 2.3h) show continued PDC activity to the south but also a general decrease in the strength and size of the thermal anomalies, indicating cooling of the deposits and waning of the eruption.

The near-nightly frequency of clear MODIS TIR images allowed me to create a detailed time series of extrusion rate and total volume of extruded magma during the 2006 eruption (Figure 2.4). Variations in extrusion rate are captured by my TIR analysis, and several eruption stages can be distinguished (dashed vertical lines, Figure 2.4), such that the initiation, peak, waning, and renewal of activity during Phase 5 of the eruption are clearly visible. A sharp increase in extrusion rate is observed in mid-May, corresponding to the emplacement of the first PDCs (Phase 2, Figure 2.4; Table 2.1) that

followed the initial slow dome growth (Phase 1, Figure 2.4; Table 2.1). The eruption intensity continued to escalate to a peak in Phase 3 before it quickly decreased during Phase 4 (Figure 2.4; Table 2.1). Highly variable extrusion rates persisted through late June into July during phase 5 (Figure 2.4; Table 2.1).

Due to the previously discussed range in potential radiating and cooling temperatures of the lava, minimum and maximum possible heat fluxes exist for each image. The extrusion rate and total volume values reported hereafter in the text are calculated from the maximum possible heat flux, which results from assuming T_h = 150 °C and ΔT = 200 °C (Figure 2.4, solid lines). The minimum values, resulting from assuming T_h = 270 °C and ΔT = 350 °C, are shown only in Figure 2.4 (dashed lines) (Harris & Ripepe, 2007). The maximum values were selected for further discussion because they are most consistent with ground-based estimates made during Phases 1, 2, and 3 and observations of the dome suggesting growth was primarily endogenous during those phases of the eruption, which agrees with the cooler T_h value (Ratdomopurbo et al., 2013). The maximum extrusion rate derived from a single MODIS image was 7.5 m^3 s^{-1}, on June 2, 2006, and the maximum 5-point running average was 5.0 m^3 s^{-1}, on June 4. I calculated an erupted volume of 8.4 Mm^3 DRE of juvenile lava for the entire eruption (Figure 2.4; Table 2.1), and average extrusion rates for Phases 1 through 5 of 0.2, 0.7, 3.6, 0.7, and 1.6 m^3 s^{-1} (Figure 2.4; Table 2.1).

In the manner introduced above in Figures 2.2a and 2.2b, I plot the radiance data for Phases 1-4 in Figure 2.5a and the ratios in Figure 2.5b. These regime diagrams allow me to qualitatively classify the eruption activity and track the eruption in time. The first point to note is that the data from individual phases generally cluster together in the same

regions of each regime diagram. However, the pixel count-mean plot (Figure 2.5a) better differentiates activity style than the ratio plot (Figure 2.5b). Nonetheless, both Figures 2.5a and 2.5b show that Phase 1 consisted of slow growth of the lava dome (blue regions) before the dome increased in size and a small coulee flow or rockfall deposit formed, marking the beginning of Phase 2 (red regions). It was during Phase 2 that the first PDC occurred as the edges of the growing dome became gravitationally unstable and collapsed (Ratdomopurbo et al., 2013). This activity is identifiable in the corresponding thermal data in Figure 2.5a, as the data points generally progress in time from the pure dome region into the mixed dome and PDC deposit regions, indicating increasing lava dome and PDC activity. The peak of the extrusion rate occurred in Phase 3 (magenta regions) as dome growth continued and lava extended further from the vent and generated multiple large PDCs (Ratdomopurbo et al., 2013). In the regime diagrams of both Figures 5a and 5b, the corresponding MODIS radiance data extends as expected into the upper-right quadrant. As the rate of magma supply decreased, the dome cooled and PDCs became smaller and more infrequent in Phase 4, as indicated by the cyan regions in the bottom-left quadrants of both plots, representing cooler and smaller anomalies.

In contrast to Phases 1-4, Phase 5 includes multiple types of activity (Figure 2.6), so I consider this data separately from that of Phases 1-4. The complete collapse of the southern crater wall on June 14 (start of Phase 5) created a new gravitational instability in the dome leading to the collapse of the old edifice and of the new dome, generating the largest PDCs of the 2006 Merapi eruption (Charbonnier & Gertisser, 2008). The variability in Phase 5 is due to large but increasingly infrequent PDCs and simultaneous dome growth that continued after the June 14th PDCs (Ratdomopurbo et al., 2013). The

varying size and style of activity during Phase 5 is illustrated by the data points in Figure 2.6 occupying multiple regimes, though a general cooling trend exists as the eruption waned.

The ASTER images generally corroborate the observations extracted from the MODIS images. The interpretation of MODIS thermally anomalous pixel counts and means (Figure 2.5a) agree with the ASTER images (Figure 2.3) that show the size of the lava dome and its associated PDC deposits increased as the eruption progressed. On April 28th (Figure 2.3a), the ASTER image shows a small dome, as predicted by both regime diagrams (Figures 2.5a and 2.5b, blue stars). The May 14th ASTER image (Figure 2.3b) shows a dome and small PDC deposit, again consistent with both regime diagrams (Figures 2.5a and 2.5b, red stars). The May 30th (Figure 2.3c) and June 6th (Figure 2.3d) ASTER images show continued dome-growth and increasing PDC runout distances, as predicted by the MODIS analysis (pink stars, Figures 2.5a and 2.5b). Phase 5 MODIS images in Figure 2.6 (green stars) also agree with the ASTER images, showing a large hot dome with a PDC deposit on June 15th (Figure 2.3e) and June 22nd (Figure 2.3f) and a dome with a smaller hot deposit on July 8th (Figure 2.3h). The pixel count method (Figure 5a) is not always effective, as MODIS identifies only a hot lava dome on July 1st (Day 182, Figure 2.6) whereas the corresponding ASTER image (Figure 2.3g) clearly shows a PDC deposit in addition to the dome at the summit and data from the Global Volcanism Program (2007) report multiple PDCs occurred on that day. However, the temperatures derived from Band 10 of the ASTER image indicate that the deposit is cooler than similar deposits captured in other ASTER images, which may explain the discrepancy.

Looking closely at the data in Figure 5a allows the progression of the eruption during Phases 3-4 to be tracked (Figure 2.7). This visualization of the TIR data, starting with Phase 3, shows a period of dome growth and small PDCs, lava avalanches, or coulee growth (days 148-152, May 28-June 1, path A) immediately following the May 27 earthquake. On or just before day 153 (Figure 2.7, June 2, path B), the dome became unstable and collapsed, creating large PDCs. After this collapse the dome continued to grow and PDCs remained frequent (days 155-159, June 4-10, path C). This period was followed by cooling of the dome and a decrease in PDC frequency (days 161-164, June 10-14, path D) during Phase 4. The sequence of activity shown in Figures 2.4-2.7 indicates this was a Merapi-type eruption (Voight et al., 2000) where increased PDC activity resulted from a brief increase in extrusion rate. The conclusions drawn from Figure 2.7 agree with ground observations made during the eruption (Global Volcanism Program, 2007), which also identify large dome collapse and PDC events on June 2 (Julian day 153) and June 9-10 (Julian days 160-161).

2.4. Discussion

The extrusion rates, erupted volumes, and activity styles determined from MODIS TIR images (Figures 2.4-2.6, Table 2.1) agree well with previous ground- (Ratdomopurbo et al., 2013; Preece et al., 2013) and satellite-based (Harris & Ripepe, 2007) observations of the 2006 eruption of Merapi. For Phases 2 and 3 of the eruption (Figure 2.4, Table 2.1) I find average extrusion rates of 0.7 and 3.6 $m^3 s^{-1}$ compared to 0.54 and 1.27 $m^3 s^{-1}$ for Harris & Ripepe (2007) and 1.9 and 3.3 $m^3 s^{-1}$ for Ratdomopurbo et al. (2013). The satellite data (this study and Harris & Ripepe, 2007) underestimate the

rates compared to the photographic estimates of Ratdomopurbo et al. (2013) in Phase 2, likely because new lava was extruding beneath the cooled crust of an older dome, resulting in lower than expected radiance for dome growth activity. My estimate of the average extrusion rate during the Phase 3 eruption peak is closer to the ground-based visual observations than that of Harris & Ripepe (2007), primarily because my data set includes all cloud-free MODIS images acquired during the eruption, whereas Harris & Ripepe (2007) used only the MODIS pixels identified as volcanic thermal anomalies by the MODVOLC algorithm (Wright et al., 2004).

I applied my methods for analyzing MODIS images to the ASTER images as well. Calculated extrusion rates from both instruments were similar, but raw radiance data methods (Figure 2.5) using ASTER thermal bands proved less useful due to their 97 °C saturation temperature, which saturated pixels associated with all types of activity and therefore limited the ability of my method to distinguish activity styles. While ASTER has many qualitative and quantitative applications to monitoring volcanism (e.g., Rose & Ramsey, 2009), ASTER cannot be used to construct a meaningful continuous time series in the case of rapid lava dome growth due to its long repeat interval. ASTER is best utilized as a visual check on the results of the MODIS analysis described here.

For the entire 2006 eruption period, I calculate a total volume of extruded magma of 8.4 Mm^3 DRE (Figure 2.4). I do not extrapolate an average extrusion rate over days with missing data to avoid overestimation, so this volume estimate potentially represents a lower bound. My value lies between the estimate of 5.3 Mm^3 DRE total erupted magma based on ground-based photographic methods (Ratdomopurbo et al., 2013), and the estimate of 13.3 Mm^3 DRE total PDC deposit volume (which includes non-juvenile

material) (Charbonnier & Gertisser, 2008). Before the crater wall began to collapse significantly on June 9th (Ratdomopurbo et al., 2013), volume estimates were dominated by lava extrusion, and Ratdomopurbo et al. (2013) report a total volume of 5.3 Mm^3 magma extruded through June 8 (end of Phase 3), compared to the 4.5 Mm^3 calculated for the same period in this study (Table 2.1). My estimates are reasonably consistent with the ground-based numbers through June 8th and also agree with the total volume of extruded magma estimate of 8 Mm^3 of Walter et al. (2007). Based on my calculations, I suggest that an additional ~4 Mm^3 DRE of lava was extruded during Phases 4 and 5.

My data suggest that this eruption sequence represents a single pulse of high lava ascent rate leading to growth of the lava dome (Phases 1-4) followed by a period of variable ascent rates related to slower dome growth and less frequent PDCs (Phase 5). I suggest that the variable extrusion rates during Phase 5 are most likely caused by the unloading of the underlying conduit as a result of dome collapse (as suggested by Melnik & Sparks, 1999 for the Soufrière Hills volcano, Montserrat). These conclusions are consistent with the work of Preece et al. (2013), who examined textures of samples from the 2006 eruption and found evidence for high ascent rates from depth during the main stage of the eruption followed by variable ascent rates and temporary shallow storage of magma (~2 km below the vent) in the later stages of the eruption. The conduit unloading process related to dome collapse offers a potential explanation for the variable ascent rates and temporary storage of magma during Phase 5 of the eruption described by Preece et al. (2013). According to this model, ascent rates increase following a dome collapse and corresponding unloading, leading to higher extrusion rates as the dome rebuilds. The rebuilding of the dome and corresponding increase in overburden eventually slows

magma ascent and leads to temporary magma storage at shallow depth until the next dome collapse.

The satellite thermal dataset tracks the varying intensity of the eruption well, such that significant changes in calculated extrusion rate or extrusion rate slope correspond within a day or two of transitions between eruption phases (dashed vertical lines, Figures 2.4 and 2.8) identified by Ratdomopurbo et al. (2013) or alert levels as determined by the Merapi Volcano Observatory and reported by the Global Volcanism Program (2007). Furthermore, this detailed record of extrusion rate, combined with PDC data, supports previous suggestions that the frequency and size of PDCs during dome-building eruptions correlate with extrusion rate (e.g., Nakada et al., 1999; Calder et al., 2002). Despite some data gaps, trends in PDC frequency (numbers of PDCs per day extracted from seismic records and reported by the Global Volcanism Program, 2007; Walter et al., 2007; Ratdomopurbo et al., 2013), closely follow extrusion rate trends (Figure 2.8), supporting the idea that PDC activity generally increases during periods of high extrusion rate, when the size and instability of the dome are expected to increase.

The 2006 Merapi eruption also points to other possible mechanisms of increasing the likelihood of dome-collapse PDCs. Despite low extrusion rates, peaks of PDC events per day (Figure 2.8) occur in both mid-May and mid-June. I suggest that the mid-May peak in PDC activity is due to new lava dome growth destabilizing and collapsing the old dome during Phase 2. The mid-June peak is due to the collapse of the southern crater wall and destabilization of the new dome, marking the onset of the renewed activity of Phase 5 (Global Volcanism Program, 2007). PDC occurrences also increased immediately following the May 27th M_w 6.4 earthquake, as originally noted by Walter et al. (2007)

(vertical line, second from left, Figure 2.8). Extrusion rate increased for a 13-day period following the earthquake (Phase 3) and Preece et al. (2013) show that magma ascent rates were highest in the two weeks following the earthquake as Ill. Previous work modeling stress changes caused by the earthquake (Walter et al., 2007) shows that corresponding static stress changes can not account for the increased ascent rates, but a concurrent increase in activity at Semeru Volcano 260 km to the east (Harris & Ripepe, 2007) suggests that dynamic stress changes due to the passing of seismic waves through the volcano plumbing system may have affected the eruption (e.g., Manga & Brodsky, 2006). Future work is necessary to explore if changes at depth, such as an increase in pressure or in the proportion of volatile phases, possibly caused by the earthquake, can explain the duration and elevated ascent rate of Phase 3, or if the earthquake was a small effect superimposed onto an existing trend of increasing activity.

2.5. Conclusions

The method for calculating extrusion rate from satellite thermal images developed by Pieri & Baloga (1986), Harris et al. (1997; 2003), Harris & Ripepe (2007) and Harris & Baloga (2009) is further validated by this study. While more accurate temperature measurements and differentiation between lava and PDC contributions to the thermal signal would improve accuracy, the method functions as a reliable first-order estimate of extrusion rate. The steady-state and cooling-limited assumptions required to solve eq. 2.1 are also appropriate in the Merapi case, despite a crater-filling dome and lava extending down the steep flanks of the volcano. My use of a background subtraction to remove atmospheric effects is a simple and possibly more accurate solution compared to

MODTRAN atmospheric modeling, and I demonstrate that it provides extrusion rate measurements sufficiently reliable to monitor and understand dome-building activity.

I show that the activity style of a dome-building eruption can be differentiated using MODIS data. Plotting the pixel mean radiance against pixel count of a thermal anomaly allows differentiation between anomalies caused by lava domes and PDC deposits. This regime diagram also differentiates between anomalies with flows of various sizes (coulees, rock avalanches, small and large PDCs) with or without a strong lava dome signal. This method can be automated for a given volcano to track eruption style over time and can be especially useful for poorly observed eruptions or in retrospect to obtain a denser time series record of an eruption. Further manual analysis in the form of pixel radiance histograms can be used to extract additional details about the type of activity in a given MODIS scene.

These methods produced a detailed record of extrusion rate and activity style at Merapi during the 2006 eruption. Five phases are discernable by satellite and agree with the timing of phases determined by ground-based observations. The peak of the eruption occurred in the two weeks following a regional tectonic earthquake on May 27th. While this and previous works suggest the two are related, additional study is required to determine the significance of the earthquake's influence on the eruption. I show that the occurrence of PDCs is positively correlated with extrusion rate during this Merapi dome-building eruption. Monitoring extrusion rate using these methods can therefore provide information about periods of increasing or decreasing PDC hazards.

Other factors control PDC occurrence as well, as seen in Phases 2 and 5 when collapses of the old dome and crater, respectively, resulted in sharp increases in the

number of PDCs as well as increases in extrusion rate. Numerical modeling by Melnik & Sparks (1999) and petrologic evidence from Preece et al, (2013) suggest that conduit unloading due to dome collapse can increase magma ascent and extrusion rates, though understanding of the detailed effects of this relationship will benefit from additional studies. Satellite TIR data provide useful and necessary data for monitoring volcanic eruption hazards and provide a point of comparison for studies of the internal and external factors controlling extrusion rate during an effusive eruption.

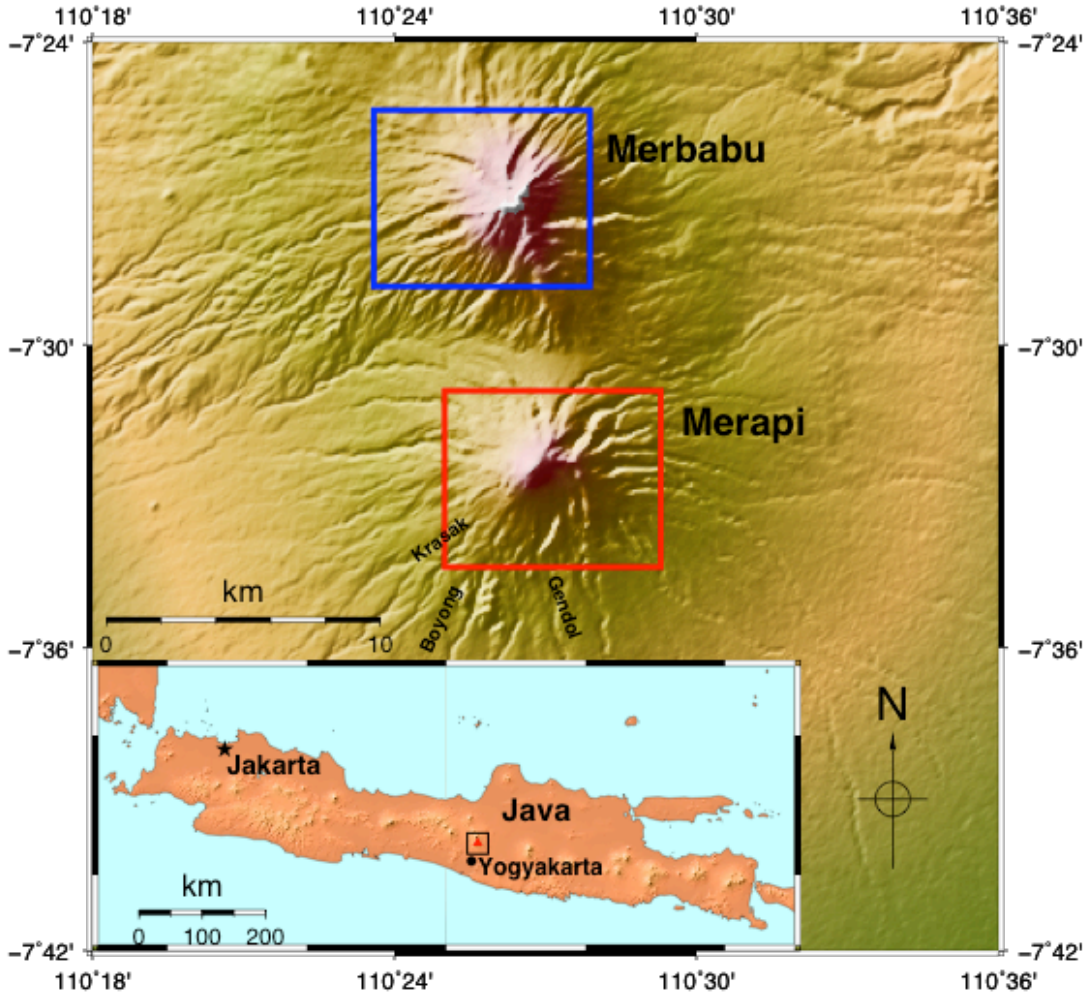

Figure 2.1. Location of Merapi Volcano. Merapi and Merbabu Volcanoes, showing the regions of interest (ROIs) that were used for the extrusion rate calculations (red box) and background subtraction (blue box), and the primary PDC drainages for the 2006 eruption (Krasak, Boyong, & Gendol). **Inset:** location of the main figure (box) and Merapi (triangle) on the island of Java, showing the proximity of Merapi to the city of Yogyakarta.

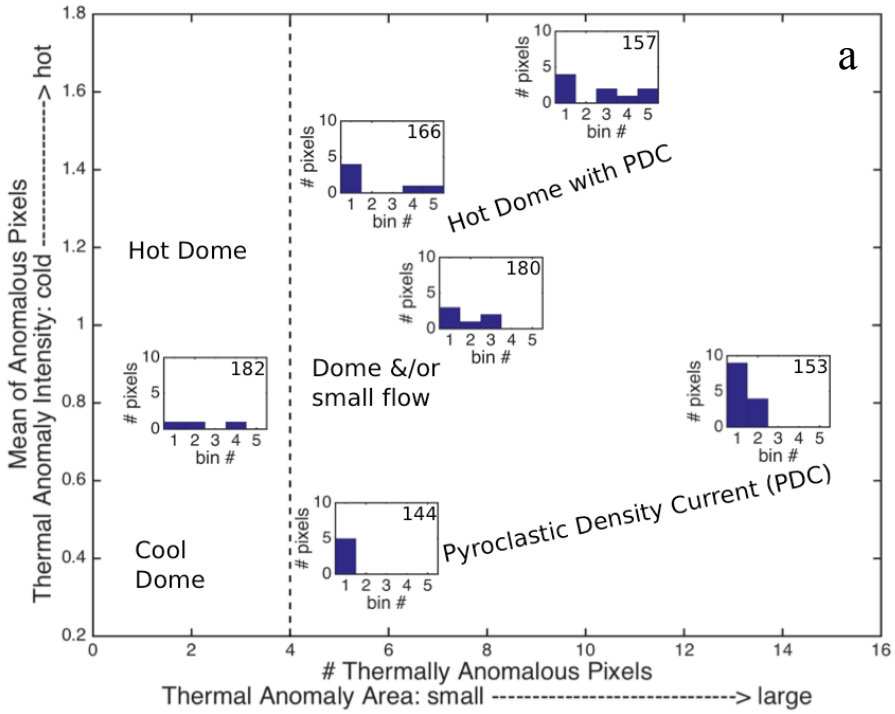
a
Mean of Anomalous Pixels
Thermal Anomaly Intensity: cold ----------> hot
Thermally Anomalous Pixels
Thermal Anomaly Area: small ----------> large
Hot Dome
Hot Dome with PDC
Dome &/or
small flow
Cool
Dome
Pyroclastic Density Current (PDC)
pixels
bin #
157
166
180
182
153
144

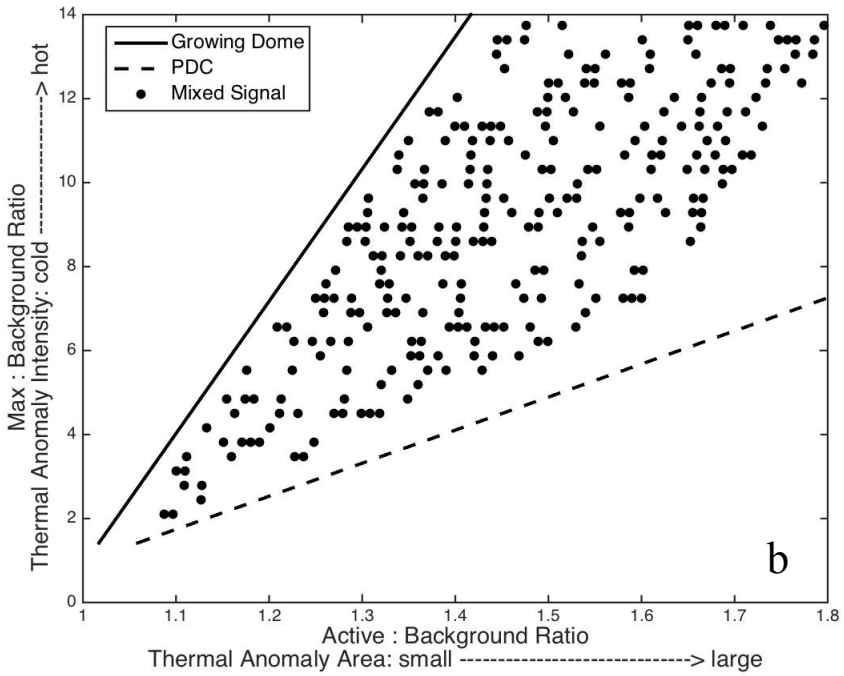
b
Growing Dome
PDC
Mixed Signal
Max : Background Ratio
Thermal Anomaly Intensity: cold ----------> hot
Active : Background Ratio
Thermal Anomaly Area: small ----------> large

Figure 2.2 (previous page). Volcanic activity style from MODIS thermal anomalies. **(a)** The labels indicate where activity types are located in a plot of thermally anomalous pixel count vs. the mean of those pixels. The term "small flow" indicates either a coulee or a small lava avalanche. Given that the maximum dome radius in 2006 was ~150 meters (Ratdomopurbo et al, 2013), a maximum of four pixels can be attributed to the thermal anomaly caused by the dome, as shown by the dashed vertical line. Insets are histograms of thermally anomalous pixel radiances (in W/(m^2 mm sr), where $0.5 < \text{bin } 1 \leq 1.0$, $1.0 < \text{bin } 2 \leq 1.5$, $1.5 < \text{bin } 3 \leq 2.0$, $2.0 < \text{bin } 4 \leq 2.5$ and $\text{bin } 5 > 2.5$. The number in the upper right of the histograms is the Julian day of the MODIS image. **(b)** Modeled lines show where PDC deposit and lava dome signals will likely fall in a plot of the active:background and max:background ratios. The dots are modeled ratio values for mixed thermal signals with pixels representing both dome and PDC activity.

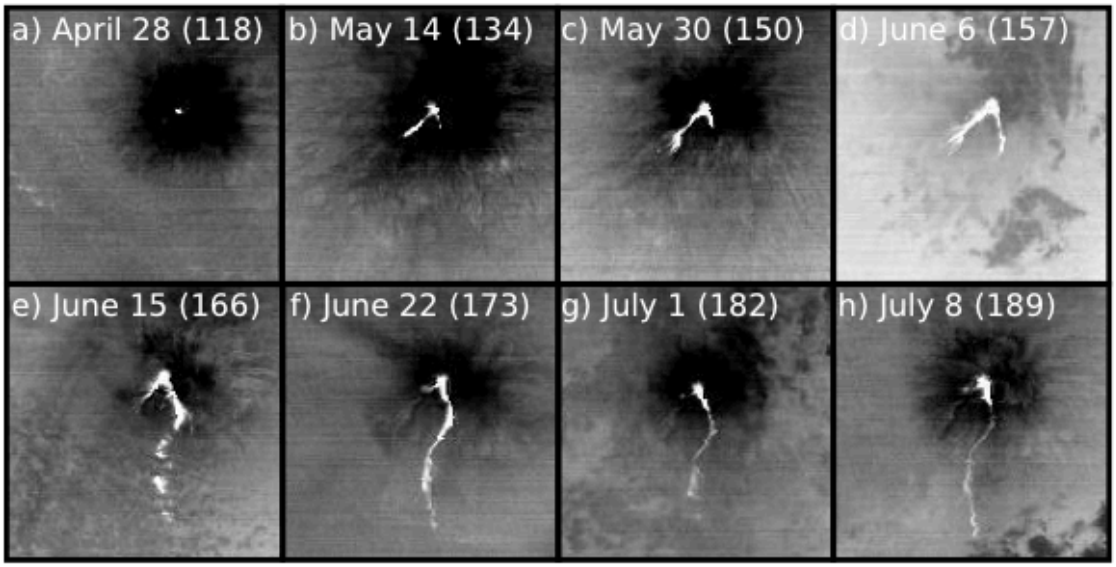

Figure 2.3. Merapi ASTER images. ASTER Band 10 (bandwidth = 8.125-8.475 μm) images of Merapi during the 2006 eruption. The number in parentheses is the Julian Day.

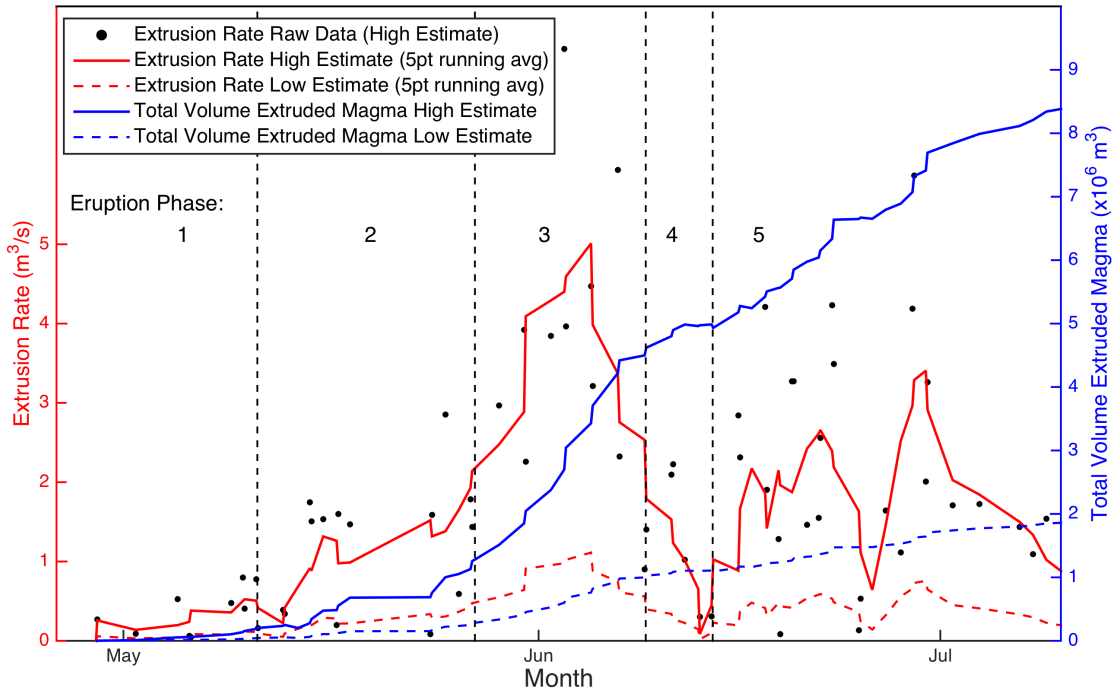

Figure 2.4. MODIS extrusion rate and volume for Merapi. Extrusion rate (left axis and red lines) and total volume of magma extruded (right axis and blue lines) calculated from MODIS data for the 2006 Merapi eruption. The lines are 5-point running averages of the raw data (black dots). High (solid lines) and low (dashed lines) estimates result respectively from minimum and maximum values used for temperature variables in eqs. 2.3 & 2.4.

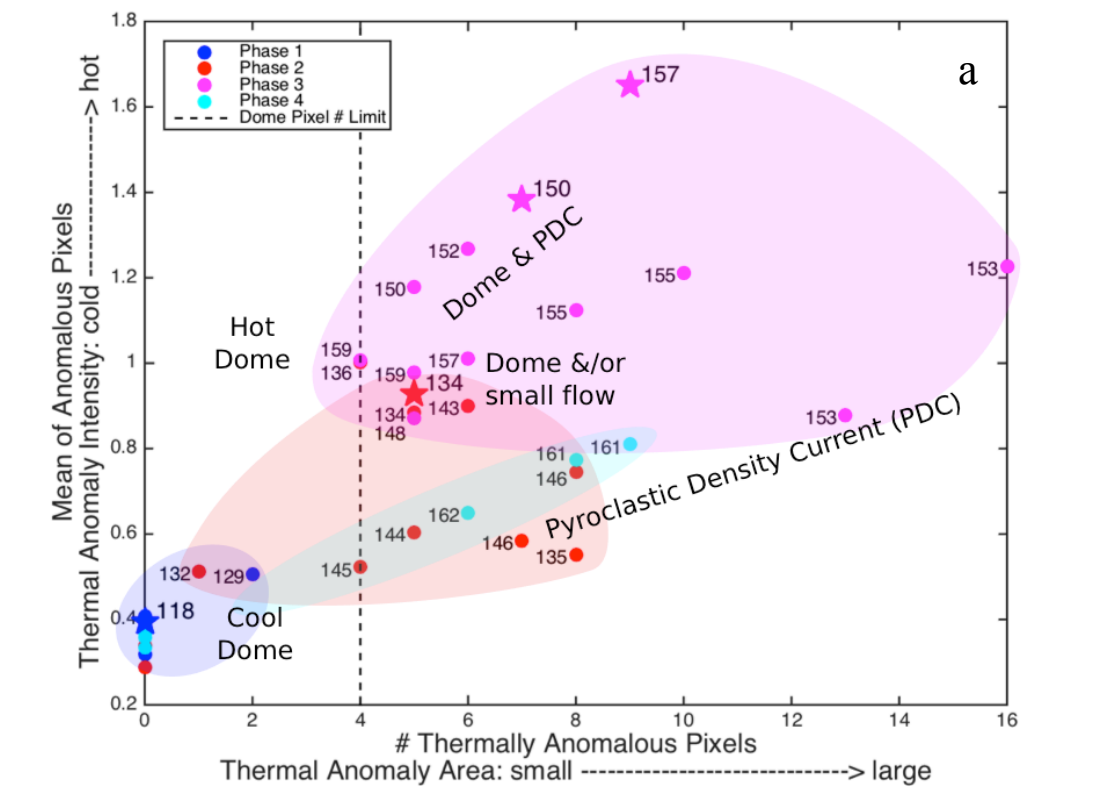
a
Phase 1
Phase 2
Phase 3
Phase 4
Dome Pixel # Limit
Mean of Anomalous Pixels
Thermal Anomaly Intensity: cold ----------> hot
Thermally Anomalous Pixels
Thermal Anomaly Area: small ----------> large
Hot Dome
Dome & PDC
Dome &/or small flow
Pyroclastic Density Current (PDC)
Cool Dome

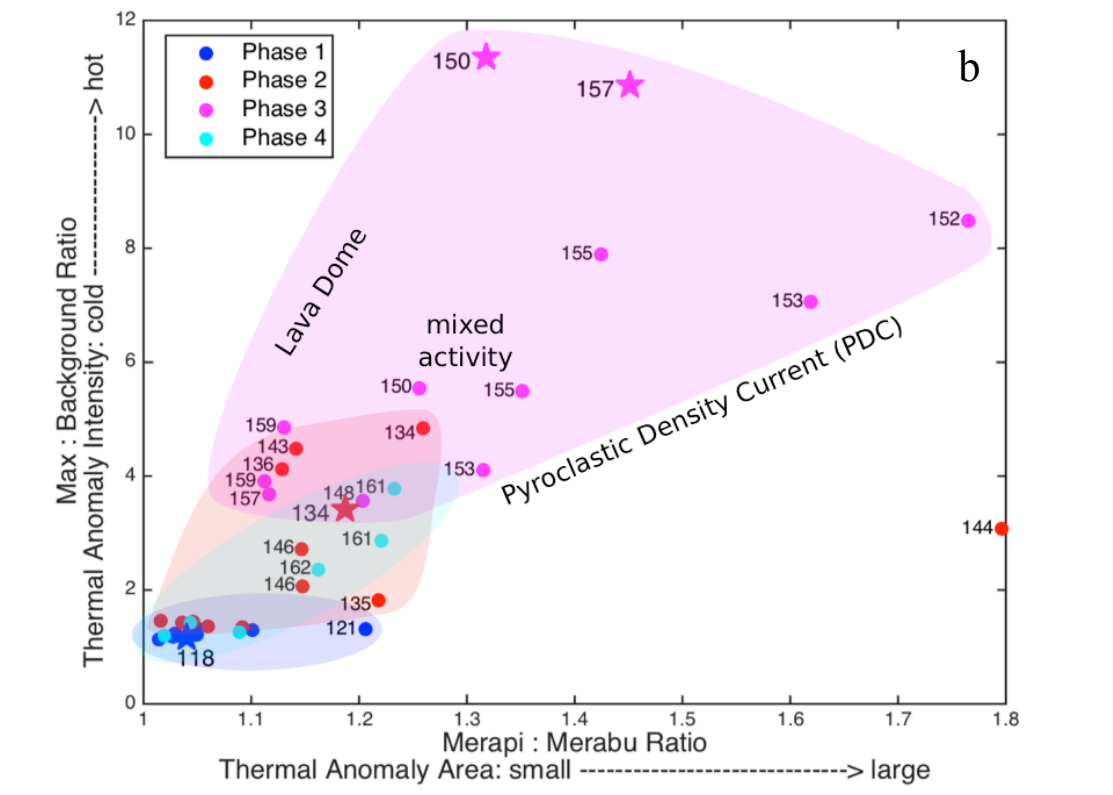
b
Phase 1
Phase 2
Phase 3
Phase 4
Max : Background Ratio
Thermal Anomaly Intensity: cold ----------> hot
Merapi : Merabu Ratio
Thermal Anomaly Area: small ----------> large
Lava Dome
mixed activity
Pyroclastic Density Current (PDC)

Figure 2.5 (previous page). MODIS-derived activity style for Merapi. **(a)** Thermally anomalous pixel count vs. pixel mean radiance and **(b)** active:background vs. max:background ratios for each MODIS image from Phases 1-4. Polygons enclose images from each phase. Image labels are Julian Day of image acquisition. Stars represent images that have a simultaneous ASTER image (see Figure 2.3 for corresponding Julian Days).

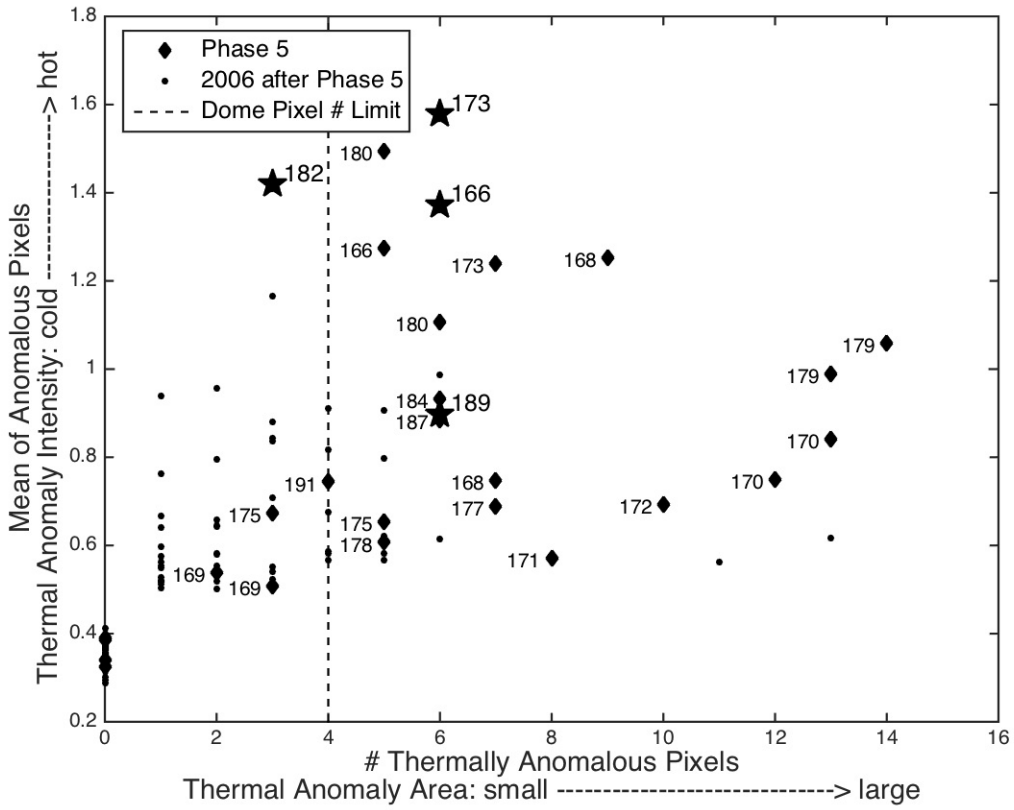

Figure 2.6. Activity style for eruption Phase 5. Thermally anomalous pixel count vs. pixel mean radiance for MODIS images from Phase 5 of the 2006 Merapi eruption. Image labels are Julian Day of image acquisition. Stars are images that have a simultaneous ASTER image (see Figure 2.3 for corresponding Julian Days). Black dots are MODIS images from after Phase 5.

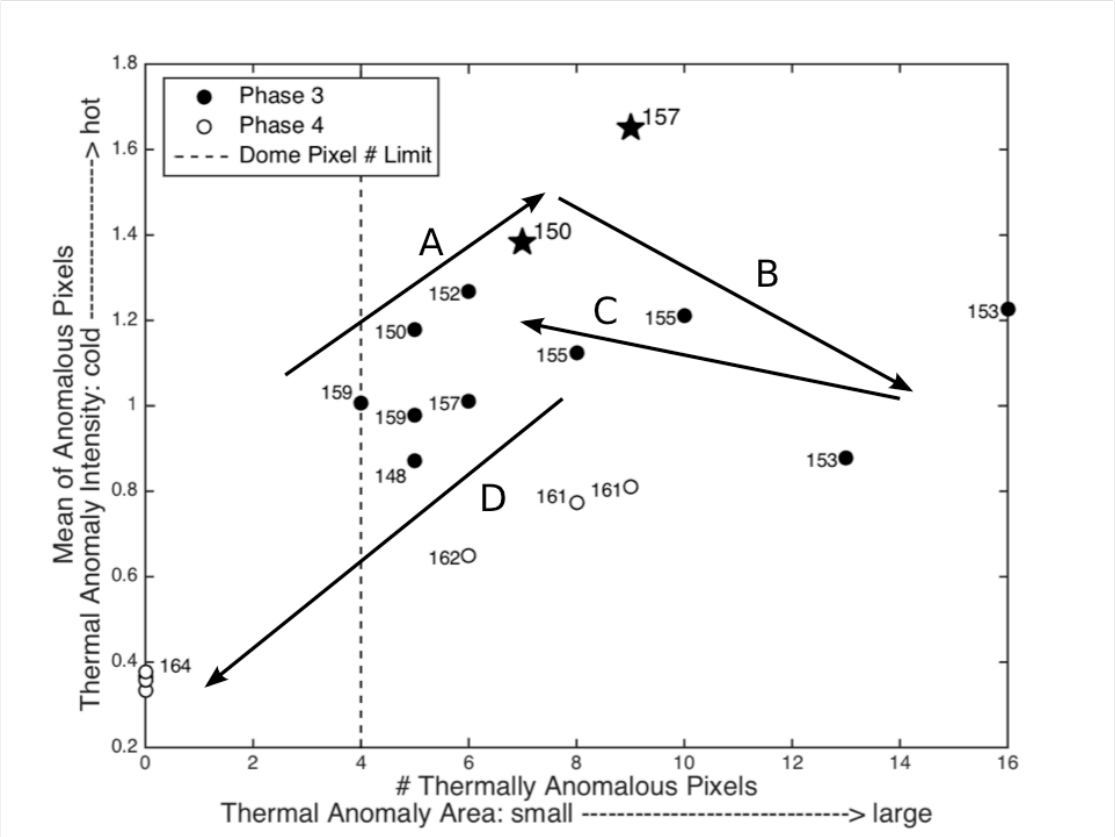

Figure 2.7. Observing changes in eruption style with MODIS. Mean and number of thermally anomalous MODIS TIR pixels during Phases 3 and 4 of the 2006 Merapi eruption. Data points are labeled by Julian day; see Figure 2.5a for eruption style labels. The lettered arrows show documented trends of activity during Phases 3-4, see text for details.

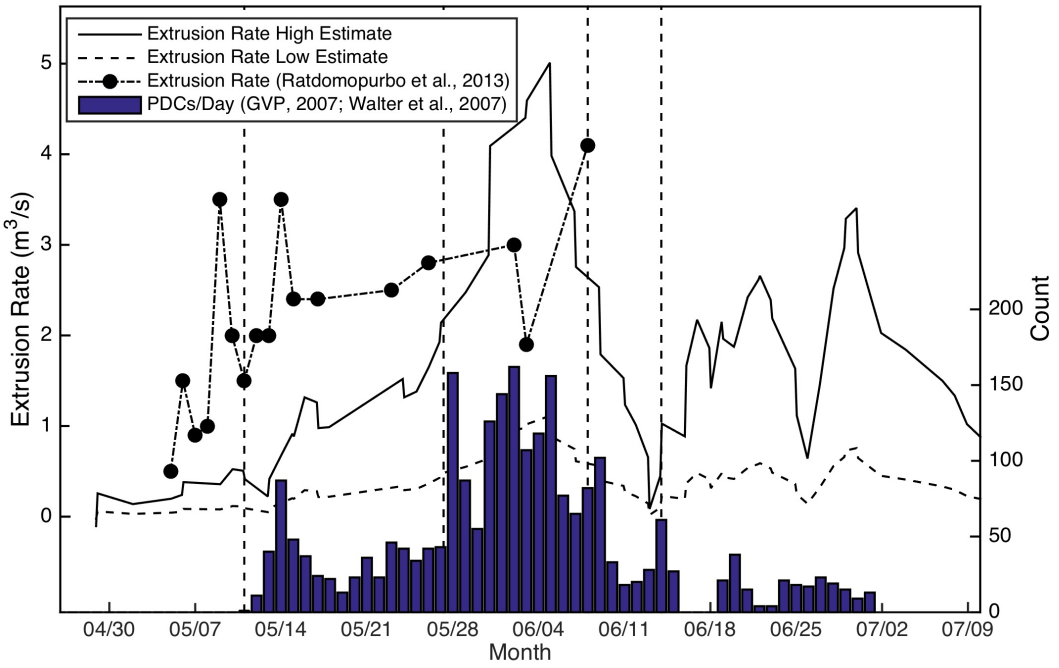

Figure 2.8. PDC correlation to eruption rate. The eruption rate and phase boundary data from Figure 2.4 compared to PDC count data from the Global Volcanism Program (2007) and Walter et al. (2007), and extrusion rate data from Ratdomopurbo et al. (2013). High eruption rates correspond to high frequency of PDCs.

			Extrusion Rate (m^3/s)				Cumulative Volume Extruded (10^6 m^3)			
Phase	**Dates**	Activity	This Study	Ratdomopurbo et al., 2013	Harris & Ripepe, 2007	BGVP	This Study	Ratdomopurbo et al., 2013	Harris & Ripepe, 2007	BGVP
1	**April 26 - May 10**	Initial dome growth	0.2	1			0.2	1.0		
2	**May 11 - May 26**	First pyroclastic flows observed	0.7	1.9	0.54		1.3	2.6	0.5	2.3
3	**May 27 - June 8**	Peak of activity following 5/27 6.4M_w EQ	3.6	3.3	1.27	1.16	4.5	5.3	1.6	4.0
4	**June 9 - June 13**	Significant decrease in activity	0.7		0.94		4.9		2.0	
5	**June 14 - July 10**	Renewed pyroclastic flow activity then decreases until alert level lowered	1.6				8.4			
Total			**1.6**				**8.4**	**5.3**		

Table 2.1. Extrusion rate and volume for the 2006 eruption of Merapi. Average extrusion rates and volume of magma extruded compare well with previous works based on both remote sensing and ground-based estimates. This is the case for each phase of the eruption and for the entire eruption. BGVP stands for Bulletin of the Global Volcanism Program (2007).

CHAPTER 3

EXTRUSION RATE VARIATIONS DURING DOME-FORMING ERUPTIONS: A NUMERICAL MODELING APPROACH TO THE 2006 ERUPTION OF MERAPI VOLCANO (INDONESIA)

Extrusion rates during lava dome-building eruptions are variable and eruption sequences at these volcanoes generally have multiple phases. I apply a 1D, steady-state numerical model of magma ascent in a volcanic conduit to explain the extrusion rate variations observed during the 2006 dome-forming eruption of Merapi Volcano, Java, Indonesia. Merapi is one of Indonesia's most active volcanoes and during the 20th and early 21st centuries effusive activity was characterized by long periods of low (< 0.1 m^3 s^{-1}) extrusion rate interrupted every few years by short episodes of elevated extrusion rates (1 – 4 m^3 s^{-1}) lasting weeks to months. One such event occurred May – June 2006, and previous research has identified multiple phases with different styles of activity during the eruption. Using input values established in the literature, I apply the model to interpret changes in observed extrusion rates and gain insight into corresponding conduit processes. The peak phase of the 2006 eruption occurred in the two weeks following the May 27 M_w 6.4 earthquake 50 km to the south. Previous work has suggested that the peak extrusion rates observed in early June were triggered by the earthquake through either dynamic stress-induced overpressure or addition of CO_2 due to decarbonation and gas escape from new fractures in the bedrock. I show that the overpressure increase must be on the order of 5 MPa or the volatile increase on the order of 1.7 wt. % to account for the observed increase in extrusion rate. A time-series of extrusion rate shows that the rate

increased suddenly four days following the earthquake. I explain this delay by the combined time required for the effects of the earthquake to develop in the deep system (1-2 days), and the time I calculate here for the affected magma to ascend from storage zone to surface (38 – 48 hours). The inflated extrusion rate was sustained for 2-7 days before dissipating and returning to pre-earthquake levels. The final phase of the 2006 eruption was characterized by highly variable extrusion rates. I demonstrate that those changes were likely controlled by large dome collapses that were precipitated by failure of the edifice that had been confining the dome to Merapi's crater. The corresponding reductions in dome height caused increased extrusion rates that helped to rebuild the dome and lead to further collapses, a feedback cycle that prolonged the eruption even as magma supply rates returned to background levels.

3.1. Introduction

Merapi Volcano is one of Indonesia's most active and dangerous volcanoes. Located 30 km north of Yogyakarta in central Java (Figure 3.1), the primary hazard to the surrounding population is pyroclastic density currents (PDCs) caused by collapse of an active lava dome at the summit (Voight et al., 2000). While the size and frequency of PDCs generally correlates with the extrusion rate (Nakada et al., 1999; Calder et al., 2002), and periods of increased extrusion rate can be anticipated through extensive geodetic and seismic monitoring (e.g. Surono et al., 2012; Ratdomopurbo et al., 2013), the causes of changes in the extrusion rate are not well constrained for individual eruptions. Numerical models of magma ascent in a volcanic conduit can test the effect different parameters have on the extrusion rate, such that general relationships between a

range of magma and conduit parameters have been well described (Melnik & Sparks, 1999; Mastin, 2002; de' Michieli Vitturi et al., 2008; 2010). However, these relationships can be applied only to determine the cause of varying extrusion rates in real eruptions for specific cases where the system is sufficiently well-constrained to reduce the number of free parameters. Numerous eruptions at Merapi are well documented, making them excellent case studies for the application of numerical models of volcanic processes. In this chapter I apply a conduit model with inputs well-constrained for the 2006 effusive eruption and pair it with a detailed record of extrusion rate (Harris & Ripepe, 2007; Ratdomopurbo et al., 2013; Chapter 2, this dissertation) to explain the causes of variable activity during the multiple phases of the 2006 eruption sequence.

3.1.1. Merapi's activity

For much of the late 19th, 20th, and early 21st centuries, activity at Merapi Volcano consisted of continued slow extrusion leading to the formation of a series of lava domes (Voight et al., 2000). The long-term background extrusion rate at Merapi is approximately 0.03 m^3 s^{-1} (Siswowidjoyo et al., 1995). Every few years (an average of <7 years, Ratdomopurbo et al., 2013) extrusion rates have increased to 1-4 m^3 s^{-1} during short-lived periods of increased activity of a few weeks to months when PDCs have been most common (Siswowidjoyo et al., 1995). This pattern of low-level background activity interrupted by relatively brief periods of increased extrusion rate and PDC frequency was so persistent at Merapi that it has been described as "Merapi-type" activity and the term is used to describe similar eruptions at other volcanoes (Voight et al., 2000).

Observations and studies of the 2006 eruption have identified five phases (Global Volcanism Program, 2007; Harris & Ripepe, 2007; Ratdomopurbo et al., 2013; Preece et al., 2013; Chapter 2, this dissertation). Phase 1 began on April 26 when lava extrusion increased above background levels (Ratdomopurbo et al., 2013), though extrusion rates were ≤ 1 m^3 s^{-1} (Ratdomopurbo et al., 2013; Chapter 2, this dissertation). Extrusion rate increased to ~2 m^3 s^{-1} during Phase 2, which began on May 11 with the first PDCs generated by dome collapse (Ratdompurbo et al., 2013; Preece et al., 2013). The start of Phase 3 is marked by a M_W 6.4 strike-slip earthquake at a depth of 10 km located ~50 km S of Merapi (7.89° S, 110.41° E) that occurred on May 27 and caused thousands of fatalities around Yogyakarta (Nakano et al., 2006). Immediately following the earthquake the frequency of PDCs increased and the extrusion rate rose to 3-3.5 m^3 s^{-1} for a period of nearly two weeks (Ratdomopurbo et al., 2013; Preece et al., 2013). This increase was followed by a brief decrease in activity during phase 4 (June 9 – 13) when extrusion rates returned to ~1 m^3 s^{-1} (Harris & Ripepe, 2007; Chapter 2, this dissertation). The mass of the growing lava dome initiated a progressive failure of the southern crater wall during Phases 3 and 4 (Ratdomopurbo et al., 2013). This failure caused the primary direction of PDCs to switch from the SW down the Krasak and Boyong drainages to the S down the Gendol drainage (Charbonnier & Gertisser, 2008; Ratdomopurbo et al., 2013) (Figure 3.1). The start of Phase 5 is marked by the final and complete collapse of the crater wall on June 14, leading to the largest PDCs of the 2006 event which traveled up to 7 km from the vent and caused the only two fatalities directly attributed to the eruption (Charbonnier & Gertisser, 2008). Extrusion rates were variable during this phase, ranging from 1-2 m^3 s^{-1} (Preece et al., 2013; Chapter 2, this dissertation). I mark the end of Phase 5 on July 10,

when the Indonesian Center of Volcanology and Geological Hazards Mitigation lowered the alert level for Merapi from 4 to 3 (on a 1-4 scale) (Global Volcanism Program, 2007).

Previous research has suggested that the peak extrusion rate during Phase 3 is related to the occurrence of the May 27 earthquake (Walter et al., 2007; Harris & Ripepe, 2007; Troll et al., 2012). While the static stress change caused by the earthquake was not strong enough to apply a pressure change to the Merapi magmatic system sufficient to increase extrusion rate, the dynamic stress change caused by passing seismic waves likely played a role (Walter et al., 2007). The effect of dynamic stress change is further supported by Harris and Ripepe (2007) who identify an increase in extrusion rate at both Merapi and Semeru Volcano (280 km to the east) in the days following the earthquake. Both Harris & Ripepe (2007) and Walter et al. (2007) suggest that dynamic stress may cause increased vesiculation and promote bubble growth in the magma which leads to increased pressure and buoyancy in the magma chamber and higher extrusion rates (Manga & Brodsky, 2006). Deegan et al. (2010) and Troll et al. (2012) propose a different mechanism, noting that the crustal contribution to CO_2 emissions at Merapi increased following the earthquake. They suggest that the earthquake may have promoted increased release of CO_2 from the carbonate bedrock at mid- to upper crust depths into the Merapi magmatic system (Deegan et al., 2010), increasing the volatile content of the magma and promoting increased extrusion rates (Troll et al., 2012).

3.1.2. Numerical modeling of volcanic conduits

Multiple numerical models of volcanic conduits of varying complexity have been developed over the past decades to aid the understanding of both effusive and explosive

volcanic eruptions. These models treat the rising magma as a laminar two-phase flow of exsolved volatiles and melt that includes the liquid, crystals, and dissolved volatiles (e.g. Jaupart & Allègre, 1991; Woods & Koyaguchi 1994; de' Michieli Vitturi et al., 2008). Magma rise is driven by the pressure gradient between the chamber and the vent while being resisted by gravity and viscous forces. The viscosity of the magma is a factor of the exsolved volatile phase, temperature, dissolved volatiles, and the crystal content of the melt and can change rapidly with variations in any of these parameters (Lejeune & Richet, 1995; Hess & Dingwell, 1996). Jaupart & Allègre (1991) and Woods & Koyaguchi (1994) showed that lateral degassing through the conduit walls is an important process for determining whether an eruption is explosive or effusive, with enhanced lateral degassing promoting effusive eruptions and also the formation of dense plugs at the vent and cyclic eruptive activity (Diller et al. 2006; Clarke et al. 2007; de' Michili Vitturi et al., 2008; 2010). Overpressure in the chamber exerts a primary control on magma ascent rates and the intensity of activity observed at the vent (Woods and Koyaguchi, 1994). A lava dome at the vent decreases the pressure gradient and consequently decreases mass flow rates (Jaupart & Allegre, 1991; Woods & Koyaguchi, 1994; Melnik & Sparks, 1999).

3.2. Methods

The model I present here is derived from the theory of thermodynamically compatible systems (Romenski et al., 2010; La Spina et al., 2014) and applies to 1D, isothermal, multiphase, steady-state flow. It can be accessed at https://github.com/demichie/MAMMA. The model accounts for the effects of the main

processes controlling magma rise in a vertical conduit, such as crystallization, rheological changes, magma fragmentation, interaction with the conduit walls (viscous forces), outgassing, and degassing. The system is described as a mixture of two phases (i = 1, 2), each one characterized by a volumetric fraction (α_i), density (ρ_i), velocity (u_i), and specific entropy (s_i). Below the fragmentation level, phase 1 corresponds to a mixture of crystals, dissolved gas, and melts (continuous phase) while phase 2 is composed of the exsolved gas (dispersed phase). Above the fragmentation level exsolved gas (phase 2) constitutes the continuous phase while magma fragments are the dispersed phase. Each component of the system is characterized by a state equation, with the specific energy function of the density and entropy obtained by a linearized form of the Mie-Grüneisen equations. The pressure (p_i) of both phases is derived from the internal energy (e_i). With these assumptions, the system of conservation equations for the mixture mass, mass of phase 1, mixture momentum, and mixture energy is written as

$$\frac{\partial}{\partial z}\left(\rho u\right) = -Q_{lat} \tag{3.1}$$

$$\frac{\partial}{\partial z}\left(\alpha_1\rho_1 u_1\right) = \frac{1}{\tau^{(d)}}\left(x_d - x_d^{eq}\right)\alpha_1\left(\rho_1 - \beta\rho_c\right) \tag{3.2}$$

$$\frac{\partial}{\partial z}\left(\alpha_1\rho_1 u_1^2 + \alpha_2\rho_2 u_2^2 + \alpha_1 p_1 + \alpha_2 p_2\right) = -\rho g - \frac{8\mu_{mix}u}{R^2} - u_2 Q_{lat} \tag{3.3}$$

$$\frac{\partial}{\partial z}\left[\alpha_1\rho_1 u_1\left(e_1 + \frac{p_1}{\rho_1} + \frac{u_1^2}{2}\right) + \alpha_2\rho_2 u_2\left(e_2 + \frac{p_2}{\rho_2} + \frac{u_2^2}{2}\right) - \rho x_1 x_2\left(u_1 - u_2\right)\left(s_1 - s_2\right)T\right]$$
$$= -\rho g u - \frac{8\mu_{mix}u^2}{R^2} - Q_{lat}\left(\frac{u_2^2}{2} + c_{v,2}T\right) \tag{3.4}$$

where z is the vertical coordinate, ρ is the mixture density, u is the mixture velocity, Q_{lat} is the lateral degassing mass flux, $\tau^{(d)}$ is the characteristic time which controls the gas exsolution rate, x_d is the mass fraction of the dissolved gas, x_d^{eq} is the equilibrium value of the same parameter, β is the volume fraction of crystals, ρ_c is the density of crystals, g is the acceleration of gravity, μ_{mix} is the mixture viscosity, R is the conduit radius, x_i is the mass fraction of the phase i, and T is the mixture temperature.

The volume fraction of the liquid (melt, crystals, and dissolved gas) is governed by the following equation, accounting for the relaxation of phase pressure differences through the characteristic time $\tau^{(p)}$:

$$\frac{\partial}{\partial z}\left(\rho u \alpha_1\right) = \frac{1}{\tau^{(p)}}\left(p_2 - p_1\right) \tag{3.5}$$

The mechanical disequilibrium between the phases is modeled by the following balance law for the relative velocity:

$$\begin{aligned} &\frac{\partial}{\partial z}\left[\frac{u_1^2}{2} - \frac{u_2^2}{2} + e_1 + \frac{p_1}{\rho_1} - e_2 - \frac{p_2}{\rho_2}\rho_1 - \left(s_1 - s_2\right)T\right] \\ &= -\rho g - \chi_j \frac{8\mu_{mix} u}{\alpha_j \rho_j R^2} - \frac{x_1 x_2}{\rho \tau^{(f)}}\left(u_1 - u_2\right) + \frac{u_2}{\alpha_2 \rho_2} Q_{lat} \end{aligned} \tag{3.6}$$

where $\tau^{(f)}$ is the characteristic time which controls the degree of decoupling between the gas and liquid phases, j is the continuous phase index (1 or 2, a function of the relative position of the fragmentation level), while the parameter χ_j controls the sign of the viscous term contribution to the relative velocity (1 or -1, also a function of the continuous phase index). Below the fragmentation level, $\tau^{(f)}$ is defined in order to retrieve the Forchheimer's law to model the outgassing, while above the fragmentation level it is

defined in order to model the drag exerted by the gas on the fragmented particles of magma (Degruyter et al., 2012; La Spina et al., 2015).

Finally, the mass conservation laws for the crystals and dissolved gas are

$$\frac{\partial}{\partial z}\left(\beta\alpha_1\rho_c u_1\right) = \frac{1}{\tau^{(c)}}\left(\beta - \beta^{eq}\right)\alpha_1\rho_c \tag{3.7}$$

$$\frac{\partial}{\partial z}\left(x_d\alpha_1\left(\rho_1 - \beta\rho_c\right)u_1\right) = \frac{1}{\tau^{(d)}}\left(x_d - x_d^{eq}\right)\alpha_1\left(\rho_1 - \beta\rho_c\right) \tag{3.8}$$

where $\tau^{(c)}$ is the characteristic time of the crystallization process and β^{eq} is the equilibrium volume fraction of crystals.

As the magma rises, pressure decreases and causes exsolution of volatiles as the melt crystallizes, changing the density and viscosity of the melt (Hess & Dingwell, 1996). The evolving viscosity of the mixture, below the fragmentation level, is modeled as

$$\mu_{mix} = \mu_m \cdot \theta_1(\beta)\theta_2(\alpha) \tag{3.9}$$

where μ_m is the viscosity of a bubble and crystal free liquid where viscosity is controlled by the temperature and water content (Hess & Dingwell, 1996), $\theta_1(\beta)$ is a factor that increases viscosity according to crystal volume fraction (Costa, 2005) and $\theta_2(\alpha)$ is a factor accounting for the effect of the exsolved gas phase on viscosity (Llewellin et al., 2002; Llewellin & Manga, 2005). Lateral degassing through the conduit walls is defined to occur when bubble connectivity is sufficient at 60% volume fraction (Eichelberger et al., 1986) and conduit overpressure is greater than lithostatic pressure. The rate of lateral degassing (Q_{lat}) is described as in Jaupart & Allègre (1991) where

$$Q_{lat} = \frac{\rho_2\alpha_2 k_{wr}\left(p_2 - p_{lith}\right)}{\mu_2 R} \tag{3.10}$$

and k_{wr} is the wall rock permeability, and P_{lith} is the lithostatic pressure. I use a permeability of 4.8 x 10^{-14} m^2 after Jaupart & Allegre (1991) and Clarke et al. (2007).

The system of equations is solved using numerical approaches that progressively solve the equations from the bottom to the top of the conduit, starting from assumed initial conditions. A solution is achieved when the ascent rate satisfies pressure boundary conditions at the chamber and vent (conduit inlet and outlet).

I apply the model to the Merapi system using input parameter values taken from published literature (Table 3.1). I use a conduit length of 2000 m based on Ratdomopurbo & Poupinet (2000) who observed an aseismic zone 1500-2500 m below the vent, which they attribute to a small magma storage zone. Preece et al. (2013) also identified a shallow temporary storage zone at ~2 km depth based on petrologic samples from the 2006 eruption. Siswowidjoyo et al. (2005) estimate a vent radius of 25 m based on topographic maps, however, I use a conduit radius of 15 m as in previous conduit models for similar systems (Melnik & Sparks, 1999; Kozono & Koyaguchi, 2012; de' Michieli Vitturi et al., 2013). Magma temperature is 950 °C from Costa et al. (2013) and Voight & Davis (2000). Chamber pressure is lithostatic pressure calculated from the depth of the conduit inlet and assuming a carbonate bedrock composition (Table 3.1) (Troll et al., 2012) plus any overpressure I apply to the system. Outlet pressure at the vent is atmospheric plus the pressure applied by a dome of varying height (Global Volcanism Program, 2007; Ratdomopurbo et al., 2013) with a density of 2400 kg m^{-3} (Charbonnier & Gertisser, 2008). I use a dense rock equivalent (DRE) density of 2800 kg m^{-3} (Costa et al., 2013) and initial crystal volume fraction of 0.5 (Hammer et al., 2000). The dome height at the initiation of the 2006 eruption is estimated to be 150 m based on

observations of the crater floor elevation by Siswowidjoyo et al. (1995) and descriptions of eruptive activity from Walter et al., 2007), the Global Volcanism Program (2007), and Ratdomopurbo et al. (2013).

To match the observed extrusion rates at Merapi during the 2006 eruption (Ratdomopurbo et al., 2013; Chapter 2, this dissertation) I hold all parameters constant and vary the dome height, chamber overpressure, and volatile wt. % to simulate each phase of the eruption. Other input parameters in the model are unlikely to have changed significantly over the course of the two-month eruption whereas significant dome growth was observed (Ratdomopurbo et al., 2013) and increases in volatile content (Troll et al., 2012) and dynamic stress-induced increases in chamber overpressure (Walter et al., 2007; Harris & Ripepe, 2007) are both suggested as causes for the increased extrusion rate during the peak phase of the eruption.

I run the model for a wide range of parameter values and include all combinations of all parameter values using the Dakota toolbox (Adams et al., 2011). Dakota is open-source software developed at Sandia National Laboratories providing a flexible and extensible interface between analysis codes (in my case the model described above) and iterative systems analysis methods (e.g. uncertainty quantification, sensitivity analysis, optimization, and parameter estimation). For the Merapi system in 2006, the combination of multiple possible values for multiple parameters likely to be variable during the eruption results in over 350 model runs. Using the model solutions for these variable parameters, I am able to comment on the required magnitude of changes to dome height, volatile content, and overpressure that can account for the observed extrusion rates. I also address the feasibility of these values based on the physical processes responsible.

3.3. Results

A sequential list of the model runs that best describe activity for each eruption phase is shown in Table 3.2. I initiate model runs for Phases 1 and 2 of the 2006 eruption with no overpressure and a dome height of 150 m, representing the initial case with low mass flow rate and lava extruding from the conduit outlet into a complex of older domes from previous eruptions. Under these conditions, a volatile wt. % of 2.5 results in a DRE volume flow rate (extrusion rate) of 1.4 m^3 s^{-1}, within the range of extrusion rates for Phases 1 and 2 of 1.0-1.9 m^3 s^{-1} reported by Ratdomopurobo et al. (2013). A vertical profile of the conduit conditions during ascent for this run shows that ascent was under equilibrium conditions (Figure 3.3). For the low initial volatile wt. % used, lateral degassing does not initiate until the upper few meters of the conduit, where it causes some separation in the bubble and melt phase velocities and a small decrease in mass flow rate as gas exits the system.

For the peak of the eruption in Phase 3, I identify three different scenarios for the elevated extrusion rates: 1) overpressure-induced only 2) increased volatiles only and 3) a combination of both effects. I simultaneously account for an observed increase of 100 m in the height of the lava dome by using a dome height of 250 m (Global Volcanism Program (2007)). During Phase 3 extrusion rates were observed to increase from ~1.0 m^3 s^{-1} to ~3.5 m^3 s^{-1} (Ratdomopurbo et al, 2013; Chapter 2, this dissertation). An increase in overpressure of 5 MPa is necessary to account for this change and results in an extrusion rate of 3.6 m^3 s^{-1} (Table 3.2). An extrusion rate of 3.4 m^3 s^{-1} results from an increase in volatile wt. % from 2.5 to 3.7 (Table 3.2). Allowing for both overpressure and volatile

wt. % to change give an extrusion rate of 3.5 m^3 s^{-1} for an overpressure of 3 MPa and 3 wt. % volatiles (Table 3.2).

When I remove the overpressure and excess volatiles from the model but keep the 250 m dome, the result is an extrusion rate of 1.2 m^3 s^{-1} (Table 3.2), similar to the range of 0.7 – 1.6 m^3 s^{-1} observed for phases 4 and 5 (Preece et al. 2013; Chapter 2, this dissertation). For Phase 5 I decrease the dome height by 50 m to match observations of dome collapse during this time (Global Volcanism Program, 2007; Ratdomopurbo et al., 2013), resulting in an extrusion rate of 1.3 m^3 s^{-1}. While not a large difference, this change shows that varying dome height does have an effect on the extrusion rate in this case and that dome collapse can result in increased extrusion rates that rebuild the dome and promote future collapse.

Changes in the chamber conditions will not immediately be observed as a change in extrusion rate at the vent due to the response time of the magmatic system to the change (de' Michieli Vitturi et al., 2010). I use the ascent time of the magma in the conduit for each phase as an estimate for the length of this response time (Table 3.2). For the overpressure-only, volatiles-only, and combination scenarios for Phase 3, the ascent times are 38.3 hours, 47.6 hours, and 37.6 hours, respectively. The dissipation of the increased overpressure and/or volatiles in Phase 4 has an ascent time of 120 hours. For the change in dome height between Phases 4 & 5, the ascent time under the new conditions is 106 hours.

3.4. Discussion

I successfully validate the numerical model for the Merapi system by fitting it to each phase of the eruption using published literature values. My model results compare well with previous estimates of extrusion and ascent rate during the 2006 effusive eruption of Merapi Volcano based on observational (Walter et al., 2007; Ratdomopurbo et al., 2013), thermal remote sensing (Harris & Ripepe, 2007), and petrologic data (Preece et al., 2013). My estimate of 2.5 wt. % volatile content is reasonable for a slow-rising magma that has undergone degassing prior to eruption (Costa et al., 2013).

I compare the ascent times with a time-series of time-averaged discharge rate derived from nighttime satellite thermal images (Chapter 2, this dissertation) that show individual peaks in extrusion rate during each phase (Figure 3.4) as opposed to the average extrusion rates for each phase that I have reported so far. The maximum observed extrusion rate from a single satellite image was 7.5 $m^3 s^{-1}$ on June 2, 2016 (Chapter 2, this dissertation), 6 days after the May 27 earthquake. The trend of increasing extrusion rate during Phase 2 did not significantly increase until May 30, 3 days after the earthquake (Figure 3.4). The ascent time for the conduit conditions during Phase 3 is 1.6 – 2 days, suggesting that the full effect of the earthquake on the magmatic system took 1 – 4 days to develop. The decrease from the average extrusion rate in Phase 3 to the average rate in Phase 4 took ~7 days. This is slightly longer than the 5-day ascent time of magma during Phase 4 (Table 3.2), but shows that the effect caused by the earthquake dissipated over a few days, causing the extrusion rate to slowly decrease for a week before returning to magnitudes similar to those in Phase 1 (Figure 3.4). This analysis also

shows that the effect of the earthquake on the magma chamber was sustained for a period of 2 – 7 days.

During Phase 5 local peaks in extrusion rate are observed following some time after local peaks in the number of PDCs occurring each day (Figure 3.4), related to larger dome collapses. For the three peaks in PDCs per day shown in Figure 3.4 (+) on June 14, June 20, and June 27, peaks in extrusion rate (*) occurred on June 16, June 22, and June 29- a delay of two days in each instance and less than half the ascent time of 4.4 days for magma during Phase 5. This timeframe suggests the model is not fully capturing processes in the upper conduit that cause more significant and more rapid variation in extrusion rate. Another contributing factor to the magnitude of variability in the extrusion rate is errors from the estimation of the rate from satellite images. This method assumes a constant radiating temperature of a relatively cool dome crust (Harris & Ripepe, 2007), and if a satellite image is acquired after a large dome collapse event that exposes the hotter interior of the dome, the extrusion rate will be overestimated. Conversely, if little dome growth or collapse has occurred prior to the satellite image, the crust can become more insulating and appear cooler than the assumed temperature (as described in Chapter 6 of this dissertation).

Overpressure induced as a result of dynamic stress changes caused by passing seismic waves is attributed to an increase in the volume fraction of the exsolved gas phase of the magma. While multiple mechanisms have been proposed to explain how dynamic stress can increase the volume of the bubbles in the magma, no single mechanism can easily account for an increase in overpressure of 5 MPa. Advective overpressure caused by shaking-induced bubble rise through a magma chamber can

produce overpressures of a few MPa in a few days (Linde & Sacks, 1994), but the assumptions for that model may not generally be valid for most magmatic systems (Manga & Brodsky, 2006). The rectified diffusion model of Brodsky et al. (1998) has been demonstrated to increase the volume of the exsolved gas phase, but with typical pressure changes on the order of kPa, not MPa. Small pressure variations on the order of magnitude of those related to dynamic stress can also induce increased vesiculation of new bubbles and if the magma is supersaturated with volatiles, the bubbles can grow rapidly and increase overpressure (Manga & Brodsky, 2006). To generate the overpressure that I show is needed to cause the increase in extrusion rate on the timescales observed, a combination of vesiculation, bubble growth, and bubble rise processes is likely.

An increase in volatile content caused by the release of trapped CO_2 and decarbonation of fresh surfaces that result from earthquake-induced cracking in the mid- to upper crust can also lead to increased extrusion rates (Deegan et al., 2010; Troll et al., 2012). The ascent of the liberated crust-derived CO_2 from various depths within the Merapi magmatic system can also explain the delay in the response of the extrusion rate to the earthquake and the sustained elevated extrusion rate during Phase 3. For the elevated extrusion rates in Phase 3 to be solely accounted for by an increase in wt. % of the volatile phase, the wt. % must increase by nearly 50% from 2.5 to 3.7. However, the model does not account for different volatile species, treating the gas phase as 100% water. Because CO_2 is less soluble than H_2O and also decreases the solubility of H_2O in the magma (Deegan et al., 2010; Costa et al., 2013), a smaller increase in CO_2 would be required to result in the same volume fraction of bubbles. Deegan et al. (2010) also show

in experiments that the decarbonation process can release enough CO_2 to overpressure a magma chamber on a timescale of hours to days, in agreement with the timescales for the delayed response of extrusion rates following the earthquake.

The increase in crust-derived CO_2 contribution to the total CO_2 output at Merapi following the 27 May 2006 earthquake described by Troll et al. (2012) strongly suggests that CO_2 released into the magma as a result of the earthquake played a role in the 2006 eruption. Similarly, the simultaneous increase of extrusion rate at both Merapi and Semeru Volcanoes documented by Harris & Ripepe (2007) demonstrates the role of dynamic stress in triggering increases in volcanic activity. Thus, I favor an explanation for the elevated extrusion rates in Phase 3 that incorporates both the addition of volatiles through decarbonation and dynamic stress-induced overpressure as a result of the earthquake ('Combination', Table 3.2). Combining the two processes serves to reduce the magnitude of their individual contribution to a higher extrusion rate, making these values more physically realistic. The addition of CO_2 also encourages the processes of vesiculation, advective overpressure, and rectified diffusion by increasing the volatile content of the magma, which will result in bubble growth that increases the exsolved gas phase of the magma and the overpressure. An increase from 2.5 to 3.0 wt. % volatiles requires a complimentary increase in overpressure of 3 MPa to result in an extrusion rate of 3.5 $m^3 s^{-1}$ (Table 3.2). Similarly, an overpressure of 1 MPa requires 3.5 wt. % volatiles to result in the same extrusion rate.

The effect of the May 27 earthquake on the 2006 eruption of Merapi Volcano demonstrates the multiple ways in which seismic activity may effect volcanic systems and trigger either increased activity or a new eruption. In addition to the delayed effects

related to magma chamber processes, the earthquake also had an immediate impact on Merapi by causing a series of dome collapses resulting in numerous PDCs (Figure 3.4). While not all earthquakes that are large enough to induce static and/or dynamic stress changes on a volcanic system cause increases in volcanic activity (Manga & Brodsky, 2006), their potential to do so should be accounted for and anticipated in volcano monitoring and hazard mitigation. The effects of earthquake activity on volcanoes, and why some earthquakes trigger changes in activity while other do not, remains poorly understood and an important focus of future work.

3.5. Conclusions

I validate a numerical model of magma ascent in a volcanic conduit and use it to explain variable extrusion rates observed during the 2006 effusive eruption of Merapi Volcano. The peak phase of the eruption followed a M_W 6.4 earthquake ~50 km away and I show that this earthquake likely caused release of CO_2 into the magma that increased the volatile content of the melt and contributed to increased vesiculation and bubble growth, generating an overpressure in the magma chamber. This elevated overpressure and volatile content caused extrusion rates to increase by a factor of 3. Using the numerical model I am able to show the time it took for these effects to develop and dissipate when compared to a time series of satellite-derived extrusion rates and a daily record of PDC events. I also show that large dome collapses that reduced the height of the dome prolonged the eruption as the collapses reduced the confining pressure at the vent and promoted higher extrusion rates that rebuilt the dome.

This study demonstrates how a numerical model can be combined with literature and observational data to quantify the processes responsible for changes in volcanic activity. While I apply the model to the specific case of Merapi, the input conditions are flexible and allow for application to a variety of different volcanic systems. The model can also be applied in a forward sense to estimate changes in eruptive activity that may result from increases in magma supply to the system or seismic activity, for example. This and future applications of the conduit model help to quantify and improve understanding of eruption processes and hazard management at silicic volcanoes.

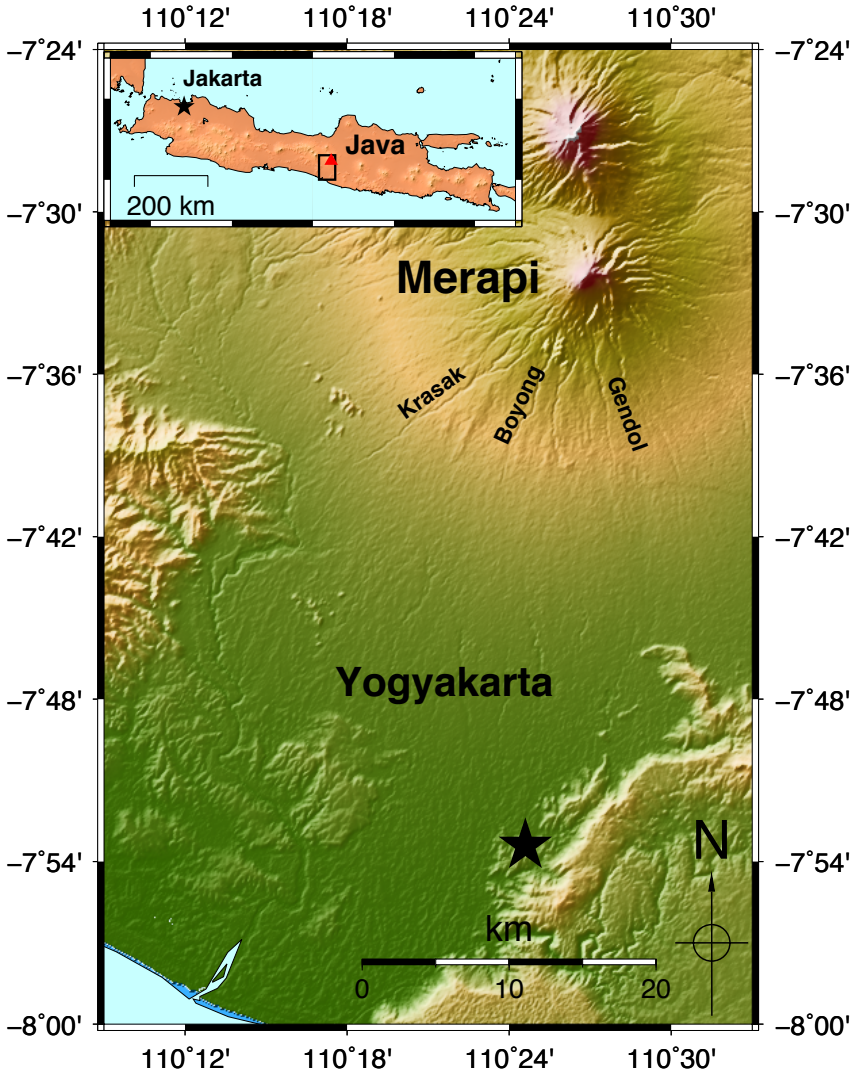

Figure 3.1. Location of Merapi Volcano. Merapi Volcano is located 30 km north of the city of Yogyakarta and 50 km north of the epicenter of the 2006 earthquake (star). Major PDC drainages for the 2006 eruption are labeled. Inset: location of the main figure (box) and Merapi (triangle) on the island of Java.

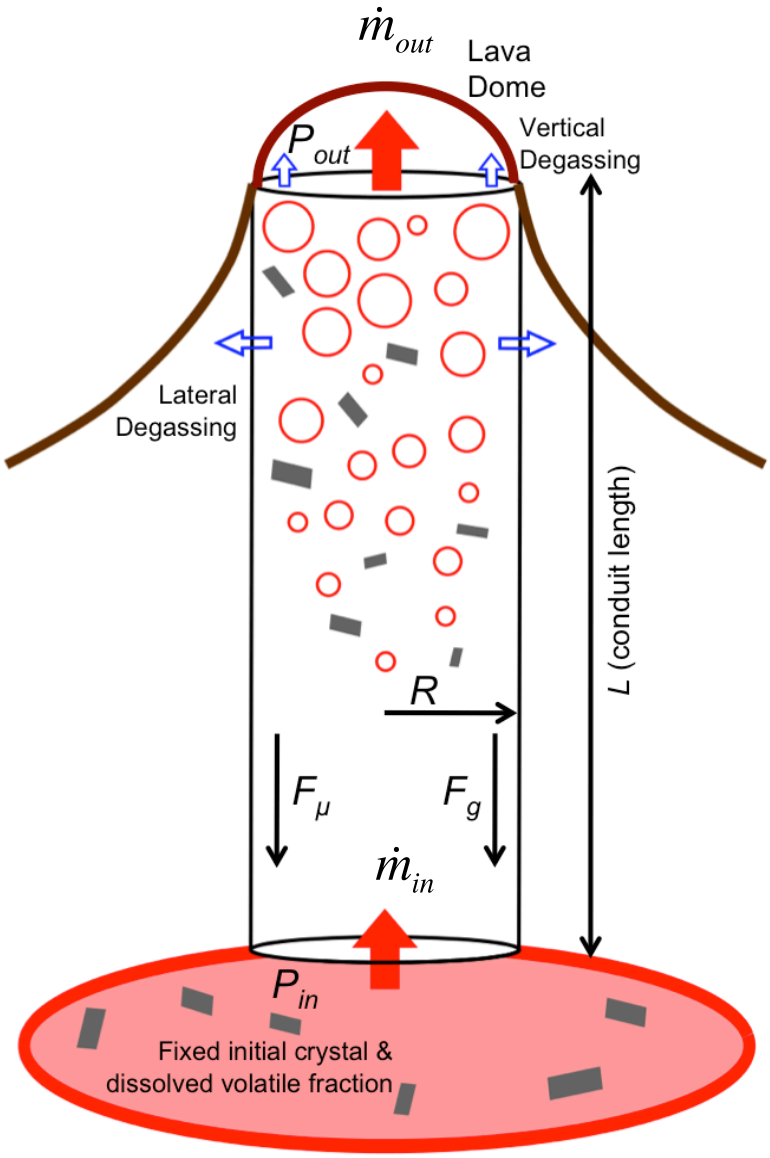

Figure 3.2. Schematic of the conduit model. Magma rise is driven by the pressure gradient between the chamber and the vent and resisted by viscous (F_μ, which includes resistance due to friction along the conduit walls) and gravitational (F_g) forces. As the magma rises it crystallizes (gray rhomboids) and gas exsolves (red circles). The magma degasses both laterally through the conduit walls and vertically through the vent. A lava dome creates confining pressure at the vent.

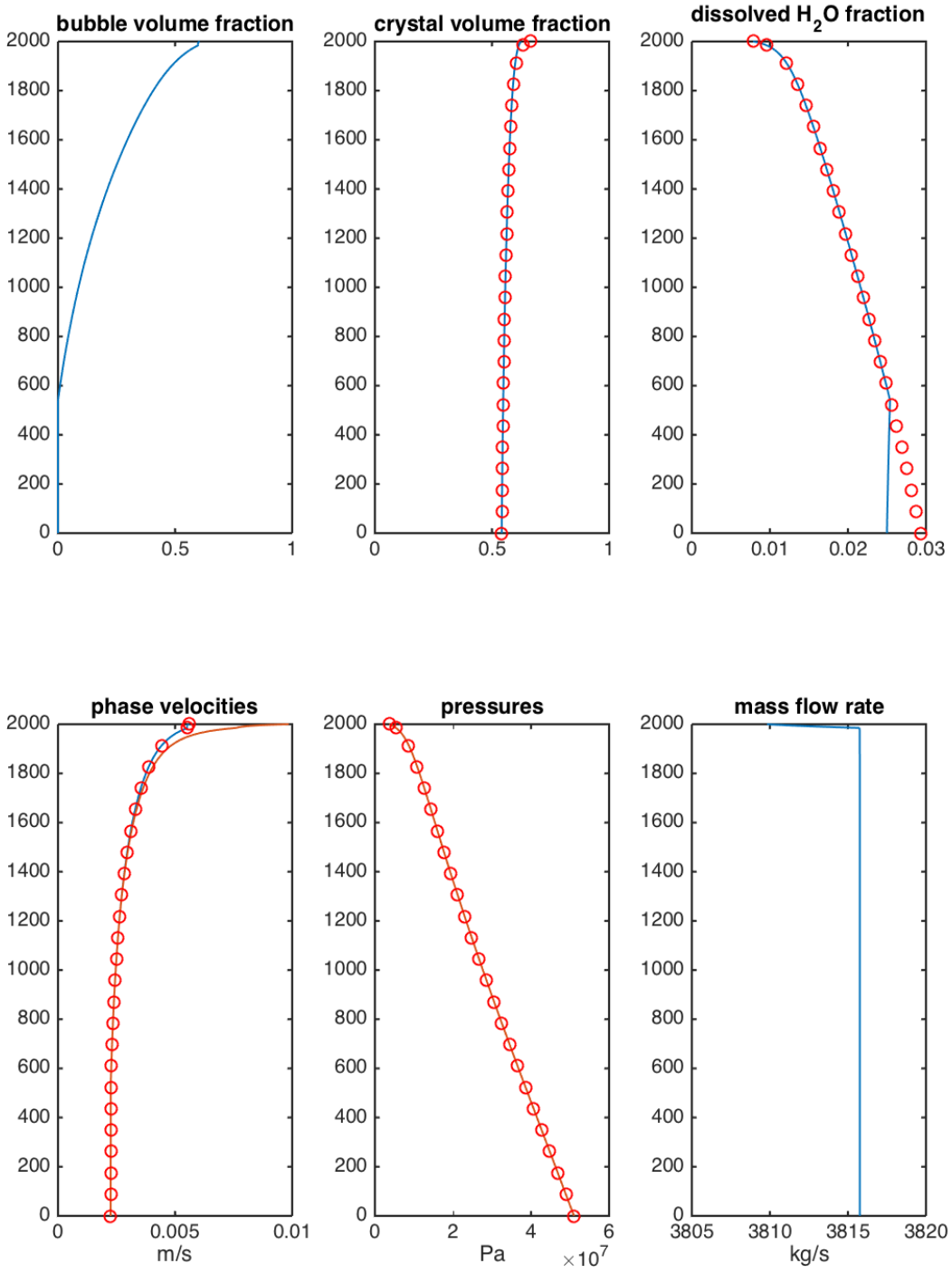
bubble volume fraction
crystal volume fraction
dissolved H_2O fraction
phase velocities
pressures
mass flow rate
m/s
Pa
$\times 10^7$
kg/s

Figure 3.3 (previous page). Model results for magma ascent. Each panel shows the ascent conditions for different parameters for my run representing activity during Phases 1-2. The y-axis is distance in meters along the conduit from the magma chamber to the vent. Solid blue lines are the values for the melt phase during ascent. The red line in the phase velocities panel is for the bubble phase. Open circles are equilibrium conditions for the pressure at that location in the conduit. The deviation of the blue line from the equilibrium values in the dissolved H_2O fraction panel occurs because the H_2O fraction set by the model input is less than the equilibrium value at the depth of the conduit inlet- no exsolution occurs during ascent until the equilibrium value is reached (note that the bubble volume fraction is 0 until this same depth, ~600 meters above the conduit inlet). Lateral degassing initiates very close to the vent when bubble volume fraction reaches 0.6 m, decreasing mass flow rate and separating the phase velocities by small amounts as gas exits the system.

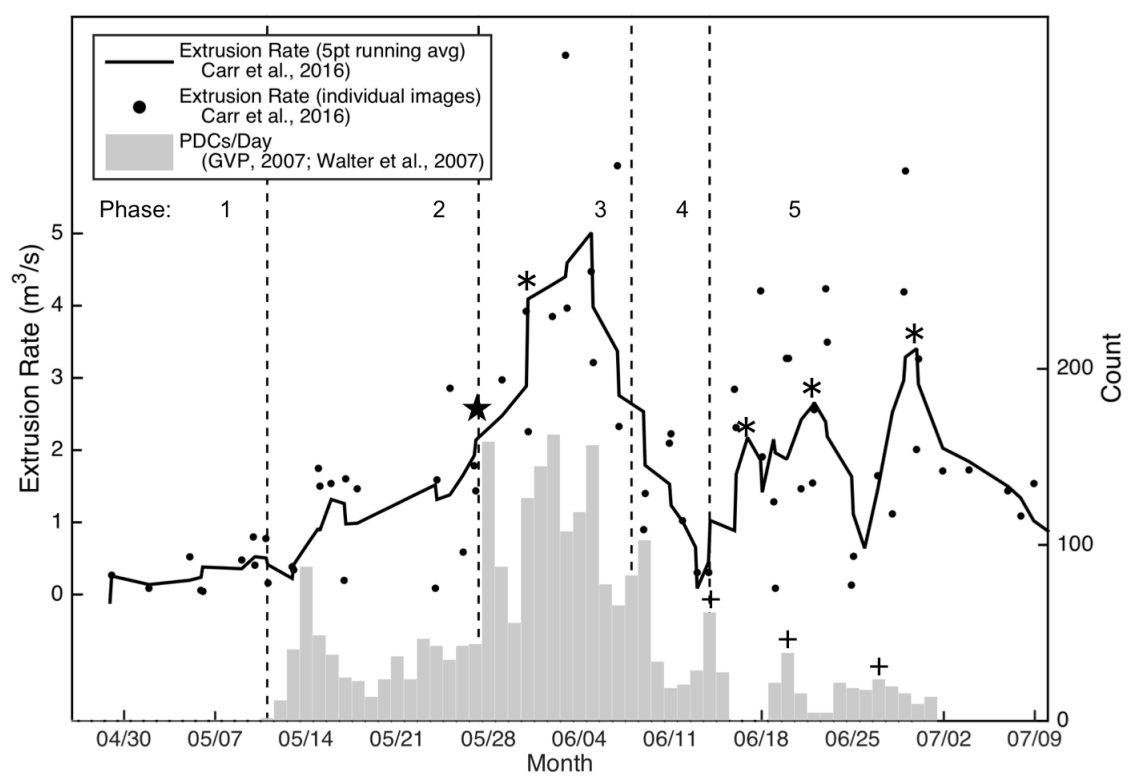

Figure 3.4. Extrusion rate during the 2006 eruption. A time series of extrusion rate derived from satellite thermal images (Chapter 2, this dissertation) (dots are individual images, solid line is a 5 point running average) shows the variable rate during the 2006 eruption. Phase boundaries from Ratdomopurbo et al. (2013) and the Global Volcanism Program (2007) are shown as dashed vertical lines and PDC counts per day from Walter et al. (2007) and the Global Volcanism Program (2007) are the vertical bars. Local peaks in PDCs related to the May 27 earthquake (★) or other dome collapse events (+) are followed by peaks in extrusion rate a few days later (*) due to the response time of the magmatic system to changes in pressure.

Variable	Units	Literature Value	Model Input
Conduit Length	Meters	1500 – 2500[1]	2000
Conduit Radius	Meters	25[2]	15[3]
Dome Height	Meters	0 – 250[4]	150
Chamber Pressure	MPa	51[5]	51
Temperature	Kelvin	1173 – 1273[6]	1223
Magma DRE Density	Kg m^{-3}	2800[6]	2800
Country Rock Density	Kg m^{-3}	2600[7]	2600
Crystal Fraction	Volume %	30-50[8]	50

1 Ratdomopurbo & Poupinet, 2000, Preece et al., 2013
2 Siswowidjoyo et al., 1995
3 Melnik & Sparks, 1999, de' Michieli Vitturi et al., 2013
4 Ratdomopurbo et al., 2013, Global Volcanism Program, 2007
5 Lithostatic at 2000 m depth with a density = 2600 kg m^{-3}
6 Costa et al., 2013
7 Density of carbonate rocks
8 Hammer et al., 2000

Table 3.1. List of input parameters. Model input parameters for Phases 1 & 2 (right column) are based on values from previous studies.

Phase	Date	Dome Height (m)	H_2O wt. %	Overpressure (MPa)	Ascent Time (hours)	Model Extrusion Rate (m^3/s)	Observed Extrusion Rate (m^3/s)
1 & 2	April 26 – May 26	150	2.5	0	99.3	1.4	0.7 – 1.9[4,5]
3[1]		250	2.5	5	38.3	3.6	
3[2]	May 27 – June 8	250	3.7	0	47.6	3.4	3.3 – 3.6[5,4]
3[3]		250	3.0	3	37.6	3.5	
4	June 9 – June 13	250	2.5	0	119.8	1.2	0.7[4]
5	June 14 – July 10	200	2.5	0	106.5	1.3	1.2 – 1.6[4,6]

1 Overpressure only
2 CO_2 only
3 Combination
4 Chaper 2, this dissertation
5 Ratdomopurbo et al., 2013
6 Preece et al., 2013

Table 3.2. Input parameters for each phase. Variables that I change to match observed extrusion rates for each phase of the 2006 eruption are shown in the middle columns, with the extrusion rate from the model output and the observed extrusion rates in the right most columns.

CHAPTER 4

VOLCANIC CONDUIT CONTROLS ON EFFUSIVE-EXPLOSIVE TRANSITIONS WITH APPLICATION TO THE 2010 ERUPTION OF MERAPI VOLCANO (INDONESIA)

Individual volcanoes can produce both effusive and explosive eruptions. A transition between these two eruption styles dramatically changes the eruption hazards and can occur either between distinct eruption events or within one eruption sequence. The causes of these transitions are difficult to determine due to the number of parameters related to the volcanic system that can influence whether or not magma fragments. I apply a numerical model of magma ascent in a volcanic conduit to isolate and test the effects of key parameters related to magma rheology and system geometry. For a given volcanic system, parameters related to magma viscosity, such as initial water mass fraction, crystal volume fraction, and temperature, have the greatest influence on whether or not magma fragments during ascent and erupts explosively. I also show that a transition in eruption style, from effusive to explosive or the reverse, can occur with minimal or no change in the rheology of the magma if the above parameters are in a 'critical' state, which I define as values near conditions necessary to cause fragmentation. In these cases, small heterogeneities in the water or crystal content of the magma, or variations in the conduit pressure gradient due to overpressure or dome growth/collapse, can push the magmatic conditions across the fragmentation threshold and cause a transition in activity style. The 2010 VEI 4 eruption of Merapi Volcano was exceptionally large compared to previous eruptions and included both effusive and

explosive phases. I constrain the model to the Merapi system using published literature values and show that between the previous eruption in 2006 and 2010, the Merapi system reached a critical state due to the ascent of a more gas-rich magma. Under these critical conditions, small changes in the volatile content of the magma then triggered transitions between effusive and explosive activity. I attribute these changes in volatile content to heterogeneous addition of CO_2 to the magma through decarbonation of the bedrock.

4.1. Introduction

Volcanic eruptions, whether effusive or explosive, have large impacts on their surroundings. While explosive eruptions are more violent and their hazards more far-reaching, effusive eruptions can persist for decades (Wolpert et al., 2016) and pose a continuous hazard. Transitions between eruptive styles are especially hazardous, as deviations from a "typical" eruption at a volcano can catch the local population unprepared for a larger or longer-lasting event. Numerical modeling is a useful technique to test the conditions leading to eruptions of varying size. Constraining a model to simulate the conditions of an active or potentially active system can help understand the potential for transitions in eruptive style in that system. In this chapter, I apply a numerical model of magma ascent in a volcanic conduit to show the effect of different magma and geometric properties on eruption style and then apply the model to explain the variations in explosive and effusive activity during the 2010 eruption of Merapi Volcano.

4.1.1. Transitions between explosive and effusive activity

An explosive eruption is initiated by fragmentation of the magma, which occurs when the volume fraction of the gas phase is large enough, or the strain rate in the rapidly ascending magma high enough, to induce brittle failure of the remaining melt phase of the mixture (Woods & Koyaguchi, 1994; Papale, 1999). This condition leads the carrying phase of the magma to switch from the melt phase containing bubbles to a gas-driven phase containing particles of melt and crystals. Previous works have discussed whether a volcano erupts effusively or explosively (i.e. whether or not the magma fragments) in the context of pressure building in the system and whether or not the volcano can dissipate this pressure through degassing (Woods & Koyaguchi, 1994; Ruprecht & Bachmann, 2010; Kozono & Koyaguchi, 2012). For this case, as overpressure in the system drives an increase in mass flow rate, proportionally less gas is able to escape the system and the magma density decreases, causing it to rise faster and become unable to depressurize before reaching the surface, causing an explosive eruption (Woods & Koyaguchi, 1994). Woods & Koyaguchi (1994) suggest that overpressure can be generated if supply rate from depth to the system is greater than the mass flow rate at the vent, and transitions between effusive and explosive eruptions occur to relieve this overpressure.

Transitions can also be affected by near-surface processes. Lateral degassing through the conduit walls promotes effusive eruptions by removing gas from the magma and preventing the critical bubble volume fraction from being reached (Jaupart & Allègre, 1991). Variations in the permeability of the conduit wall rock, which controls the rate of lateral degassing, can thus lead to different types of eruptions (Woods &

Koyaguchi, 1994; Diller et al. 2006; Clarke et al. 2007; Kozono & Koyaguchi, 2012; Degruyter et al., 2012). Lava domes can also have significant impact (Woods & Koyaguchi, 1994). Dome growth can suppress fragmentation by increasing the pressure at the vent, which reduces the pressure gradient in the conduit that is the driving force of the ascent rate. Conversely, dome collapse can relieve confining pressure and trigger explosive eruptions (Woods & Koyaguchi, 1994; Melnik & Sparks, 1999). Magma viscosity also strongly affects the potential for magma fragmentation, as Kozono & Koyaguchi (2012) describe a feedback mechanism whereby higher flow rates result in less crystallization during ascent and thus lower viscosities, which promotes further increase in flow rate. However, Ruprecht & Bachmann (2010) show that pre-eruptive heating of a silicic magma chamber by mixing with a recharge batch of magma can promote effusive eruptions by lowering viscosity and allowing more efficient gas loss in a permeable system.

Many of the factors described here show nonlinear effects on the mass flow rate at the vent (Melnik & Sparks, 1999, Kozono & Koyaguchi, 2012; Degruyter et al., 2012), where small changes in certain variables can result in large changes in the mass flow rate and potentially effusive-explosive transitions. Melnik & Sparks (1999) model how small changes in dome height can significantly vary the mass flow rate and show that the effects can be similar for minor variations in overpressure or volatile content as well.

4.1.2. Recent Merapi activity

Merapi Volcano is located in central Java (Figure 4.1) and for millennia has been one of Indonesia's deadliest and most active volcanoes (Newhall et al., 2000; Voight et

al., 2000). During the 20th and early 21st centuries Merapi was consistently active, with a sustained effusive eruption constructing a series of lava domes at the vent (Voight et al., 2000). Effusive activity was characterized by long periods of very slow (< 0.1 m^3 s^{-1}) extrusion rate interrupted every few years by short episodes of elevated extrusion rates (1 – 4 m^3 s^{-1}) lasting weeks to months (Siswowidjoyo et al, 1995). The periods of elevated extrusion rate were accompanied by dome collapse-generated block-and-ash flows, which caused a majority of the casualties and damage associated with the eruptions. This pattern of activity was so persistent for over 100 years that it became known as "Merapi-type" activity and this term is applied to describe similar eruptions at other volcanoes (Voight et al., 2000). The most recent "Merapi-type" eruption at Merapi occurred in May-July 2006 (Ratdomopurbo et al., 2013).

The 2010 eruption at Merapi broke the recent pattern in dramatic fashion. On October 26, following a period of intense precursory signals, an explosive eruption destroyed the 2006 lava dome and generated an ash plume 12 km tall (Surono et al., 2012). Following this explosion, rapid lava extrusion in excess of 25 m^3 s^{-1} built a new lava dome (Pallister et al., 2013a). After this period of rapid lava extrusion, the climactic explosion occurred on Nov 4-5 and rated as a VEI 4 (Volcano Explosivity Index; Newhall & Self, 1982) with an eruption plume reaching 17 km (Pallister et al., 2013a). Based on plume heights, mass flow rates during the explosive phases of the eruption were on the order of 10^6 – 10^7 kg s^{-1}(Sparks et al., 1986; Woods, 1988). During the waning phase of the eruption a new dome was emplaced at a rate of 35 m^3 s^{-1} (Pallister et al., 2013a). Extrusion rates during the 2010 eruption were over an order of magnitude greater than extrusion rates during the 2006 and previous 20th century effusive eruptions

(Ratdomopurbo et al., 2013; Hammer et al., 2000). Column-collapse pyroclastic density currents (PDCs) reached up to 16 km from the vent during the November 4-5 explosion, compared to 7 km for the largest dome-collapse PDCs from the 2006 eruption (Charbonnier & Gertisser, 2008; Charbonnier et al., 2013). As a result of the significant increase in eruption intensity in 2010, 367 people were killed- the deadliest eruption at Merapi since 1931 (Voight et al., 2000; Surono et al., 2012). The previous VEI 4 eruption at Merapi occurred in 1872, and eruptions of this size were more common in the two millennia prior to that year compared to the past 150 years (Voight et al., 2000; Newhall et al., 2000; Gertisser et al., 2012).

Surono et al. (2012) and Costa et al. (2013) suggest the exceptional size of the 2010 eruption was caused by the rapid ascent of an unusually large and volatile-rich batch of magma from depth. This magma had similar composition to the 2006 magma (Costa et al., 2013), but the size and ascent rate overwhelmed the capacity of the shallow, crystal-rich storage system at Merapi that had slowed previous rising magma batches, allowing them to degas and erupt effusively (Costa et al., 2013). Surono et al. (2012) attribute the explosiveness of the 2010 eruption to the separation of the gas phase from the rest of the magma that allowed it to rise rapidly to the surface and attribute the alternation between effusive and explosive eruption phases to variable gas content in the magma.

4.2. Methods

I use a numerical model for magma ascent in a vertical conduit derived from the theory of thermodynamically compatible systems (Romenski et al., 2010; La Spina et al.,

2014). For my application, this model applies to 1D, isothermal, two-phase flow in a steady state (Chapter 2, this thesis). The model accounts for the effects of the main processes controlling magma rise in a vertical conduit, such as crystallization, rheological changes, magma fragmentation, interaction with the conduit walls (viscous forces), outgassing, and degassing. The model treats the evolving viscosity of the melt as a function of the viscosity of a bubble- and crystal-free melt adjusted for factors accounting for the effects of temperature and dissolved water content (Hess & Dingwell, 1996), volume fraction of crystals (Costa, 2005), and exsolved gas phase characteristics (Llewellin et al., 2002; Llewellin & Manga, 2005). Lateral degassing occurs when bubble connectivity is sufficient to allow permeable gas loss (~60% volume fraction, Eichelberger et al., 1986) and the conduit overpressure is greater than the lithostatic pressure. I use the rate of lateral degassing as defined by Jaupart & Allègre (1991) and a value for wall rock permeability of 4.8×10^{-14} m^2 as in Diller et al. (2006) and Clarke et al. (2007). The conservation equations used in the model, including the conservation of the mass, momentum, and energy for the mixture, plus volume fractions and mechanical disequilibrium, can be found in Chapter 2 of this dissertation.

I use a critical gas volume fraction to define the fragmentation threshold. At this critical value the bubble volume fraction is too large for the melt phase to remain connected and magma fragmentation occurs. Following previous works (Woods & Koyaguchi, 1994; Kozono & Koyaguchi, 2012; Degruyter et al., 2012), I use a value of 0.8, above which the magma will fragment. Below the fragmentation level, the liquid phase (a mixture of crystals, dissolved gas, and melts) is defined as the continuous phase while the exsolved gas is the dispersed phase. Above the fragmentation level, the

exsolved gas constitutes the continuous phase while magma fragments constitute the dispersed phase. The characteristic time which controls the degree of decoupling between the gas and liquid phase is defined to retrieve the Forchheimer's law to model the outgassing when the mixture is below the fragmentation level. Above the fragmentation level this characteristic time is defined in order to model the drag exerted by the gas on the fragmented particles of magma (Degruyter et al., 2012; La Spina et al., 2015). The system of equations is solved using numerical approaches that progressively solve the equations from the bottom to the top of the conduit, starting from assumed initial conditions. A solution is achieved when the ascent rate satisfies pressure boundary conditions at the chamber and vent (conduit inlet and outlet).

To investigate the effects of different parameters on mass flow rate and magma fragmentation and estimate the parameters that lead to the observed activity at Merapi in 2010, I use the Dakota toolbox (Adams et al., 2011). Dakota is open-source software developed at Sandia National Laboratories providing a flexible and extensible interface between analysis codes (in my case the model described above) and iterative systems analysis methods (e.g. uncertainty quantification, sensitivity analysis, optimization, and parameter estimation). For my variable sensitivity analysis I conduct two types of runs. First, I hold all but one parameter constant to isolate individual effects. Second, I use sets of three free parameters and run the model for all combinations of all variable values to investigate the relationship between parameters in a dynamic system. Dakota allows these sets of model runs to be run iteratively without manual manipulation of input values, dramatically streamlining this process. In total, the output of over 1500 model runs are

included in the variable sensitivity and Merapi parameter estimation results presented below.

I choose a set of model input values representative of previous research on different volcanic systems to define a 'standard' run to use during my variable sensitivity analysis (Standard Run, Table 4.1). I use a conduit length of 5000 m, conduit radius of 15 m, and temperature of 850 °C from Melnik & Sparks (1999), Kozono & Koyaguchi (2012), and de' Michieli Vitturi et al. (2013). The pressure at the conduit inlet (magma chamber) is 130 MPa, which assumes lithostatic pressure with a country rock density of 2650 kg m^{-3}. The pressure at the conduit outlet (vent) is ~3.6 MPa, based on a 150 m tall dome (Calder et al., 2002; Nakada et al., 1999; Ratdomopurbo et al., 2013) with a density of 2400 kg m^{-3} (Komorowski et al., 2013). Initial water mass fraction is 0.04 (Degruyter et al., 2012; Costa et al., 2013) and initial crystal volume fraction is 0.44 (Melnik & Sparks, 1999; Hammer et al., 2000; Degruyter et al., 2012). For Merapi ('Merapi Literature', Table 4.1), I change the conduit length to 2000 m (Ratdomopurbo & Poupinet, 2000), country rock density to 2600 kg m^{-3} (for a carbonate bedrock), and lateral permeability to 4.8 x 10^{-12} m^2 (within the range given by Jaupart & Allègre, 1991). I then vary the water mass fraction from 0.04 – 0.06 (Costa et al., 2013), the crystal volume fraction from 0.3 – 0.5 (Hammer et al., 2000), the temperature from 950 °C – 1000 °C (Costa et al., 2013), and the dome height from 0 – 130 m (Pallister et al., 2013a). I select the runs that best describe the observed activity at Merapi (Runs 1-6, Table 4.1) from this set of parameters and use these results to assess the processes responsible for the documented 2010 eruptive activity.

4.3. Results

The model output demonstrates the conditions of magma ascent for the standard run I describe above (Figure 4.2). The most noticeable condition during ascent is the effect of lateral open-system degassing, which initiates when the bubble fraction equals 0.6 near the top of the conduit (dashed line, Figure 4.2a) and causes a decrease in mass flow rate, in the velocity of both phases, and in bubble volume fraction above the initiation point. Decreasing the initial crystal content by a factor of two (from 0.44 to 0.22) results in an explosive eruption (Figure 4.2b) with fragmentation occurring ~1000 m below the vent (dashed line, Figure 4.2b). The bubble volume fraction increases exponentially such that for the lower crystallinity case, the rate of lateral degassing is too low to suppress fragmentation, resulting in an explosive eruption (Figure 4.2b).

I vary eight parameters from my standard run to show the effects of each parameter on the mass flow rate (Figure 4.3). In three cases (crystal volume fraction, temperature, and dome height), the range of values (above and in Table 4.1) includes a transition between explosive and effusive activity (stars, Figure 4.3). The parameters controlling magma viscosity - crystal volume fraction, temperature, and water mass fraction - have the largest effect on fragmentation. Though for the standard run, the crystal volume fraction and temperature dominate the viscous effects such that increasing water mass fraction cannot induce fragmentation (Figure 4.3, 1st panel). This effect is due to the chosen values for crystal volume fraction and temperature strongly favoring higher viscosities and effusive eruptions. Similarly, when water mass fraction is fixed at a low value (0.02) and the others are varied, it dominates the viscous effects compared to crystal volume fraction and prevents fragmentation (compare slope of blue line to that of

the red line, Figure 4.3 2nd panel). Parameters related to system geometry or pressure- conduit radius, conduit length, overpressure, and dome height- have variable effect on mass flow rate and do not have a major effect on fragmentation for the ranges shown. Dome height has a critical value for a given set of input parameters- below this height fragmentation will occur and above this height effusion will occur- while increasing dome height above the critical value has a relatively small effect on mass flow rate. For the set of input parameters I chose for the standard run, wall rock permeability also has a small effect on mass flow rate (Figure 4.3, 4th panel).

I also look at the relationships between multiple varying parameters and their relative effect on mass flow rate and fragmentation. For these sets of runs I focus on water mass fraction and crystal volume fraction over ranges of 0.03 – 0.05 and 0.3 – 0.5, respectively, and three different 'third' parameters- temperature (850 and 950 °C), dome height (0, 75, and 150 m), and overpressure (0, 5, and 10 MPa). Water mass fraction, crystal volume fraction, and temperature all control the viscosity of the melt, so the combined effect of all three parameters, as they move toward values that decrease viscosity, is an exponential increase in mass flow rate (Figure 4.4a). The top surface in Figure 4.4a represents a fixed temperature of 950 °C, while the bottom surface represents a fixed temperature of 850 °C; effusive runs are marked with blue dots. In contrast, Figure 4.4b shows a linear rate of increase in mass flow rate as both the water and crystal content change. The three different surfaces represent three different dome heights, with lowest dome height representing the upper surface. Figure 4.4b also shows the same pattern as in Figure 4.3, where the threshold dome height is the most important control on mass flow rate; varying dome height within a given regime, effusive or explosive, has a

small effect on mass flow rate, whereas a transition from one regime to the other has a dramatic effect on mass flow rate. For the runs in Figure 4.4, that critical transition occurs in the far lower right corner for the top (no dome) surface (crystal volume fraction 0.48-0.5 and water weight fraction 0.03-0.036) and moves towards the lower left corner (decreasing crystal volume fraction, increasing water weight fraction) as dome height increases (middle and bottom surfaces). For the range of chamber overpressures I used for these runs, there is little impact on mass flow rate compared to the water or crystal content (Figure 4.4c; note that all three surfaces are tightly spaced and are parallel).

The effusive-explosive regime diagrams in Figure 4.5 highlight the critical conditions where fragmentation is likely for these parameters. In each of these panels the effusive regime is located in the lower right and the explosive regime is in the upper left. The lines in each diagram are the fragmentation thresholds for the labeled value of the third parameter. The slope of this line shows which of the two axes parameters has a greater effect on fragmentation - a slope near zero shows that fragmentation is controlled by the water mass fraction while a near-vertical slope indicates that fragmentation is controlled by the crystal volume fraction. Intermediate slopes are controlled by both parameters to varying degrees. The space between fragmentation threshold lines represents the 'strength' of the third parameter in controlling fragmentation conditions, with greater spacing indicating greater effect. The region along the fragmentation threshold line represents a critical zone where small changes in parameter values can result in the boundary being crossed and a transition in eruption style.

For a magma temperature of 950 °C (Figure 4.5a), a change of either 0.02 crystal volume fraction (i.e. 0.46 to 0.44) or 0.002 water mass fraction (i.e 0.036 to 0.038) will

result in a transition between effusive and explosive regimes (arrows, Figure 4.5a). For a temperature of 850 °C, critical values shift, for example, to 0.30 – 0.34 for crystal volume fraction and 0.038 – 0.046 for water mass fraction, showing the significance of the effect of the temperature on fragmentation (Figure 4.5a). Also note that, for the range of water and crystal contents explored here, the explosive regime dominates at 950 °C, whereas the effusive regime dominates the 850 °C case. Most runs are explosive when no dome is present (Figure 4.5b), while the effusive regime dominates when dome height is 150 m. The larger space between the 0 m and 75 m dome height lines compared to the space between the 75 m and 150 m dome height lines is because the critical dome height for a majority of the runs shown (black dots) lies between 0 and 75 m rather than 75 and 150 m. Figure 4.5c again shows the relatively minor effect of overpressure on fragmentation compared to other parameters, although increasing overpressure gently moves the system toward explosive activity. Under the right conditions (0.34 crystal volume fraction and 0.044 water mass fraction, shown as a star in Figure 4.5c), an increase in overpressure of just a few MPa can cause fragmentation, but in other conditions (arrow, Figure 4.5c) a 10 MPa increase in overpressure will not cause fragmentation while a decrease in crystal volume fraction of just 4% (from 0.34 to 0.3) will cause fragmentation.

Using parameter values from previous studies on Merapi (Table 4.1), the conduit model is able to match the mass and volume flow rates observed during both explosive and effusive phases of the 2010 eruption (Runs 1-7, Table 4.1). Run 1 (Table 4.1) represents the October 26 explosive initiation of the eruption. For a water mass fraction of 0.04, crystal volume fraction of 0.44, and temperature of 970 °C, the magma fragments and erupts explosively with a mass flow rate of 1.4×10^6 kg s^{-1}, despite the initial

confining pressure of the 50 m dome remaining from the 2006 eruption (Ratdomopurbo et al., 2013). The exceptionally high effusion rates immediately following the 2010 explosive phase rapidly built a new lava dome at a documented volume flow rate of approximately 25 $m^3 s^{-1}$ (Pallister et al., 2013a). I model these conditions (Run 2, Table 4.1), achieving an effusion rate of 28 $m^3 s^{-1}$ using a dome height of 130 m and the same water content, crystal content, and temperature as Run 1. An explosive phase can be initiated under these effusive conditions by increasing the water mass fraction by just 0.001, from 0.040 to 0.041 (Run 3, Table 4.1). This comparison suggests that the Merapi system was in a critical state during the 2010 eruption, where very small changes in individual parameters could result in fragmentation and a transition from an effusive to explosive eruption, and back again. Similarly, a decrease in dome height of only 10 m, from 130 m to 120 m, also results in fragmentation (Run 4, Table 4.1) and dramatically greater mass flow rates of $1.6 – 1.9 \times 10^5$ kg s^{-1}. Either or both of these changes may have been the trigger for the November 4-5 climactic explosive phase of the eruption. After initiation of the explosive phase destroyed the lava dome (Runs 5 & 6, Table 4.1), maximum mass flow rate during this phase was $3.7 – 5.3 \times 10^6$ kg s^{-1} for the range of volatile contents measured in samples from the eruption by Costa et al. (2013). The model output mass flow rates of $1.4 – 5.3 \times 10^6$ kg s^{-1} for both explosive phases (Runs 1, 5, & 6, Table 4.1) are within the range of $10^6 – 10^7$ kg s^{-1} likely for an explosive eruption that produces plumes between 12 and 17 km in height (Sparks, 1986; Woods, 1988; Pallister et al., 2013a).

4.4. Discussion

The broad range of model results for multiple parameters that I present here allows me to comment on two types of effusive-explosive transitions at individual volcanoes- those that occur between distinct eruption events and those that occur within one eruption sequence. Furthermore, I am able to apply these concepts to describe processes at Merapi Volcano that led to effusive-explosive transitions between the 2006 and 2010 eruptions and during the 2010 eruption.

4.4.1. Transitions between distinct eruptions

Parameters affecting the viscosity of the magma have the greatest influence on mass flow rate and thus whether or not fragmentation occurs (Figure 4.3). A transition in eruption style can occur if the viscosity of the magma changes between eruptions. This can be achieved without changing the composition of the magma, but by altering the water mass fraction, crystal volume fraction, and/or temperature of the magma through mixing with new magma ascending into the system. The new magma will generally be hotter, higher in volatile content, and lower in crystal content compared to a magma residing in a shallow storage system (Ruprecht & Bachmann, 2010). If this newly mixed magma does not get stalled during ascent, its lower viscosity will favor explosive eruption compared to the pre-existing magma in the system. This process is likely responsible for the explosive eruption at Kelud Volcano (Java, Indonesia) in 2014, which followed an effusive eruption in 2007 (Kristiansen et al., 2015; Jeffery et al., 2013). Precursory seismic activity showed rapid ascent of magma from depth (Global

Volcanism Program, 2014c), suggesting a new magma batch quickly mixed with the residing magma and erupted prior to degassing or cooling.

Conversely, if magma entering or remaining in a shallow storage region following an explosive eruption has time to cool, degas, and/or crystallize prior to rising towards the vent, it will favor effusive eruption due to a higher viscosity. This is likely the case for dome-forming eruptions that follow in the months to years after large explosive eruptions, such as at Mount St. Helens in Washington (Fink et al., 1990) and Santiaguito Volcano in Guatemala (Anderson et al., 1995). The rate of magma ascent and the duration of magma storage is also an explanation for why neighboring volcanoes can display very different types of activity, despite their proximity.

4.4.2. Transitions during eruptions

For a transition between explosive and effusive activity to occur within a single eruption sequence, the volcanic system must be in a 'critical' state, where small variations of one or two parameters can cause the conduit conditions to cross the fragmentation threshold (Figure 4.5). This concept has been described previously for scenarios involving overpressure (Woods & Koyaguchi, 1994), permeable gas loss (Kozono & Koyaguchi, 2012; Degruyter et al., 2012), viscosity (Kozono & Koyaguchi, 2012), and dome height (Melnik & Sparks, 1999; Woods & Koyaguchi, 1994), and I observe trends in my results similar to these studies. In the critical zones along the fragmentation threshold lines (Figure 4.5), small variations in water mass fraction or crystal volume fraction can cause the eruption style to change. The variations are small enough to be attributed to natural heterogeneities in a magma chamber. Given constant

values for water mass fraction and crystal volume fraction, critical values also exist for temperature, dome height (Figure 4.3), and overpressure. Critical states likely explain the multiple phases of the eruption of Chaitén Volcano in Chile in 2008 – 2009 (Pallister et al., 2013b), although additional modeling work specifically targeting the Chaitén system is required to determine the critical parameter(s) responsible for the observed activity.

Singular explosive eruptions and sustained effusive eruptions are likely examples of systems where the magma is not near a critical state. Because small variations in parameters will not change the eruption type, the eruption style is stable and will continue until the supply of magma diminishes- rapidly over a few hours for explosive eruptions or slowly over months or years for effusive eruptions. The 2014 eruption of Kelud, which it did not produce any effusive activity before or after the February 14 explosion (Global Volcanism Program, 2014c), is likely an example of an explosive eruption from a stable state, while the ongoing eruption of Santiaguito is a likely example of an effusive eruption from a stable state.

4.4.3. Transitions at Merapi in 2010

My model results support previous observations of the 2010 Merapi eruption. The volume flow rate of 28.1 m^3 s^{-1} that I calculate in Run 2 (Table 2) is within the range of 25 – 35 m^3 s^{-1} observed by Pallister et al. (2013). The maximum mass flow rate of 5.3 x 10^6 kg s^{-1} (Run 6, Table 4.1) is within the range of 10^6 – 10^7 kg s^{-1} expected for an eruption generating a 17 km high plume (Sparks, 1986; Woods 1988). Compared to my results using the same conduit model to fit the 2006 eruption (Run 7, Table 4.1; Chapter 2, this dissertation), water mass fraction increases from 0.025 to 0.04, crystal volume

fraction decreases from 0.5 to 0.44, and temperature increases from 950 to 970 °C for the effusive phase of 2010 eruption (Run 2, Table 4.1). These changes can be explained by a hotter, less-crystallized, more volatile-rich magma entering and mixing with the existing magma in the Merapi system between the 2006 and 2010 eruptions. This mixing created conditions more favorable for explosive eruptions and high extrusion rates during effusive activity. This explanation for the cause of the more violent 2010 eruption agrees with the conclusions of Surono et al. (2010) and Costa et al. (2013), based on monitoring and petrologic observations respectively. Costa et al. (2013) explain that while the magma prior to the 2006 eruption had time to crystallize and degas in a shallow storage region, leading to an effusive eruption, the volume of magma entering the system in 2010 overwhelmed the shallow storage region, which limited the degassing and crystallization that could occur, and resulted in an explosive eruption. I attribute increased conduit wall rock permeability in 2010 compared to 2006 conditions (Runs 1 & 7, Table 4.1) to fracturing of the conduit walls during the initial explosive phase on 26 October.

I show that the rising batch of new magma generated a critical state in the Merapi system in 2010. Very small changes in either water mass fraction or dome height result in a transition from effusive to explosive eruption (Runs 2-4, Table 4.1). Variations of 0.001 water mass fraction can easily result from eruption from a heterogeneous magma chamber, as suggested by Surono et al., (2010). A variable volatile content may also result from the addition of CO_2 to the magma through decarbonation of the carbonate bedrock. Deegan et al. (2010) and Troll et al. (2012) show that activity at Merapi in 2006 was likely affected by this process, and Costa et al. (2013) suggest that decarbonation would likely be increased in 2010 due to the increased temperature and volume of the

magma. A dome collapse that reduced the average height of the dome by only 10 m would also be sufficient to trigger fragmentation (Run 4, Table 4.1). Given the frequency of block and ash flows during this and other Merapi eruptions, this is also a reasonable explanation for the initiation of explosive activity. However, I favor a variation in volatile content due to decarbonation as the primary trigger for effusive-explosive transitions during the 2010 eruption. Decarbonation is an identified process at Merapi (Deegan et al., 2010; Troll et al., 2012), whereas no descriptions of the eruption mention large dome collapses preceding the explosive phase in 2010, and in the case of the October 26 explosion, sources specifically note the lack of any dome instability or activity prior to this event (Surono et al., 2012; Pallister et al., 2013a). I also show that no substantial chamber overpressure is required for an explosive eruption to occur. This conclusion agrees with the work of Chaussard & Amelung (2012) who do not observe inflation at Merapi prior to the 2010 eruption.

The transition from explosive back to effusive activity likely still resulted from eruption rate exceeding supply rate from depth during the explosive phase as described by Woods & Koyaguchi (1994), but I suggest that this process was aided by an increase in outlet pressure at the vent due to a collapsing eruption column rather than the dissipation of an overpressure in the magma chamber (conduit inlet).

4.5. Conclusions

I use a numerical model of magma ascent in a volcanic conduit that accounts for magma fragmentation at a critical bubble volume fraction to investigate effusive-explosive eruption transitions in silicic volcanic systems. In general, the parameters

controlling the viscosity of the magma - water mass fraction, crystal volume fraction, and temperature - exert the greatest control on the mass flow rate and fragmentation. I also compare multiple parameters against each other and identify critical conditions for different sets of parameters under which a small change in a single parameter can result in the crossing of the fragmentation threshold and change in eruptive style. Critical conditions are especially sensitive to variations in water mass fraction or crystal volume fraction, but critical values also exist for all other parameters that I investigate in this study.

A transition in eruption style between eruption events can most easily be caused by changes in the viscosity of the magma in the system due to either rapid ascent of new magma (effusive → explosive) or prolonged shallow storage of magma (explosive → effusive). A transition in eruption style during a single eruption is caused by the critical state of the system where small changes in one or two parameters result in conditions that cross the fragmentation threshold. My results support the suggestion that the transition at Merapi Volcano from effusive eruption in 2006 to explosive eruption in 2010 was caused by the fast ascent of a volatile-rich batch of magma that was too large to be accommodated in the shallow storage system (Costa et al., 2013). This new batch of magma also pushed the Merapi system into a critical state, and small spatial variations in either water mass fraction or dome height led to transitions between effusive and explosive activity during the 2010 activity. I favor a variation in volatile content by the addition of CO_2 to the magma from decarbonation of bedrock - a process that has been previously identified at Merapi - as the primary cause of spatial variations in magma volatile content and thus the effusive-explosive transitions during the 2010 eruption. This

methodology is broadly applicable to multiple types of volcanic systems and can be used to investigate the causes of ongoing or historical eruptive behavior as well as anticipate the conditions that may lead to different types of eruptive activity in the future.

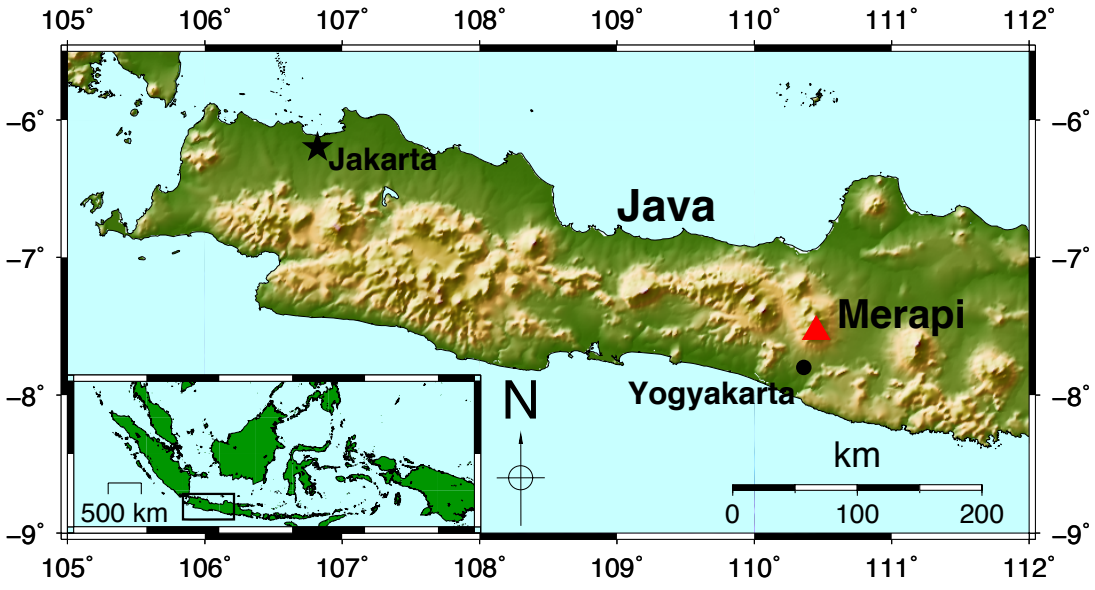

Figure 4.1. Location of Merapi Volcano. Merapi (triangle) is located in central Java, 30 km north of the city of Yogyakarta. **Inset:** Location of the main map (box) within the Indonesia archipelago.

Figure 4.2 (following pages). Model results for magma ascent. Each panel shows the ascent conditions for six different parameters for the standard run (a) and an explosive run where the crystal content was reduced by a factor of two (b). The y-axis is distance in meters along the conduit from the magma chamber to the vent. Solid blue lines are the values for the melt phase during ascent. The red line in the phase velocities panel is for the bubble phase. Open circles are equilibrium conditions for the pressure at that location in the conduit. Where the solid line deviates from the circles for the crystal volume fraction in (b), ascent is too rapid for the rate of crystallization to keep up with depressurization. Horizontal dashed lines show the level of lateral degassing initiation (a) and the fragmentation level (b).

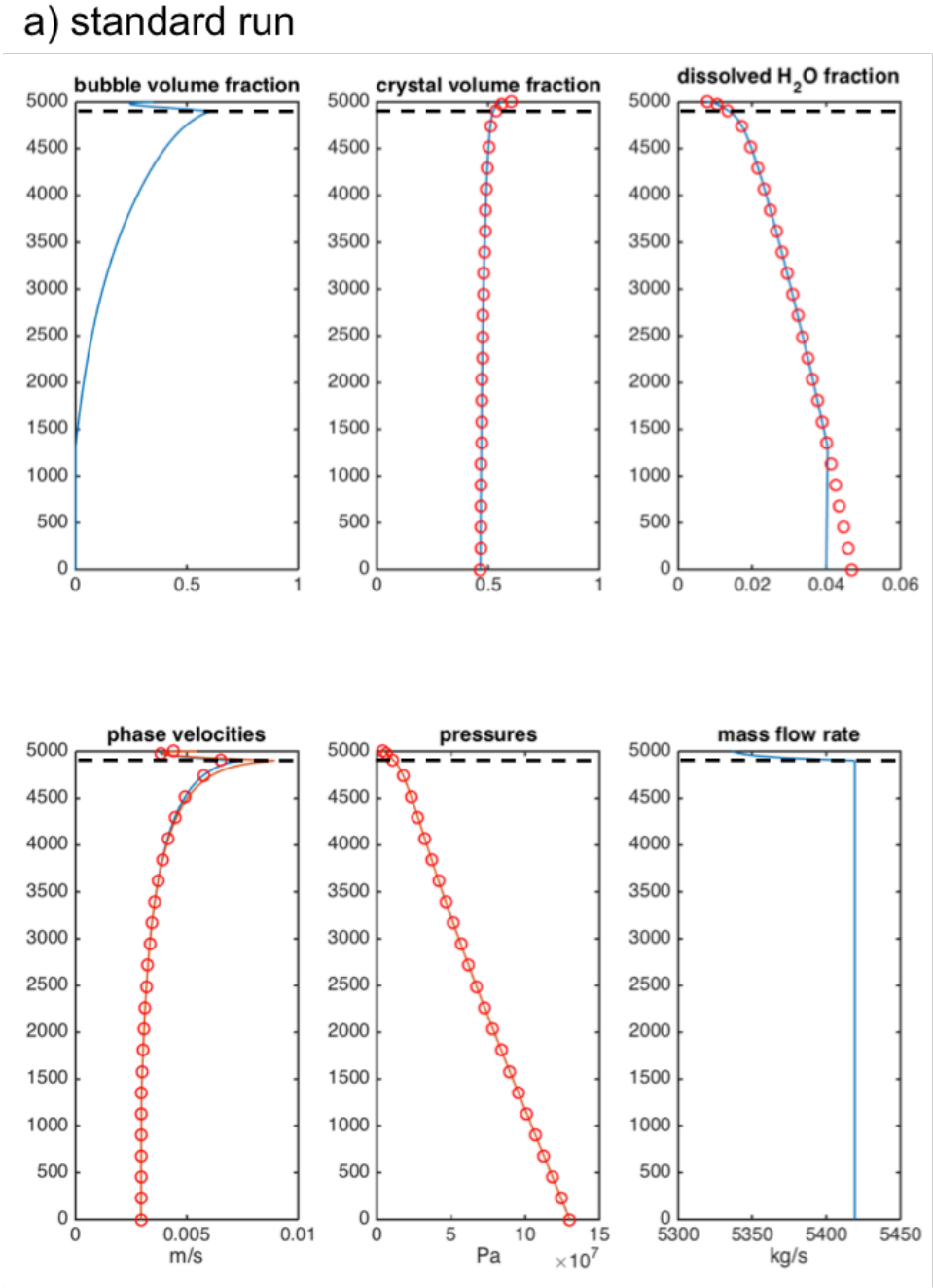

Figure 4.2 continued.

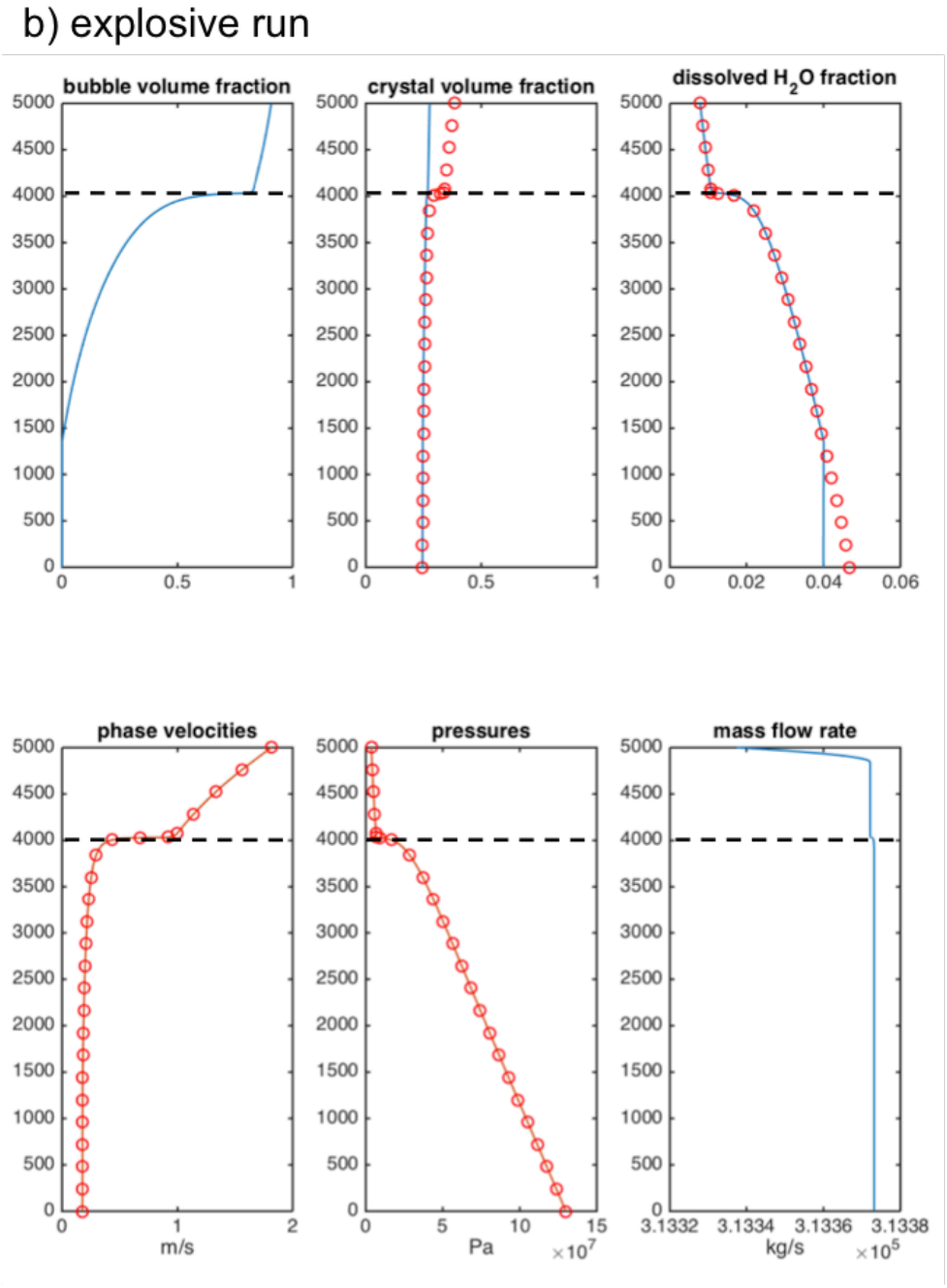

Figure 4.2 continued.

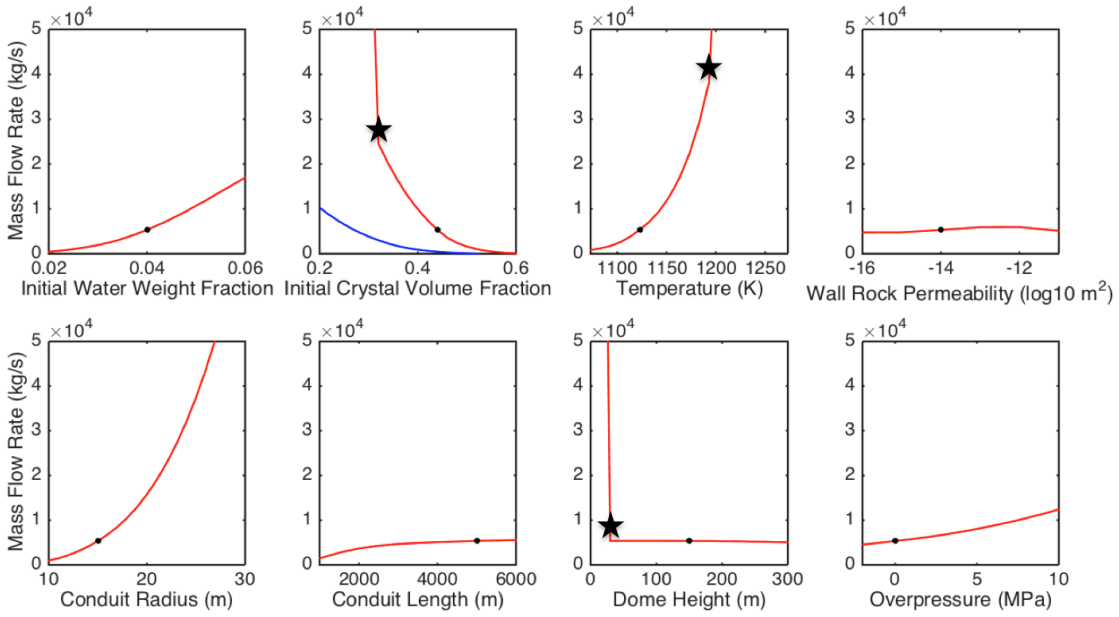

Figure 4.3. Variable effects on mass flow rate. Different parameters have different effects on the mass flow rate, shown here with each panel representing variation in one parameter while the others are held constant. Stars show where fragmentation occurs for initial crystal volume fraction, temperature, and dome height. The blue line in the initial crystal volume fraction panel shows the mass flow rate for a reduced water mass fraction of 0.02, which prevents fragmentation. The black dot in each panel indicates the conditions for the standard run (Table 4.1).

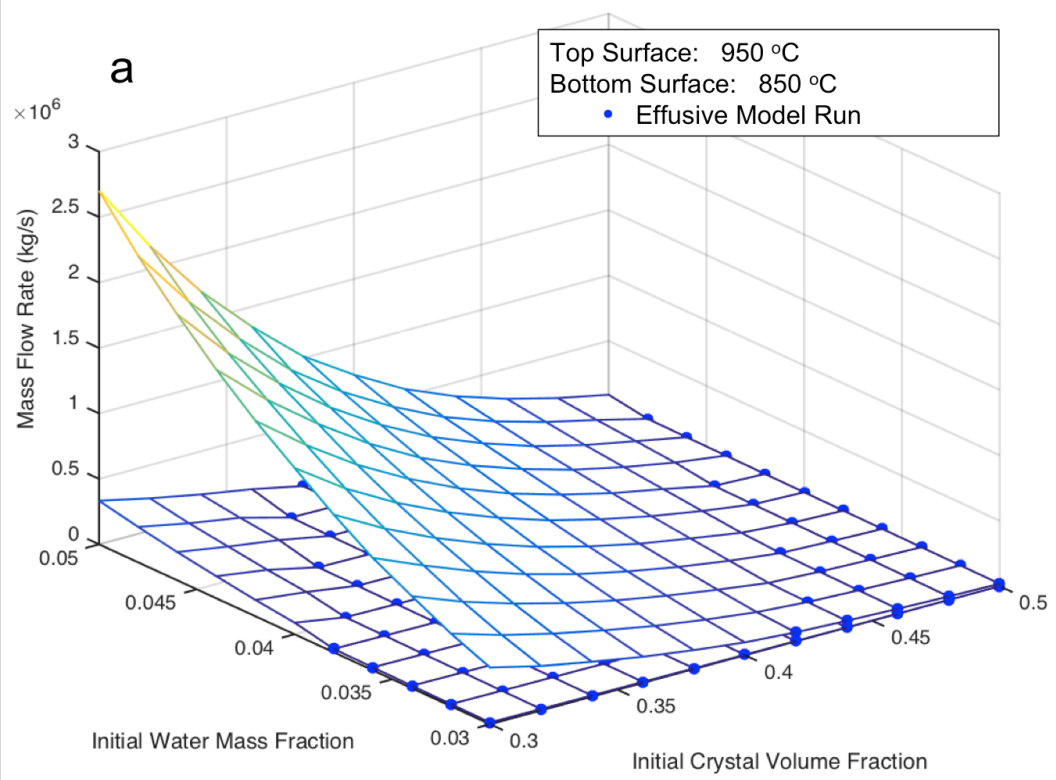

Figure 4.4. Effects of multiple parameters on mass flow rate. Sets of three different parameters are compared to show the effect on mass flow rate of initial water mass fraction, initial crystal volume fraction, and temperature (a), dome height (b), or overpressure (c). Each surface represents the mass flow rate for each value of the third parameter. Each intersection of lines on the surface grid is a model run. An effusive run is marked by a blue dot. The space between each surface shows the effect of changing the third parameter value, where more space between surfaces represents a greater effect. The highest rate of mass flow rate change is for the combination of the three parameters controlling viscosity (a), while dome height (b) shows a sharp increase in mass flow rate at the critical value for fragmentation and a steady rate of change for non-critical conditions. For the range I calculate, the effect of overpressure (c) is minimal compared to the effects of water and crystal content.

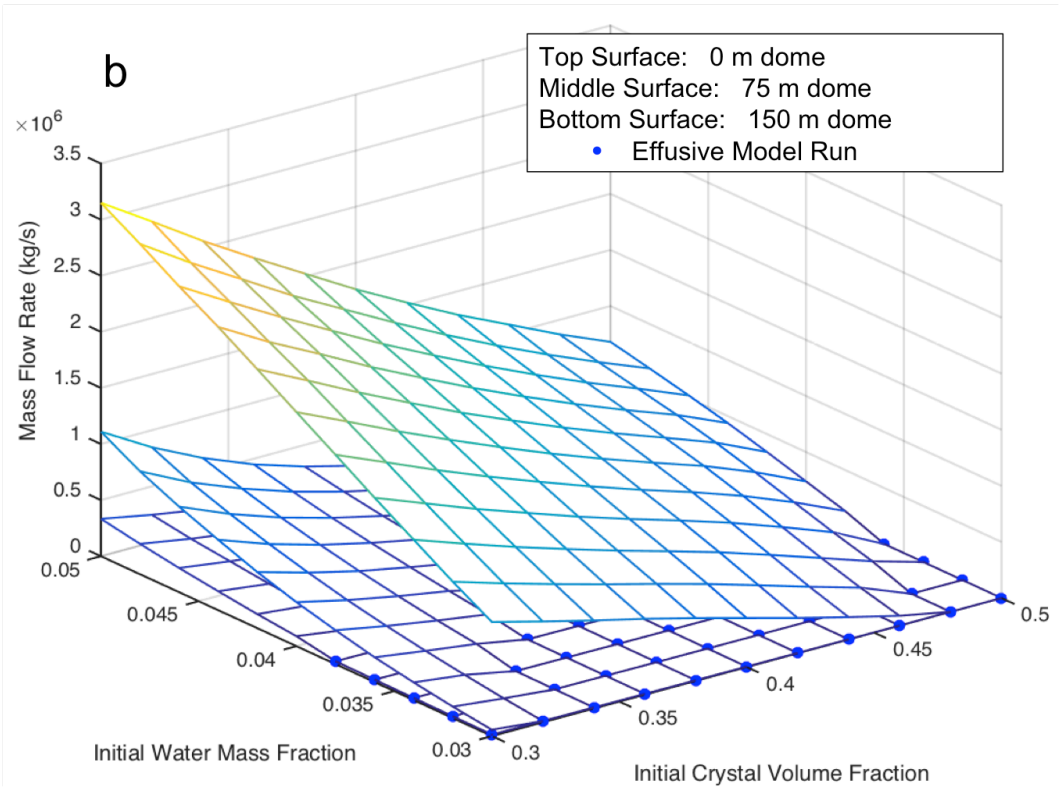

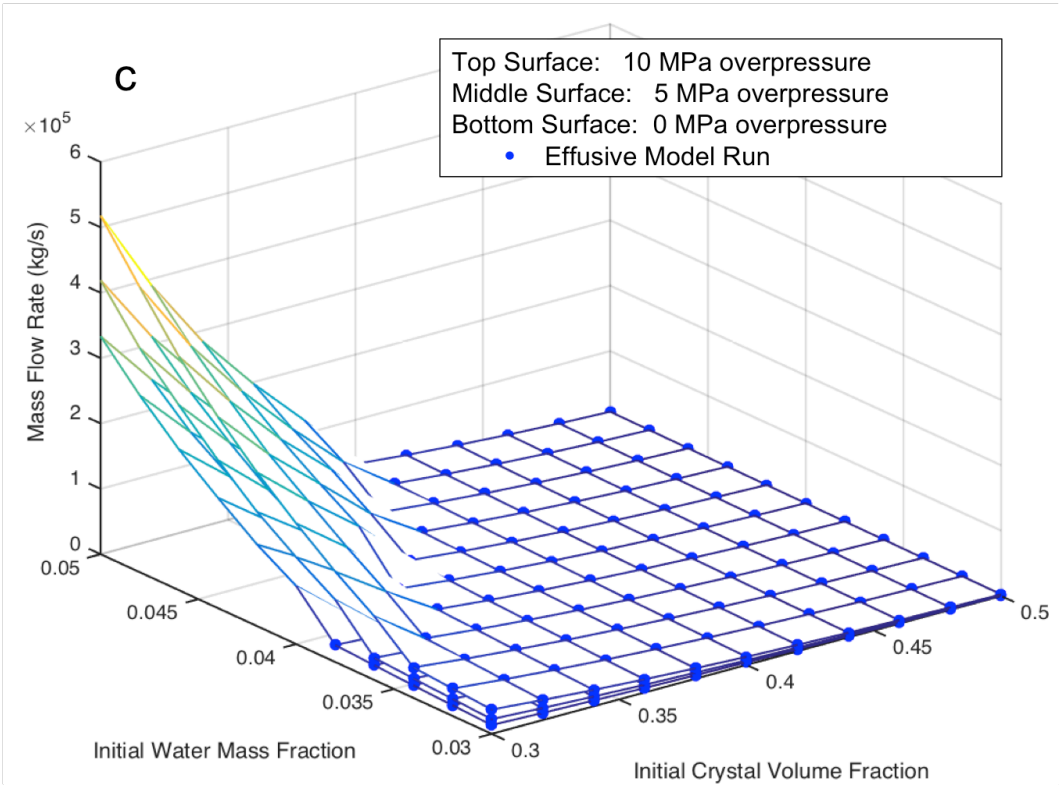

Figure 4.4 continued.

Figure 4.5 (following pages). Effects of multiple parameters on fragmentation. I show fragmentation as a phase boundary at conditions comparing 3 different variables: a) initial water mass fraction, initial crystal volume fraction, and temperature; b) initial water mass fraction, initial crystal volume fraction, and dome height; c) initial water mass fraction, initial crystal volume fraction, and chamber overpressure. Effusive conditions are towards the lower right and explosive conditions are towards the upper left. The fragmentation threshold is a solid line labeled by the value of the third parameter. For the labeled third parameter value, effusive conditions will occur for water and crystal content values below the curve, and explosive conditions will occur for water and crystal content values above the curve. The arrows (a) show how small changes in initial crystal volume fraction or initial water mass fraction can result in crossing the fragmentation threshold line for a temperature of 850 °C. A larger separation of the fragmentation lines indicates a greater effect on fragmentation by the third parameter. Black dots in each frame are model runs and show the input values of water and crystal content for each value of the third parameter.

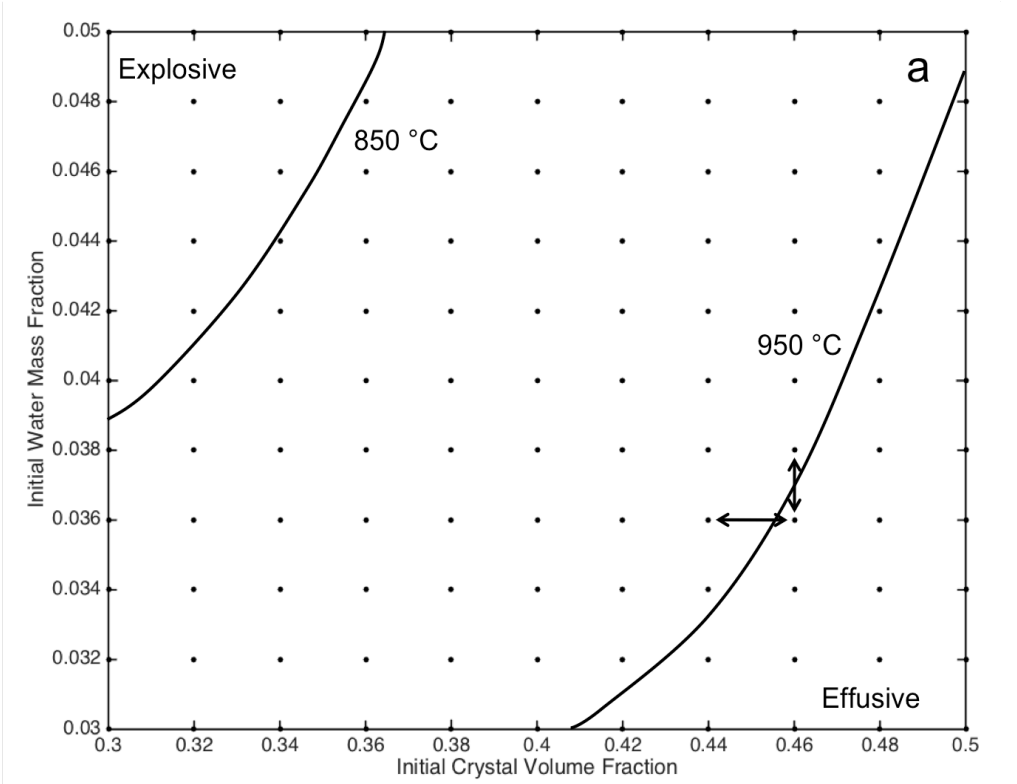

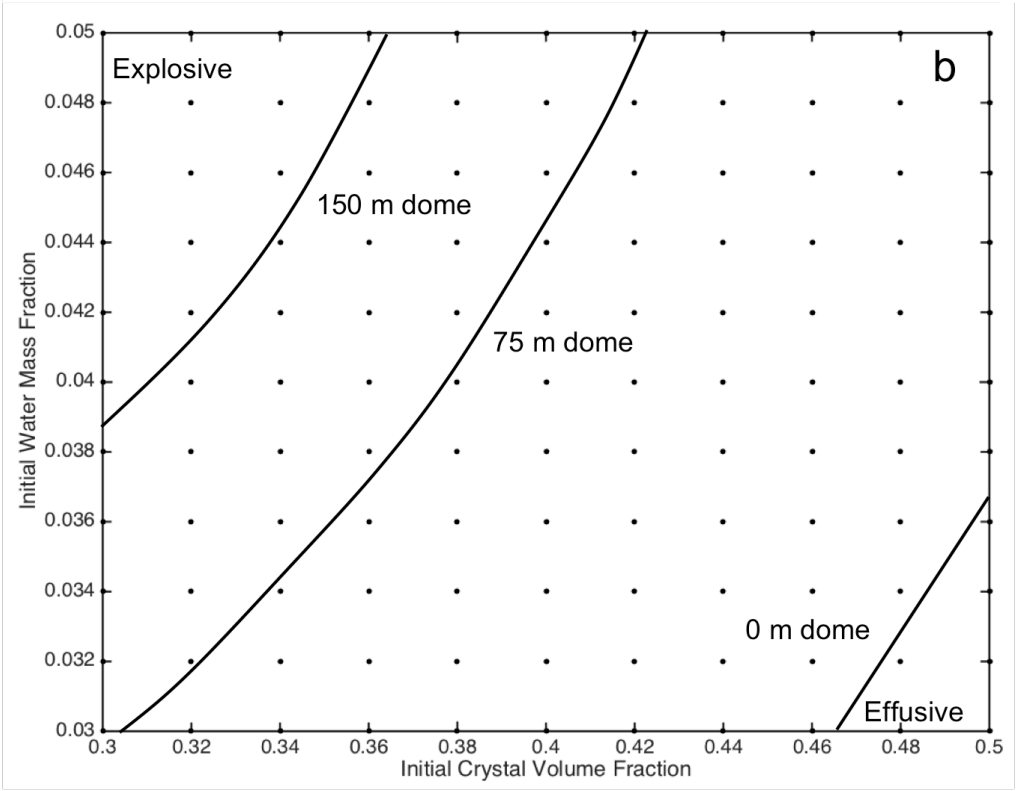

Figure 4.5 continued.

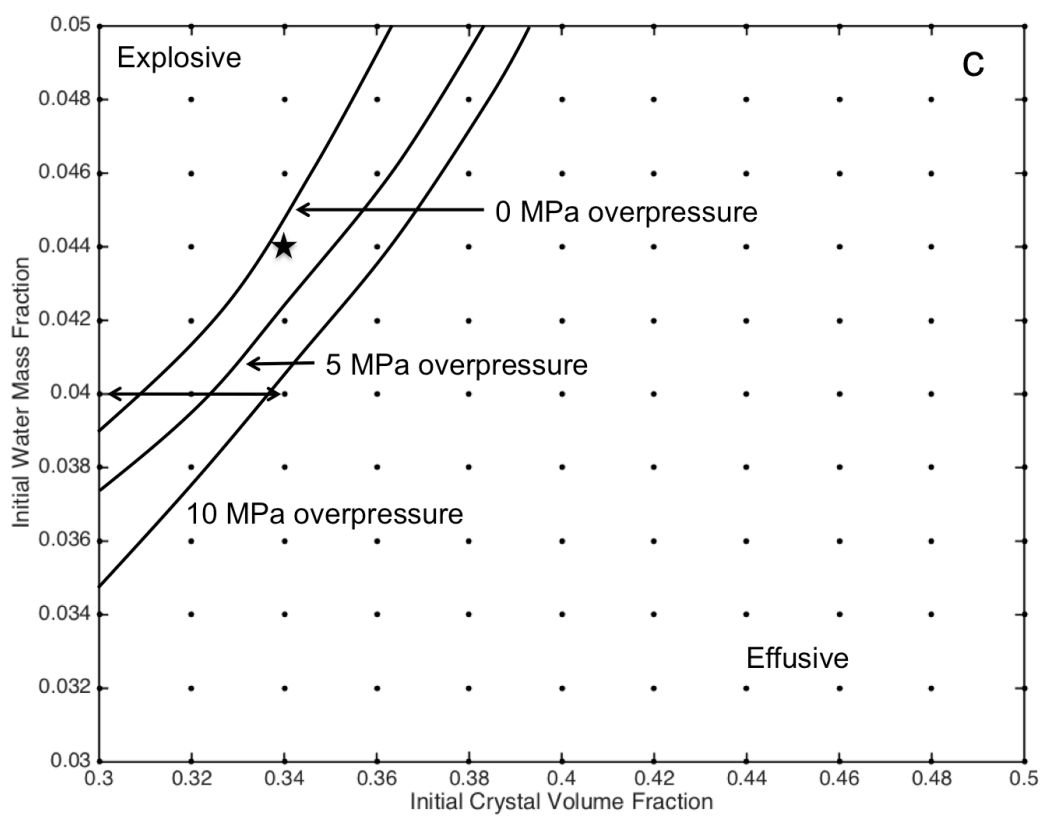

Figure 4.5 continued.

				Merapi 2010 Eruption Conditions						
	Unit	Standard Run	Merapi Liter-ature	Run 1	Run 2	Run 3	Run 4	Run 5	Run 6	Merapi 2006[1]
H_2O mass fraction		0.04	0.04-0.06[4]	0.04	0.04	0.04 1	0.04	0.04 1	0.05	0.025
Crystal volume fraction		0.44	0.3-0.5[5]	0.44	0.44	0.44	0.44	0.44	0.44	0.50
Temp	°C	850	950-1000[4]	970	970	970	970	970	970	950
Dome height	m	150	0-150[6]	50	130	130	120	0	0	250
Over-pressure	MPa	0		0	0	0	0	0	0	5
Wall-rock perm.	m^2	4.8×10^{-14}		4.8×10^{-14}	4.8×10^{-12}	4.8×10^{-12}	4.8×10^{-12}	4.8×10^{-12}	4.8×10^{-12}	4.8×10^{-14}
Conduit length	m	5000	1500-2500[7]	2000	2000	2000	2000	2000	2000	2000
Conduit radius	m	15		15	15	15	15	15	15	15
Mass flow rate[2]	Kg s^{-1}		10^6-10^7 [8]	1.4×10^6		1.6×10^5	1.9×10^5	3.7×10^6	5.3×10^6	
Volume flow rate[3]	m^3 s^{-1}	2.2	25-35[6]		28.1					3.5

1 Peak eruption phase, from ch. 2 of this dissertation

2 For explosive eruptions

3 For effusive eruptions

4 Costa et al., 2013

5 Hammer et al., 2000

6 Pallister et al., 2013a

7 Ratdomopurbo & Poupinet, 2000

8 Sparks et al, 1986 (based on plume heights of 12-17 km reported by Pallister et al., 2013a)

Table 4.1. Input parameters. Parameter values used as input for the numerical model for the standard run and Merapi 2010 eruption phases. Run 1 = October 26 initial explosive phase. Run 2 = Effusive phase. Run 3 = Initiation of Nov 4-5 explosive phase- H_2O change. Run 4 = Initiation of Nov 4-5 explosive phase- dome height change. Run 5 = Nov 4-5 explosive phase- low H_2O. Run 6 = Nov 4-5 explosive phase- higher H_2O.

CHAPTER 5

THE EMPLACEMENT OF THE ACTIVE LAVA FLOW AT SINABUNG VOLCANO, SUMATRA, INDONESIA, DOCUMENTED BY STRUCTURE-FROM-MOTION PHOTOGRAMMETRY

An effusive eruption at Sinabung Volcano in Indonesia began in December 2013. I use structure-from-motion photogrammetric techniques to create digital elevation models (DEMs) of the active lava flow. I build DEMs from photographs taken during two separate time periods and from two separate low-cost handheld cameras and compare them with a pre-eruption DEM to assess the quality and accuracy of photogrammetric DEMs created using different cameras, calculate flow volume and long-term average effusion rate, and document changes in flow morphology. On September 22nd, 2014, the lava flow was 2.9 km long and had a volume of $1.03 \pm 0.14 \times 10^8$ m^3, leading to an estimated average eruption rate of 4.4 ± 0.6 m^3 s^{-1}. Differencing the photogrammetric DEMs shows that during the two-week field campaign, topographic changes of the flow occurred in zones along the flow front and on the upper flank, a finding supported by relatively high temperatures in corresponding thermal images. The deformation can be explained by active advance at the flow front and development of instabilities and collapse on the upper flanks. Large pyroclastic density currents associated with collapse of upper-flank instabilities in October 2014 and June 2015 were caused by lava growing over ridges that had initially confined the flow to a pre-existing channel. This work demonstrates that structure-from-motion photogrammetry is a cost- and time- effective method of monitoring active volcanic features by accurately measuring the lava flow

volume and identifying changes in the flow related to flow advance and the development of gravitational instabilities.

5.1. Sinabung Volcano and Large Viscous Lava Flows

Sinabung is a 2460 m high andesitic stratovolcano located in the North Sumatra Province of Indonesia (Figure 5.1). Its ongoing eruption has produced ash columns over 10 km high, hundreds of block-and-ash type pyroclastic density currents (PDCs), and a 2.9 km long andesite lava flow (Global Volcanism Program, 2013; 2014b). Large viscous lava flows of this type are common at volcanoes around the world, but are rarely observed while active (Siebert et al., 2010). This eruption provides an opportunity to observe and document the emplacement of an active, high-viscosity lava flow with implications for improving our understanding of silicic eruption processes.

Sinabung has frequently produced voluminous viscous lava flows (Prambada et al., 2010), many of which can be identified on a digital elevation model (DEM) of the volcano (Figure 5.1). However, Sinabung had no confirmed historical eruptions prior to a brief 2010 event (Global Volcanism Program, 2013). Activity resumed at Sinabung in Fall 2013 and an effusive eruption began on December 24, when a new lava dome was observed (Global Volcanism Program, 2014a). Block-and-ash-style PDCs associated with dome collapse became frequent as the dome grew into a flow extending south down a valley, reaching 2.4 km long on March 13th 2014 (Global Volcanism Program, 2014a). From April through September 2014 the lava flow grew in both length and thickness, although PDC activity decreased (Sinabung Volcano Observatory, pers. comm.). On September 6, 2014, the lava flow was 2.9 km long (Global Volcanism Program, 2014b).

Large collapses of the upper part of the lava flow began on September 30, 2014, and June 2, 2015, resulting in renewed PDC activity (Global Volcanism Program, 2014b; 2015a). Two new lava lobes broke out at the collapse sites and redirected the flow of fresh lava away from the original axis such that, despite continued effusion, the main flow was no longer active and remains 2.9 km long (Global Volcanism Program, 2015b). As of this writing (July 2016) both new lobes remain active and are the sources of frequent PDCs (Global Volcanism Program, 2016).

5.2. Measuring active domes and flows

The methods for measuring the surfaces and estimating the volumes of active lava domes or flows have greatly improved over the past decades. The United States Geologic Survey (USGS) used aerial photographs to make high resolution (approximately 1 m grid size) DEMs of the Mount St. Helens lava dome in the 1980s (Fink et al., 1990), but the process took weeks. During the eruption of the Soufrière Hills Volcano on Montserrat (1995 – present), dome volume was monitored by a combination of theodolite, photographs, and laser range measurement surveys, producing volume calculations as frequently as every few days (Sparks et al, 1998). A laser distancemeter was used at Unzen Volcano in Japan during the 1990-1995 eruption (Nakada et al., 1999). The accuracy of these techniques is limited by the number and accuracy of survey points, forcing a trade off between spatial and temporal resolution. Dome volume can be rapidly estimated using a single-camera at a fixed point to measure dome height and/or radius and then assuming a simple geometry to calculate volume (e.g. Ratdomopurbo et al., 2013). Other methods of estimating volume or eruption rate, such as from satellite

thermal data, rely on empirical relationships and are not direct measurements of volume change (Harris & Baloga, 2009).

Multiple lava flows at Mount Etna in Italy have been measured using high-resolution techniques such as terrestrial laser scanning (TLS, James et al., 2009) and airborne LIDAR surveys (Favalli et al., 2010). Ground-based TLS provides accurate, high-spatial-resolution results, however, it can be limited by restricted coverage in rugged or dangerous terrain. Airborne LIDAR techniques, while producing the most accurate, complete, and high-resolution results, are costly and the logistics are not practical in many locations.

Advancements in computer processing power and software design have made photogrammetric techniques more practical for use in the geosciences (e.g., James & Robson, 2012). James & Varley (2012) and Diefenbach et al. (2012) use photogrammetric software (e.g. Bundler Photogrammetry Package, PhotoSynth™, and PhotoModeler Pro™) to process oblique airborne images of active lava domes and calculate volumes and eruption rates for Colima and Mount St. Helens volcanoes, respectively. Diefenbach et al. (2012) were able to create DEMs of Mount St. Helens comparable in resolution to those of the 1980's (Fink et al., 1990), but did so in less time and with commercially available digital cameras, in contrast to the expensive and specialized equipment necessary three decades earlier. Photogrammetry has also been used to model a lava lake (Smets et al., 2016) and to extensively map active lava flow fields at Mount Etna (James et al., 2012; James & Robson, 2014; De Beni et al., 2015).

All photogrammetry techniques are based on the concept that the three dimensional structure of an object can be determined by viewing the object at multiple

angles and distances. Structure-from-motion (SfM) refers to a specific photogrammetric technique that allows for the camera position and orientation and the geometry of the subject ('structure') to be estimated simultaneously from a wide range of views ('motion') (Snavely, et al., 2008). This technique makes photogrammetry more accessible, efficient, and economical as specialized camera equipment is not needed to reconstruct the 3D structure. Any set of digital photos of an object, provided there is significant overlap of the subject matter between images, can be used to produce 3D models. When additional spatial information, such as the coordinates of identifiable control points, is integrated with the 3D models, they can be georeferenced into high-resolution DEMs.

5.3. Methods

I conducted a field campaign at Sinabung September 17-29, 2014. My goals were to collect multiple sets of ground-based images in order to build photogrammetric models of the southeast flank of Sinabung. The photos were taken from roads surrounding Sinabung (Figure 5.1b) and encompass nearly 180° of viewing angles. I used two cameras to compare the quality of their resulting DEMs: 1) a Nikon D40X digital single-lens reflex (DSLR) camera (10.2 megapixels, 55 mm lens) and 2) an iPhone5 (8 megapixels, 33 mm lens). In total, I created four different DEMs of Sinabung- one from each camera at two different times during my field campaign. Additional details on processing workflow are included in Appendix A of this dissertation.

I used Agisoft PhotoScan Pro™ software to align my photographs and build dense point clouds. During these steps, I added spatial information to each model from a

combination of geotagged photographs from the iPhone5 and three dimensional control points on the Sinabung edifice manually identified in the images and in Google Earth™ (~10^0 m to 10^1 m position uncertainty). More accurately measured control points on Sinabung were not possible to obtain due to the ongoing eruption. I chose 6-7 control points to be evenly distributed across the field of view and in locations unlikely to be affected by volcanic activity. The main source of error in this process was the difficulty of manually placing the control points in the precise location on both the oblique field photograph and Google Earth™ aerial image, which I estimated to be ~10^1 - 10^2 meters (see Appendix A, Table A.1). Georeferencing each model using Google Earth™ provided a good initial spatial reference for checking model quality prior to further processing.

I further improve the spatial accuracy of my models using the Cloud Compare open source software (http://www.danielgm.net/cc/). In Cloud Compare, using 7-8 visually identifiable control points located in unchanged areas of the volcano, I use a manual rigid-body transformation to align the unchanged portions of the point cloud of each model to a point cloud derived from a 5 m pre-eruption DEM of Sinabung provided to me by the Badan Informasi Geospasial and the Center for Volcanology and Geological Hazard Management (CVGHM) in Indonesia. The root mean square (RMS) error for each model alignment ranged from 26 to 51 meters (see Appendix A Table A.2). I visualize the flow thickness for each model using the vertical component of the cloud-to-cloud distances (absolute value) calculated for this alignment. I did not try to do a global alignment of all of the data because the lava flow occupies a large fraction of each of my models. The automated iterative closest point (ICP) method (Besl and McKay, 1992)

would have attempted to average the lava flow into the transformation and created large errors.

I converted my point clouds into DEMs using a thin plate spline in ArcGIS™ and resampled to a 5 m cell size. I then subtracted the pre-eruption DEM from my DEMs, leaving only the values of flow thickness (ΔZ) and residual errors. I separated the flow thickness and residual errors by clipping the difference DEM to two regions for each model: 1) the flow area containing the flow thickness values as determined by examining the hillshade of the DEM in ArcMap™ and the point cloud in Photoscan™ and 2) the non-flow area of the DEM containing the residual errors where there is minimal change (Figure 5.2). I drew the outer boundary of the non-flow region such that the point density of the corresponding point clouds is ~> 0.01 points/m^2 (see Table 5.1 for average point density for each model calculated using lasgrid from lastools–https://rapidlasso.com/) and concavities in the boundary were minimized (Figure 5.2).

I use the residual elevation differences in the region of my DEMs outside of the lava flow (light blue outline, Figure 5.2) as the indication of the vertical error as in Albino et al. (2015) and correct an overall elevation bias in each photogrammetric DEM by the average of the residual differences ($\overline{\Delta Z}_{nf}$, Table 5.1). This approach is valid provided the set of vertical differences in the assumed unchanged area for each model approximates a normal distribution about its mean, which I show to generally be the case in Figure 5.3. The standard deviation of the residual differences (σ_{nf}, Table 5.1) can then be used as the estimate for the vertical error (Wheaton et al, 2010; Albino et al., 2015). I assume the contribution to the volumetric error in each DEM from horizontal errors is negligible due to the relatively low and uniform slopes on the pyroclastic flow plain

surrounding the lava flow (e.g., Wheaton et al., 2010). I limit the volume calculation to only the area covered by the lava flow (red outline, Figure 5.1b). The volume of the lava flow (V) is then

$$V = \sum_{i=1}^{n} \left(\Delta Z_i - \overline{\Delta Z}_{nf} \right) A \tag{5.1}$$

and the volumetric error is

$$V_{error} = nA\sigma_{nf} \tag{5.2}$$

where n is the number of pixels in the flow area and A is the pixel area (25 m^2).

I also compare my 3D models to each other in Cloud Compare to identify changes in the flow that may have occurred between photo acquisitions (September 18th – September 22nd, 2014). An ICP analysis is appropriate in this case as the difference between the clouds is minor compared to the size of clouds (Appendix A, A.2). The iterative closest point technique finds a single rigid body transformation that best aligns two different point clouds (Besl and McKay, 1992). After the point clouds are aligned, I calculate the cloud-to-cloud distance, which returns the smallest distance from each point in one cloud to a point in the other cloud. For my application, the regions of the aligned point clouds with the greatest cloud-to-cloud distances highlight areas where collapses of lava or advancement of the flow front have occurred.

5.4. Results

I created four models of the Sinabung lava flow (Table 5.1) from two periods of photo acquisition: 1) September 17 & 18 (Models 1 & 2 with the iPhone and DSLR, resp.) and 2) September 22 (Models 3 & 4 with the iPhone and DSLR, resp.). The

resolution of the DEMs is directly related to the resolution of the photographs used to create them (Table 5.1). However, the accuracy of the models is more closely correlated to the clarity of the images. On September 17 & 18 (Models 1 & 2), viewing conditions at Sinabung were limited by atmospheric haze and clouds. Poor visibility decreases model accuracy by limiting the detail captured in the photographs and precludes views from multiple angles. The error for Models 1 & 2 was 0.27 x 10^8 m^3 (22.1% of the volume estimate) and 0.29 x 10^8 m^3 (27.6%), compared to only 0.19 x 10^8 m^3 (17.2%) and 0.14 x 10^8 m^3 (13.8%) for Models 3 & 4 on September 22, which was a clear day. For these reasons, Model 4 (Figure 5.4) is the best model as it was made with photographs from the best camera (Nikon DSLR) on the day with the clearest weather (Sept. 22).

From Model 4 in comparison with the pre-eruption DEM as explained above, I find that on September 22, 2014, the volume of the Sinabung lava flow was 1.03 ± 0.14 x 10^8 m^3 (0.1 km^3) (Table 5.1). Using December 24, 2013, as the starting point of the effusive eruption, the average eruption rate at Sinabung for those nine months was 4.4 ± 0.6 m^3 s^{-1}. The volume estimates from the other models overlap within error (Table 5.1), supporting the accuracy of my measurements.

By subtracting the pre-eruption DEM from my DEMs I create a map of the thickness of the lava flow (Figure 5.5a). Topographic profiles across the flow (Figure 5.5b – 5f) show that the thickest part of the flow is around 160 m near the summit (Figure 5.5b) and that the flow front is consistently ~100 m thick (Figure 5.5f). By the time of Model 4, the flow had overtopped the southwestern (left) ridge of the valley that initially confined the lava (Figure 5.5b – 5c). This led to increased instability of the flow in this

area, as it was the source of frequent rock falls during my field campaign and the September 30, 2014, collapse event. The profiles also identify areas of erosion (*, Figure 5.5c – 5d) and deposition (★, Figure 5.5b – 5d) from PDCs. I attribute similar patterns in Figure 5.5e ('+') and on the ends of each profile to local regions of decreased DEM accuracy caused by edge or topographic shadowing effects that limited my ability to image these areas in multiple photographs.

My comparative analysis of Models 2 and 4 show areas where the flow morphology changed between acquisitions (5 days) of the photos used to create the models (Figure 5.6a). The regions that exhibit the biggest changes between DEMs correspond to zones of higher temperature observed in ground-based thermal images acquired with a FLIR ONE™ camera attachment for the iPhone5 (Figure 5.6b). These regions also correspond to the source locations of rock falls observed in the field and fumarolic activity. The region of greatest change is located at the flow front. The maximum change of ~35 m is greater than the Model 4-to-Model 2 alignment RMS error of 19.7 m, and I thus estimate corresponding flow advancement of 3-11 m d^{-1} in these isolated zones (Figure 5.6c). Areas along the upper east edge of the flow also show high relative change and correspond to surface change by rock falls as lava began to overtop this ridge (Figure 5.5b – 5c) and consequently became gravitationally unstable. A moderate-sized collapse in this region (Figure 5.4c) on September 24th, 2014, generated a 2 km-long PDC (Sinabung Volcano Observatory, pers. comm.).

5.5. Discussion

My results highlight ongoing activity over a two-week period during Sinabung's persistent effusive eruption. At the time of my observations, emplacement of the flow was focused at isolated regions along the flow front 100-200 meters wide where hotter lava from the flow interior was able to push through the thick insulating crust (Figure 5.4d). My measurements of the advancement of the flow in these regions (Figure 5.6c) suggest a maximum rate of 3-11 m d^{-1}. These advancing or breakout regions are similar in size and advance rate to those described by Tuffen et al. (2013) at the Cordón Calle rhyolite flow in Chile. Additionally, Sinabung observatory staff noted that the flow inflated as flow advance slowed in April-September 2014 and aerial images show well-developed pressure ridges on the flow surface. These observations support previous work demonstrating that viscous flows can have similar properties to basalt flows and thus their emplacement is likely controlled by similar processes (Harris et al, 2004; Tuffen et al., 2013).

The hazard of PDCs caused by the collapse of unstable regions of the flow is directly linked to flow emplacement processes. Data compiled by the Global Volcanism Program (2014b) describe both flow advance rate and PDC activity decreasing around the same time in April 2014, despite visual observations of flow inflation and seismic signals that indicated continued effusion of lava. This observation demonstrates that PDC activity during effusive eruptions is correlated to flow advance rate, in addition to the effusion rate, as has been shown in previous studies (Nakada et al., 1999; Calder et al., 2002; Chapter 2, this dissertation). My observations of frequent rockfall in the regions of flow front breakouts (Figure 5.6), while no rockfalls occurred along other regions of the

flow margin, further supports the idea that instability and collapse are directly related to the advance of the flow. Furthermore, identifying the locations of the most active advance along a flow front, through photogrammetry or other methods, can inform collapse hazards for areas downslope of these parts of the flow.

I identify another process responsible for large collapses, as renewed PDC activity in September 2014 and June 2015 did not coincide with an increase in flow advance rate or effusion rate (Global Volcanism Program, 2014b). Instead, my topographic data show that the renewed activity appears to have been caused by inflation of the flow that filled and then overtopped the valley that originally confined it (Figure 5.5b – 5c), leading to large PDC-generating collapses. The topography confining lava flows is thus an additional factor that controls the development of collapses of the lava. This process was also observed at Merapi Volcano in 2006 when, rather than overtopping a ridge as at Sinabung, the weight of the lava dome caused a section of the crater wall to collapse, releasing the confining force on the dome and causing large collapses that traveled down a drainage that had not seen PDC activity in decades (Ratdomopurbo et al., 2013; Chapter 2, this dissertation).

Instabilities related to topography (that is, by overtopping or failure), unlike those related to effusion or flow advance rates, do not require higher levels or changes in activity to develop. Specifically, the collapses referred to above at Merapi and Sinabung occurred in the weeks or months *following* the peak eruption phases. Topographic instabilities can build slowly over time and collapse when other observations may suggest that a volcano's activity is at low levels and is less hazardous. The unexpected, larger-than-average PDCs that result have been deadly at Sinabung, causing fatalities in

February 2014 (Global Volcanism Program, 2014a) and May 2016 (Global Volcanism Program, 2016) when people temporarily re-entered the exclusion zone within 5 km of the vent during periods they may have themselves perceived to be of comparatively low activity. The evidence from Sinabung and Merapi suggests that topography-generated instabilities are most likely to develop in steep terrain around the vent and upper flanks of the volcano, where crater walls and ridges can confine the flow, allowing lava to accumulate. An understanding of changing volcano edifice topography at sufficient resolution is thus necessary to fully understand PDC hazards.

I am not able to determine a PDC deposit volume at Sinabung separately from the lava flow volume. Any PDC deposits since covered by the lava flow are included in the lava flow volume estimate. Small areas of deposition and erosion in the topographic profiles (Figure 5.5b – 5f) are on the same scale as my errors and are not included in my volume calculation as they are outside of the flow area. If PDC deposits constituted a significant volume of material beyond the flow margins, this layer of deposits would appear in my flow profiles (Figure 5.5b – 5f) as misalignment between Model 4 and the pre-eruption DEM, but this is not observed. Model 4 has a vertical error of ± 8.2 m (Table 5.1), so I conclude that the thickness of pyroclastic deposits is less than this error and thus adds no significant volume to my estimate.

Structure-from-Motion has broad applications for observing volcanoes and documenting their activity (e.g. James & Robson, 2012; Diefenbach et al, 2012; De Beni et al., 2015; Smets et al., 2016). I show that oblique, ground-based photographs can be used with SfM to generate 3D photogrammetric models that allow for the calculation of volumes of erupted material and identification of regions with measureable change. The

accuracy of the models is most improved by having clear weather that enables photographs from all necessary angles to be taken in one day. The quality of the camera improves the DEM resolution but does not guarantee improved accuracy (Models 1 & 2, Table 5.1); a good model can be made using only the camera on a smart phone (Model 3, Table 5.1), as also demonstrated by Micheletti et al. (2015).

The techniques described here can easily be utilized by volcano observatories, as they require no expensive equipment or specialized expertise. A standardized workflow for an observatory could be similar to the following: 1) establish a standardized set of control points on the volcano to use for georeferencing; 2) take photographs from around a volcano (ideally using a camera with geotagging capability) every few days or whenever a clear-weather opportunity presents itself – this task can be accomplished by 1-2 people in a few hours; 3) follow all processing steps as described in section 5.3 above and in Appendix A. Additionally, if the purchasing of software licenses is not feasible, the alignment, georeferencing, and data processing steps I describe can be accomplished using freely available, open source alternatives such as Bundler Photogrammetry Package, Cloud Compare, lastools, and R (a software environment for statistical computing and graphics, https://www.r-project.org/). Frequent surveys conducted by an observatory could be used to create a time series of models with which to document and quantify effusion rate, advancement of the flow, and areas of high change in lava flows and domes that are at risk of collapsing and generating PDCs. This repeat survey method is more time- and cost-effective than other methods to generate topographic data while having similar (or better) accuracy.

5.6. Conclusions

The activity of the andesite lava flow at Sinabung presents an opportunity to observe the progression of a ubiquitous, but rarely observed, style of silicic volcanism. The ongoing activity shows that these are dangerous eruptions with persistent hazards not limited to the initial explosive and rapid lava flow advance phases. A relatively steady effusion of lava causes periods of low and high PDC activity as the lava switches from flowing down a confined valley to overtopping that valley, leading to large collapses. PDC activity during silicic effusive eruptions is thus related to the effusion rate, flow advance rate, and the underlying topography. Structure-from-motion photogrammetry techniques are ideal for documenting these types of eruptions. Because of the low cost and relative ease, I was able to achieve both high accuracy and good temporal resolution. I find that 0.1 km^3 of lava had erupted at Sinabung since effusion began in late 2013 at a long-term average rate of 4.4 $m^3 s^{-1}$ through September 2014, with an error of ~14%. I compare multiple photogrammetric models and identify isolated regions of rapid flow advance at the front of the flow, as well as high rates of change in a region on the upper flanks that collapsed two days after the photos were taken. Structure-from-motion photogrammetry can be used to continuously, efficiently, and safely monitor activity and hazards and provide insight on the processes controlling ongoing eruptions.

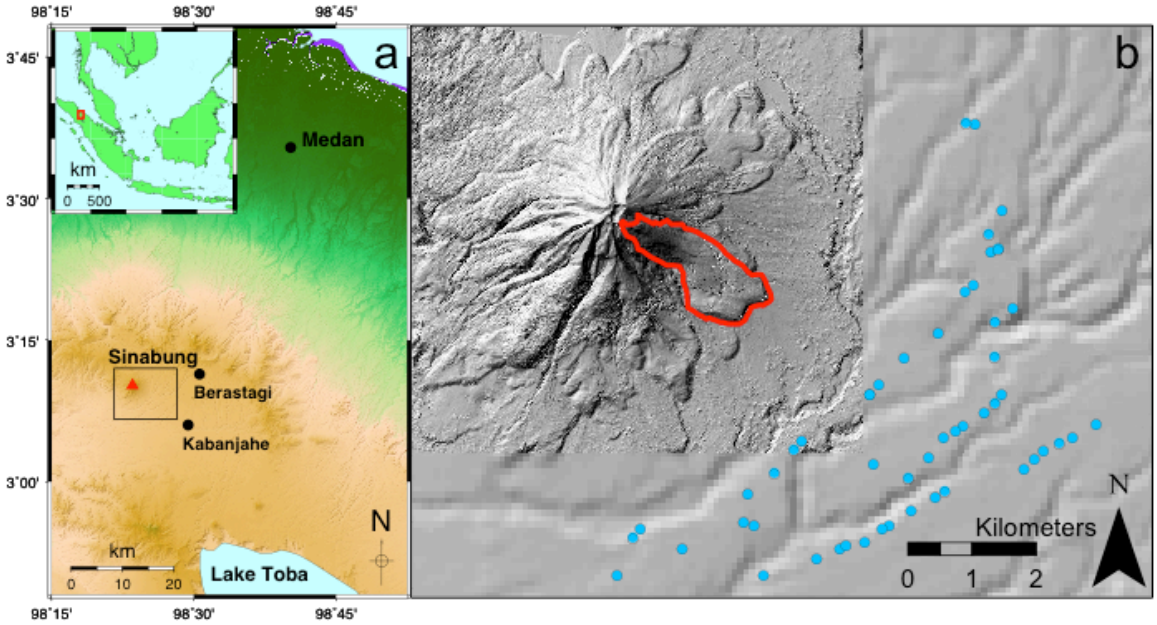

Figure 5.1. Location of Sinabung Volcano. Sinabung (triangle) is located in the North Sumatra Province of Indonesia (a). The location of the region detailed in (b) is outlined in black. **Inset:** location of (a) (red box) on the island of Sumatra. The extent of the active lava flow on September 22, 2014 (red outline) and the camera locations for Model 3 (blue dots) are shown on 5 meter and 90 meter DEMs from the Badan Informasi Geospasial and Shuttle Radar Topography Mission, respectively (b).

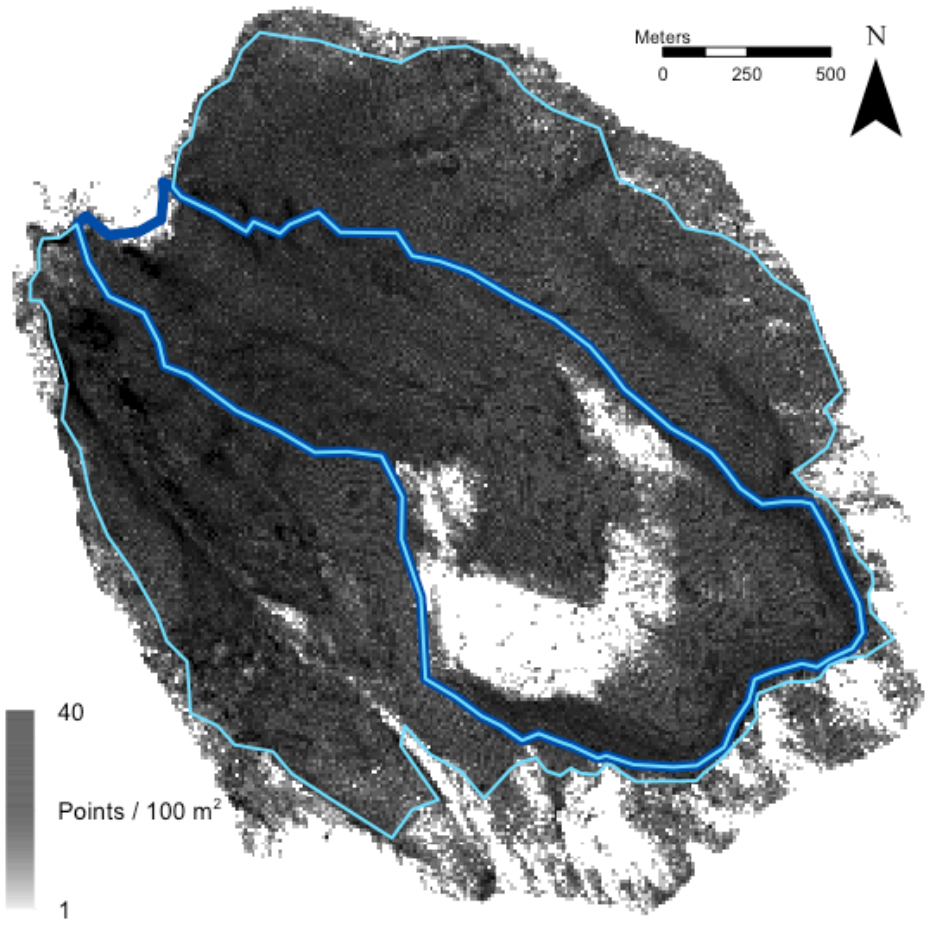

Figure 5.2. Model 4 dense point cloud point density. Points per 100 m^2 (10 meter cell size) for the Model 4 point cloud. I generally limited inclusion in the non-flow region to areas with ~> 1 point per cell in this image (a point density of ~>0.01 pts/m^2). The dark blue outline is the lava flow extent and the light blue outline is the non-flow region chosen for this model.

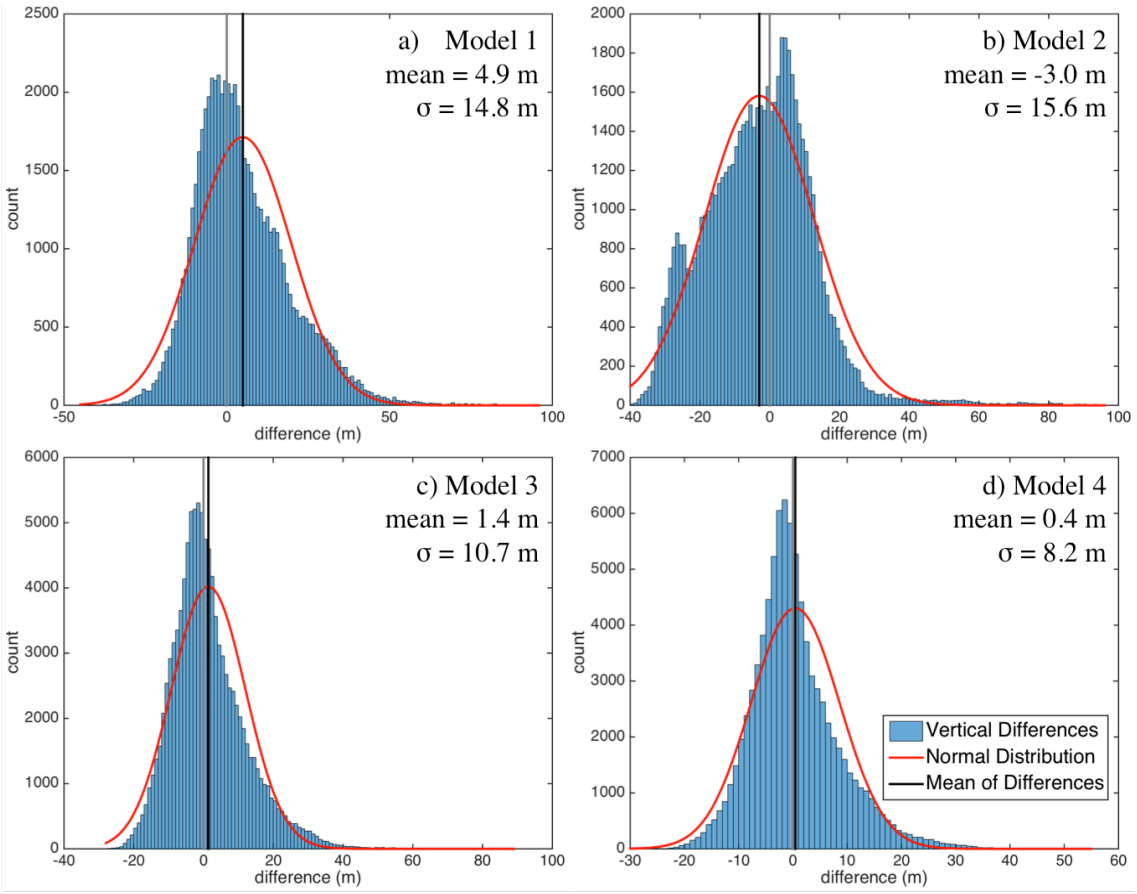

Figure 5.3. Histograms of vertical difference errors. Histograms of the non-flow vertical differences for each Model 1 (a), Model 2 (b), Model 3 (c), and Model 4 (d). Each histogram generally follows a normal distribution (red line), with the more accurate models having better fits. The black vertical line in each plot is the average of the vertical differences (Table 5.1), and represents the elevation bias for which I correct each model before calculating the lava flow volume. The distance between the black line and the gray line (at difference = 0) represents the magnitude of the elevation bias for each model. The standard deviation of these differences is used as the estimate of vertical error for each model (Table 5.1).

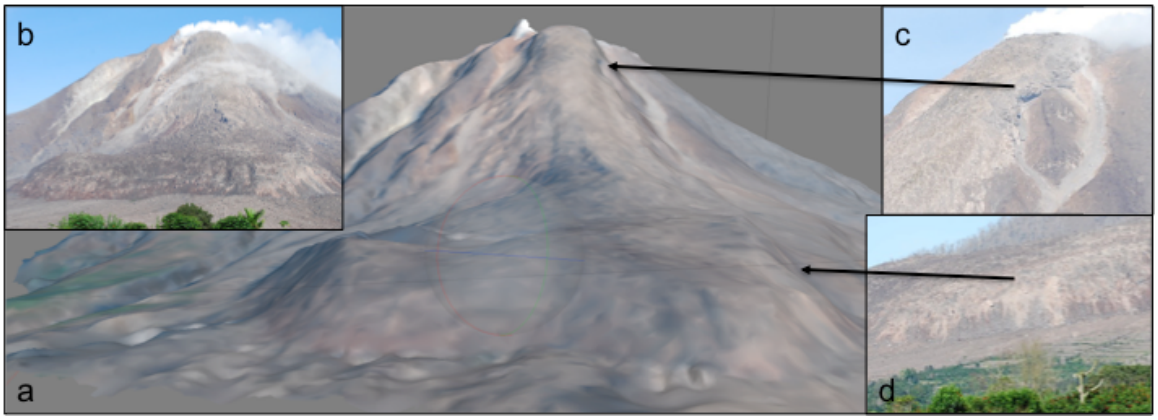

Figure 5.4. Photogrammetric model of Sinabung. A view of the 3D model for Model 4 (Table 5.1) in Photoscan™ is shown in (a). A photo used to make the model taken at a similar view angle to the model perspective is shown in (b). Areas of active and observable change in the flow include a gravitationally unstable region of the upper flank (c) and a slowly advancing breakout region near the flow front (d).

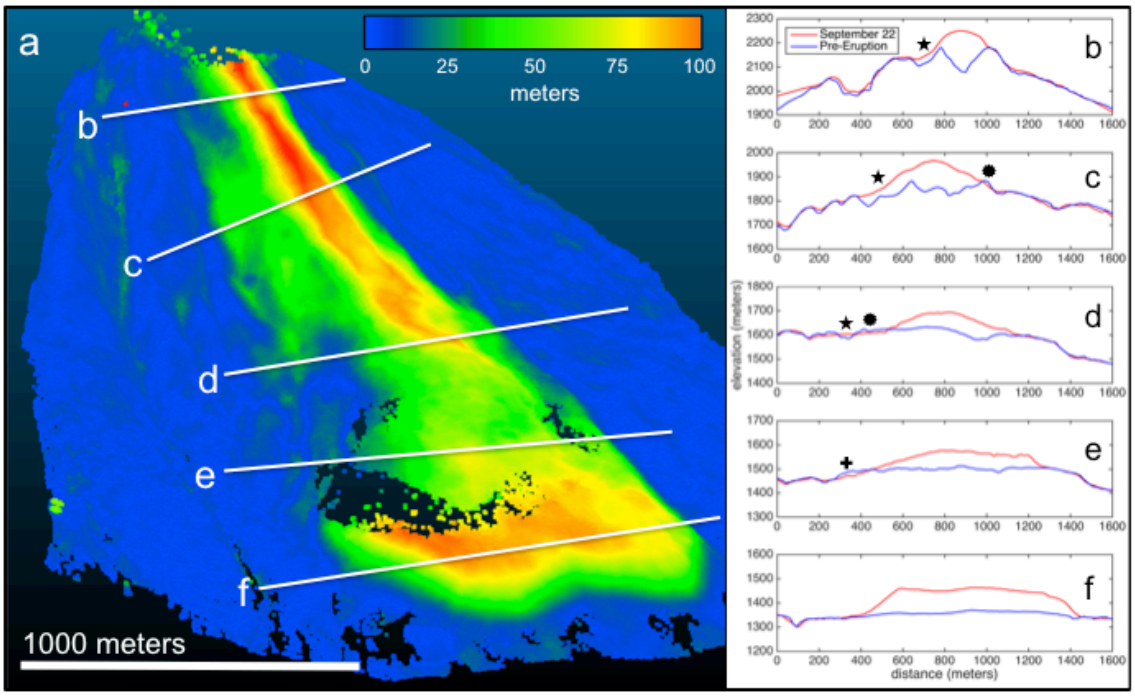

Figure 5.5. Thickness map and profiles of Sinabung lava flow. A thickness map of the Sinabung lava flow in shown in (a). White lines show the trace of the profiles across the flow shown in (b-f). White scale bar in (a) refers to distance scale. Color scale bar in (a) refers to flow thickness. See text for explanation of the symbols in (b-f).

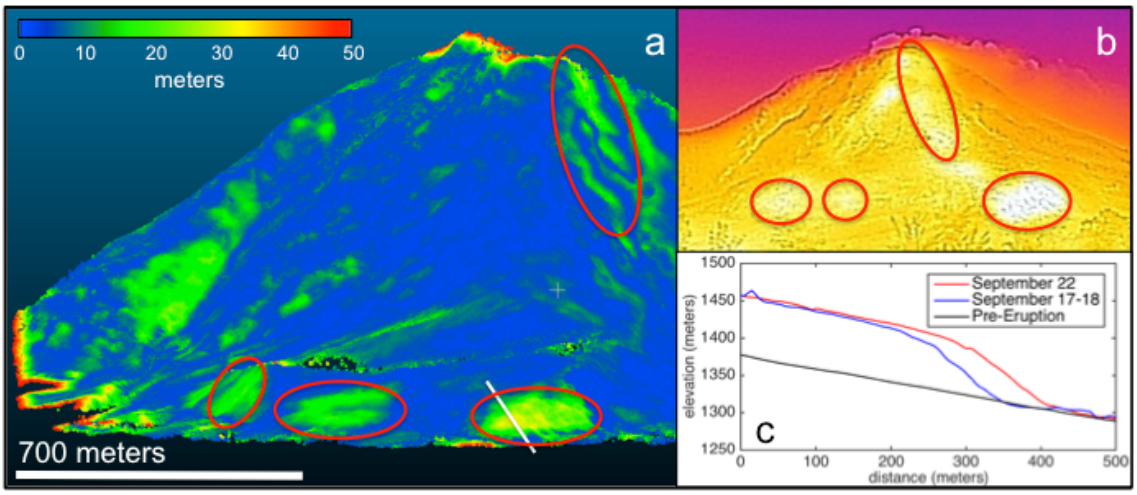

Figure 5.6. Change Detection at Sinabung by SfM. A map of change in the flow calculated by ICP analysis of Model 2 and Model 4 (Table 5.1) is shown in (a). White scale bar refers to distance scale. Color scale bar refers to cloud-to-cloud distances. White line is location of profile shown in (c). A forward-looking thermal image of Sinabung (b) shows regions of higher temperature (brighter yellow to white) on the flow corresponding to the areas of greatest change in (a). The regions of greatest change and higher temperature (circles) are found at the flow front and upper flanks. A profile across the flow front (c) shows the advance of the flow that occurred between Models 2 and 4.

Model	**1**	**2**	**3**	**4**
Camera	iPhone 5	Nikon D40X	iPhone 5	**Nikon D40X**
Date	9/17-18/2014	9/17-18/2014	9/22/2014	**9/22/2014**
Weather	Haze & Clouds	Haze & Clouds	Clear	**Clear**
# of Photos	27	39	54	**54**
DEM resolution (m/pix)	5.27	3.37	6.51	**3.84**
Point Density (pts/m^2)	0.036	0.088	0.024	**0.068**
Dense Cloud Points	134,060	425,607	188,367	**386,883**
Flow surface area (m^2)	1.83 x 10^6	1.86 x 10^6	1.81 x 10^6	**1.74 x 10^6**
$\overline{\Delta Z}_{nf}$ **(m)**	4.9	-3.0	1.40	0.44
σ_{nf} **(m)**	14.8	15.6	10.7	**8.2**
Volume (m^3)	1.14 x 10^8	1.11 x 10^8	1.09 x 10^8	**1.03 x 10^8**
V_{error} **(±m^3)**	0.27 x 10^8	0.29 x 10^8	0.19 x 10^8	**0.14 x 10^8**
% Error	22.1%	27.6%	17.2%	**13.8%**
Effusion rate (m^3/s)	4.9	4.7	4.7	**4.4**
Effusion rate error (±m^3/s)	1.2	1.3	0.8	**0.6**

Table 5.1. Summary of data for the four photogrammetric models of Sinabung.

CHAPTER 6

MECHANISM OF LAVA FLOW EMPLACEMENT DURING THE EFFUSIVE ERUPTION OF SINABUNG VOLCANO (SUMATRA, INDONESIA)

The ongoing effusive eruption of Sinabung Volcano (Sumatra, Indonesia) began in late December, 2013, and has produced a 2.9 km long central lava flow with two active secondary summit lobes, and frequent pyroclastic density currents (PDCs) (≤ 5 km long) with associated plumes over 5 km in height. Large viscous lava flows of the type documented here are common at volcanoes around the world, but are rarely observed while active. This eruption provides a special opportunity to observe and study the mechanisms of emplacement and growth of an active viscous lava flow. I use visual and thermal satellite images to document the flow and describe the processes driving emplacement of the lava over the course of the eruption. Effusion and flow advance rates were at their highest in January-March 2014. A decrease of flow advance rate in late March 2014 from > 20 m d^{-1} to < 5 m d^{-1} was the result of a decrease in effusion rate from ~7 m^3 s^{-1} to ~3 m^3 s^{-1}. Initial flow emplacement was controlled by the yield strength of the flow crust, which I estimate to have increased in thickness from 1 to 4 meters during January-June 2014, calculated from average flow surface temperatures that decreased from ~60 °C to < 30 °C during this period. Further decrease in flow advance rate in June 2014 to ~1 m d^{-1} suggests that the flow's interior had cooled, and that propagation was limited by the yield strength of the flow's interior (core). Inflation of the flow during this period of core-controlled slow advance caused lava to overtop ridges bounding the flow near the summit, and created significant gravitational instabilities.

This interpretation is supported by the generation of PDCs due to collapse of the upper portion of the lava flow and consequent breakout of new flow lobes at the site of the collapses in October 2014 and June 2015. Both upper lobes remain active as of June 2016 and present a significant hazard for collapse and generation of PDCs. This ongoing activity appears to represent a typical eruption of Sinabung, with flow length and area similar to numerous older flows observed around the volcano.

6.1. Introduction

Viscous lava flows are a common style of volcanism (Siebert et al., 2010) but are rarely observed while active, limiting our understanding of their emplacement mechanics and associated hazards. The ongoing effusive eruption at the 2640-meter-high Sinabung Volcano, located in the Karo Regency of the North Sumatra Province of Indonesia (Figure 6.1) offers an opportunity to observe the emplacement of a viscous lava flow and study the associated processes. In this chapter, I identify and explore the different styles of emplacement that have occurred at Sinabung and show the relationship between these styles, and effusion and flow advance rate. I also apply simple models of flow advance to derive material properties of the lava. My methods highlight the value of satellite remote sensing for monitoring eruptions and estimating a range of eruption quantities, from effusion rate to lava viscosity. My results can be used to better understand the continued hazards associated with the Sinabung eruption, and better anticipate eruption processes and hazards during effusive eruptions at silicic volcanoes in the future.

6.1.1. Current Eruption of Sinabung

The emplacement of viscous lava flows is the most common style of activity at Sinabung (Prambada et al., 2010) and multiple older flows can be observed in a 5-meter digital elevation model (DEM) of the volcano from 2010 (Figure 6.1). The current effusive eruption of Sinabung Volcano began on December 24, 2013, following four months of intermittent explosive activity (Global Volcanism Program, 2014a). Erupting lava first formed a lava dome and then began to flow down a south-facing valley. The Sinabung Volcano Observatory noted that the flow was 1.5 km long on 31 January 2014, and 2.4 km long on March 13 (Global Volcanism Program, 2014a). During this period of lava flow advance, collapses of the unstable flow front were common and produced block-and-ash style pyroclastic density currents (PDCs) that travelled up to 5 km from the vent and had associated plumes up to 5 km tall. At their peak, tens to hundreds of PDCs occurred each day (Global Volcanism Program, 2014a).

By 6 April 2014, the flow had advanced only another 100 meters, and was 2.5 km long (Global Volcanism Program, 2014a). From April through September 2014, PDC activity was relatively low compared to earlier in the year, and the lava flow reached 2.9 km in length (Global Volcanism Program, 2014b; Chapter 5, this dissertation) in mid-September. On 22 September 2014, the flow front was 100 m thick and the upper part of the flow had filled the valley that initially channeled the lava to a thickness of up to 160 meters (Chapter 5, this dissertation).

Beginning on 30 September 2014 and continuing through the end of the year, a large collapse on the south side of the upper part of the flow renewed PDC activity (Global Volcanism Program, 2014b). A new lava lobe grew out of the scarp, and

collapses from the front of this lobe caused numerous PDCs (Global Volcanism Program, 2014b). Activity decreased in early 2015 until a similar collapse and lava lobe outbreak occurred on 2 June 2015, on the east side of the upper flow (Global Volcanism Program, 2015a). These collapses and new flow lobes cut off the original flow from the vent and it remains ~2.95 km long, having advanced only a few meters since September 2014 (Global Volcanism Program, 2015b). As of this writing (July 2016), effusion of fresh lava is ongoing and PDCs occur daily (Global Volcanism Program, 2016).

6.1.2. Emplacement of viscous lava flows

Laboratory and field data paired with flow models demonstrate that the advance of a lava flow can be explained by the Newtonian viscosity of the lava or the yield strength of either its crust or its interior, depending on the relative rate of flow advance compared to the rate of flow cooling (Griffiths & Fink, 1997). Thus the advance rate of an active flow can be used to constrain physical parameters controlling emplacement. Flow advance also controls flow morphology and can vary depending on effusion rate, viscosity, and the slope of the underlying terrain (e.g., Lyman et al., 2004). Lyman et al. (2004) demonstrated that as the advance rate of a flow increases relative to its cooling rate, the flow will become more elongate and uniform and less likely to develop multiple flow lobes. Fink & Griffiths (1998) investigated the morphology of 20th century lava dome eruptions and showed that silicic lava domes can have a variety of forms, and that the morphology can change during prolonged eruptions.

Castruccio et al. (2013) used flow advance rate observed during eruptions and three simplified models of lava flow advance to identify the dominant mechanism

controlling flow advance. In general, while basaltic flows were controlled either by the lava's internal viscosity or the yield strength of the crust depending on effusion rate and eruption duration, data from more silicic flows in 1999-2000 at Santiaguito Volcano in Guatemala and in 1998-1999 at Colima Volcano in Mexico suggest that emplacement of these flows were controlled by the yield strength of their interiors (Castruccio et al., 2013). However, additional implications of Castruccio et al. (2013) suggest that the controlling factor can transition between mechanisms based on variations in effusion rate during an eruption. Estimates of yield strength by Castruccio et al. (2013) show a roughly two orders of magnitude difference between basaltic and andesitic flows for both the crust (10^4 vs. 10^6 Pa) and the flow interior (10^3 vs. 10^5 Pa).

Previous work on active viscous flows at Cordón Caulle Volcano in Chile and Santiaguito have shown that despite a many orders of magnitude difference in viscosity, these flows behave similarly and can have similar properties and appearance to basaltic flows, albeit on different spatial and temporal scales. Harris et al. (2002; 2004) describe a dacite flow at Santiaguito with well-developed levees that was able to travel nearly 4 km from the vent despite effusion rates < 1 $m^3 s^{-1}$ and exhibited "caterpillar-track-type" flow advance at the front, a process shared with basaltic 'a'ā flows. Tuffen et al. (2013) observed breakout lobes reminiscent of compound basaltic flows at the Cordón Caulle rhyolite flow in Chile.

6.2. Methods

6.2.1. Satellite Images

Both visual and thermal satellite images provide means to document the emplacement of the Sinabung lava flow. I use sequential visual daytime images (submeter resolution) from Google Earth™ to measure the length and surface area of the flow. Thermal images are from the Advanced Spaceborne Thermal Emission and Reflection Radiometer (ASTER) and the Moderate Resolution Imaging Spectroradiomter (MODIS) instruments on the Aqua (MODIS) and Terra (ASTER and MODIS) satellites, which are a part of NASA's Earth Observing System program. In the thermal bands, ASTER scenes have a resolution of 90 meters with a 1-2 week repeat interval and MODIS scenes have a 1 km pixel size and a 12-hour repeat interval.

I selected MODIS scenes for this work from the set of Level 1B nighttime images of Northern Sumatra captured between August 1, 2013 and April 30, 2016. Each scene was manually inspected for minimal cloud cover before being downloaded from NASA's ladsweb archive (https://ladsweb.nascom.nasa.gov/). I use the MODIS Conversion Toolkit, a free plug-in available for the ENVI software (Exelis Visual Information Services), to georeference each MODIS scene and correct for the bow-tie effect (Coppola et al., 2012; Chapter 2, this dissertation). I correct for atmospheric effects by subtraction of a representative background region near Sinabung as in Coppola et al. (2012) and Chapter 2 of this dissertation. A total of 653 scenes are used in this study.

I estimate the time-averaged effusion rate (E) at Sinabung following the methods of Harris et al. (1997) and Harris & Ripepe (2007) where

$$E = \frac{Q_{total}}{\rho\left(C_p \Delta T + L\varphi\right)} \tag{6.1}$$

and Q_{total} is the sum of the radiative (Q_{rad}) and convective (Q_{conv}) components of heat flow away from the lava flow surface

$$Q_{total} = Q_{rad} + Q_{conv} = A\varepsilon\sigma T_h^4 + Ah_c\left(T_{surf} - T_{air}\right) \tag{6.2}$$

I use values for emissivity (ε = 0.98 for andesite), specific heat capacity (C_p = 1150 J kg^{-1} K^{-1}), post-eruptive cooling of the lava (ΔT = 200–350 °C), latent heat of crystallization (L = 3.5 x 10^5 J kg^{-1}), and post-eruptive crystallization (φ = 0.45) as in Harris & Ripepe (2007). I choose density (ρ = 2500 kg m^{-3}), lava surface temperature (T_{surf} = 50–110 °C), and average air temperature (T_{air} = 20 °C) based on observations and best estimates for Sinabung (Harris et al., 2002; http://en.climate-data.org/). I correct both C_p and ρ for 20% vesicularity (Harris & Ripepe, 2007). The Stefan-Boltzmann constant (σ) is 5.67 x 10^{-8} W m^{-2} K^{-4} and the convective heat transfer coefficient for an active lava flow (h_c) is ~50 W m^{-2} K^{-1}. The surface area of the lava flow (A) is found by summing the pixel fractions occupied by a hot source (at temperature T_{surf}) for every pixel within a defined region around the active lava flow and multiplying by the pixel area (1 km^2 for MODIS). The pixel fraction is determined by a two-component temperature model as in eq. 1 of Harris & Ripepe (2007). This method assumes the area of the flow is cooling-limited and the flow is in a thermal steady-state (Harris & Baloga, 2009), resulting in flow area being proportional to effusion rate such that E represents the average effusion rate for a period of the eruption including the time of image acquisition (Wright et al., 2001). Multiple previous studies have shown these assumptions to be valid for first-order estimates of

effusion rate through comparison to effusion rates derived by other methods (e.g. Harris et al., 1997; Harris et al, 2007; Chapter 5, this dissertation).

I used the ASTER Surface Kinetic Temperature higher-level data product (AST08) and selected both daytime and nighttime ASTER scenes through NASA's Reverb system (http://reverb.echo.nasa.gov/reverb/). The surface temperature for each pixel is derived from the radiance observed by ASTER thermal bands (Bands 10-14, wavelength λ = 8.1-11.3 μm) after correcting for atmospheric effects using the thermal emissivity separation algorithm developed by Gillespie et al. (1998). I estimated the surface temperature of the lava flow by taking the average of the pixels I identify as part of the flow. I corrected daytime images for the solar heating component of the surface temperature by subtracting the surface temperature of a background region near Sinabung from the average surface temperature of the lava flow.

Following Oppenheimer (1991) and Harris et al. (2002), I use the heat conduction equation to estimate the thickness of the lava flow crust. Assuming a steady-state where the thermal conductivity of the flow crust (k), temperature of the flow core (T_{core}), and temperature of the flow surface (T_{surf}) are constant in time, the crust thickness (δ) is

$$\delta = \frac{k\left(T_{core} - T_{surf}\right)}{\vec{q}_{cond}} \tag{6.3}$$

where $\vec{q}_{cond}$ is the conductive heat flux in W/m^2. I use k = 2.5 W m^{-1} K^{-1} (Oppenheimer 1991; Harris et al., 2002; Giberti et al., 1992) and T_{core} = 850 °C following temperatures of similar eruptions at Santiaguito (Harris et al., 2002) and Soufrière Hills Volcano, Montserrat (Barclay et al., 1998). I assume that all heat conducted to the flow surface is lost via radiation and convection so that $\vec{q}_{cond} = (Q_{rad} + Q_{conv})/A$ and eq. 6.3 can be

solved independently of flow area using T_{surf} values from individual ASTER images. I also use ASTER data to provide values for T_{surf} in eq. 6.2, where I use a range of T_{surf} = 50-110 °C based on the average and maximum observed temperatures of the flow surface from multiple ASTER images in January and February 2014.

6.2.2. Flow Models

I use flow lengths measured on visual satellite images in Google Earth™ and observations from the Sinabung Volcano Observatory (Global Volcanism Program, 2014a; 2014b) to apply the flow models presented in Castruccio et al. (2013). Castruccio et al. (2013) assume a laminar flow on a slope where flow advance is driven by gravity and resisted by forces under three different scenarios: 1) the Newtonian viscosity of the flow; 2) the yield strength of the flow core; 3) the yield strength of a cooled flow crust. Each resisting force acts on the surface area of the base of the flow (assumed to be simply flow length times width). Setting the driving and resisting forces equal to each other and solving for the flow length (L) gives

$$L = \sum_{i=1}^{n} \left(\frac{V_i^2 \rho g t_i \sin \beta_i}{\mu_i W_i^2} \right)^{\frac{1}{3}} \tag{6.4}$$

for the Newtonian case (from eq. 12, Castruccio et al., 2013).

$$L = \sum_{i=1}^{n} \left(\frac{V_i \rho g \sin \beta_i}{\sigma_{yi} W_i} \right) \tag{6.5}$$

for the yield strength of the core case (from eq. 15, Castruccio et al., 2013), and

$$L = \sum_{i=1}^{n} \left(\frac{V_i^2 \rho g \sin \beta_i}{\sigma_{ci} W_i^2 \delta} \right)^{\frac{1}{2}} \tag{6.6}$$

for the yield strength of the flow crust case (from eq. 19, Castruccio et al., 2013), where g is gravitational acceleration, i represents a time step of flow advance and t_i is the duration of that time step, V_i is the volume added in each time step, β_i and W_i are the slope and flow width at the flow front at each time step, and μ_i, σ_{yi}, and σ_{ci} are the viscosity, core yield strength, and crust yield strength of the lava at each time step. In eq. 6.6 the crust thickness is assumed to be increasing by conductive cooling such that

$$\delta \sim \sqrt{\kappa t} \tag{6.7}$$

where κ is the thermal diffusivity (~10^{-6} m^2 s^{-1}) and t is the duration of the eruption (Castruccio et al., 2013). The summation form presented here and in Castruccio et al. (2013) allows for each of the variables to change during flow advance in order to match observations and produce a better fit for the unknown variables.

I choose a time step of 10^5 seconds. I scale flow width to progressively increase by $W_i = 1.005 \cdot W_{i-1}$ from an initial value of 400 meters to a final value of 1050 meters to match satellite observations. Basal topographic slope (β) is calculated using a 5-meter pre-eruption (2010) DEM of Sinabung provided by the Badan Informasi Geospasial and the Center for Volcanology and Geological Hazard Management (CVGHM) in Indonesia. I use $\beta = 0.6$ (31°) for $L < 1110$ meters and $\beta = 0.25$ (14°) for $L > 1110$ meters. The volume added is determined by two different methods, one assuming a constant eruption rate of 4.5 m^3 s^{-1} (Chapter 5, this dissertation) and the other assuming a rate of 7.0 m^3 s^{-1} for the first 81 days of the eruption (24 December 2013 to 15 March 2014), and 3.0 m^3 s^{-1} after that, based on results presented in the following section. I determined best-fit values for μ, σ_y, and σ_c by solving eqs.check 6.4-6.6 for a range of possible values and

minimizing the misfit of the flow length calculated by the model to the observed flow lengths.

6.3. Results

6.3.1 Flow growth

A combination of satellite images (Figure 6.1), observations from the Sinabung Volcano Observatory (Global Volcanism Program, 2014a; 2014b), and ground-based photogrammetry (Chapter 5, this dissertation) show the advance of the Sinabung lava flow over the course of the eruption (Figure 6.2). From the onset of the effusive eruption on 24 December 2013 to 13 March 2014, the advance rate of the flow front averaged 30 m d^{-1}. Flow advance rate decreased significantly, to an average of 4.3 m d^{-1}, between 13 March and 13 June, and 1.1 m d^{-1} between 13 June and 22 September. Following the first major lava collapse and breakout event in October 2014, flow advance slowed further to less than 0.5 m d^{-1} through the end of 2014. By early 2015, flow advance stopped altogether (Figure 6.1) as newly erupted lava fed into the breakout lobes rather than into the initial flow. Figure 6.2 also shows that the slope of the topography underlying the flow is relatively constant for the flow front locations in March-September 2014. This suggests that the decreases in flow advance rate I observe are not caused by slope effects and may be due to changes in effusion rate.

Thermal images show that the style of flow advance varies with the flow advance rate. Rapid flow advance was uniform (e.g., February 2014), as seen in an ASTER image from February 26 (Figure 6.2a, arrow) in which the flow front appears as an elongate hot spot. As flow advance slowed, parts of the flow front cooled. A 22 September 2014

ASTER image shows two separate hot spots along the front (Figure 6.2b, arrows), suggesting advance was occurring in more isolated breakout lobes.

Satellite images on 9 and 26 February 2014 show the surface area of the flow was 0.50 x 10^6 m^2 and 0.77 x 10^6 m^2, respectively - an increase of 0.17 x 10^6 m^2 over 17 days. I estimate a flow thickness of ~40 m at that time based on images from the Sinabung web camera from February (Figure 6.1). Using this thickness and the surface area, I estimate the flow volume at each date and calculate an average effusion rate of 7.5 m^3 s^{-1} for this 17-day period. If instead I estimate the flow thickness using the average effusion rate of 4.4 m^3 s^{-1} calculated in Chapter 5 of this dissertation using topographic differencing for the period from 24 December 2013 to 22 September 2014, I find the result of a ~24 m flow thickness to be too low to agree with visual observations. Thus I favor an elevated effusion rate during February 2014. If I again assume a 40 m thickness for the lava, the average eruption rate between when effusion began on 24 December 2013 and the satellite image on 9 February 2014 is 5.6 m^3 s^{-1}.

I use both eqs. 6.3 and 6.7 to estimate the thickness of the flow crust throughout the eruption (Figure 6.3). Six ASTER images show that average flow surface temperatures decreased from 50-60 °C in January-February 2014 to 25 °C by June-September 2014. The crust thicknesses calculated from the ASTER surface temperatures (dots, Figure 6.3) generally agree with the model of crust growth by conductive cooling (line, Figure 6.3) used by Castruccio et al. (2013) and validate the use of eq. 6.7 for approximating crust thickness. Both eqs. 6.3 and 6.7 suggest that crust thickness increased from 1-2 m in Jan-March 2014 to 4 m by mid-2014 and 5 m by the time the flow stopped advancing in late 2014-early 2015.

6.3.2 Eruption phases

The maximum Band 21 (central $\lambda = 3.959$ μm) pixel radiance from a MODIS scene over Sinabung is a good proxy for intensity of the eruption (Figure 6.4) and allows me to identify four main phases of eruptive activity at Sinabung (Table 6.1). The flow emplacement phase (24 December 2013 to 31 March 2014) is characterized by frequent high-radiance pixels, as both effusion and flow advance rates were relatively high and the flow crust was relatively thin, resulting in high surface temperatures easily observed by MODIS. Over 80% of the lava flow's final 2.95 km length was emplaced during this phase. I detect nearly no MODIS thermal anomaly during the flow inflation phase (1 April to 30 September 2014). Lava collapse-generated PDC activity also significantly decreased during this phase (Global Volcanism Program, 2014b), which limited the exposure of the hot interior of the flow that could be detected by MODIS. Despite the lack of a thermal anomaly and lower flow advance rates, lava effusion continued at a moderate rate such that the majority of the flow's final volume of 1.0×10^8 m^3 (Chapter 5, this dissertation) was emplaced during this phase.

The first phase of lava collapse and breakout began in early October (Breakout 1, Figure 6.4) when the flow inflated to the point where it overtopped a confining ridgeline and became gravitationally unstable (Chapter 5, this dissertation). Growth of a new lava lobe and frequent PDCs resulted in many thermal anomalies in MODIS scenes (Figure 6.4). The first collapse and breakout phase ended in late April 2015, and was followed by a month of quiet before the second collapse and breakout phase began on 1 June 2015 (Breakout 2, Figure 6.4), which renewed PDC activity. This phase of the eruption is ongoing as of this writing (July 2016) and consists of continued lava effusion, occasional

small explosions, and daily collapse of the lava lobes generating PDCs, one of which caused 7 fatalities on 21 May 2016 (Global Volcanism Program, 2016).

Time-average effusion rates derived from MODIS images using eqs. 6.1 and 6.2 show that the highest rates occurred during the emplacement phase (Figure 6.5), with less frequent high rates also occurring during the two breakout phases. The lowest average effusion rate occurred during the inflation phase. Individual MODIS images using ΔT = 200 °C and T_{surf} = 110 °C have maximum effusion rates approaching 10 m^3 s^{-1} in January-March 2014 and ~6 m^3 s^{-1} during the two breakout phases (dots, Figure 6.5), consistent with effusion rates calculated based on the surface area of the flow and estimates of flow thickness.

I calculate a total volume of extruded magma of 0.7 x 10^8 m^3 at the end of the inflation phase from the MODIS extrusion rate data. This volume and the average effusion rates (red lines, Figure 6.5) for the emplacement (3.4 m^3 s^{-1}) and inflation (1.2 m^3 s^{-1}) phases are less than the values of 1.0 x 10^8 m^3 and 4.4 m^3 s^{-1} found through photogrammetric modeling and topographic differencing (Chapter 5, this dissertation). I attribute this discrepancy to a combination of insulation by the flow crust and frequently cloudy weather that reduced the ability of satellite thermal images to detect an effusive eruption. In other words, MODIS-derived extrusion rates are underestimates (or unreliable) when emplacement is dominated by inflation into a cooling, intact crust. Effusion rates estimated from MODIS images after September 2014 are likely more representative of the actual rates as lava was no longer being extruded into the insulated flow and was instead flowing onto the surface in the new lava lobes on the upper flank (Global Volcanism Program, 2014; 2015a). Average discharge rates for the two breakout

phases are approximately 1-2 m^3 s^{-1}. I further estimate that an additional 0.5-1.0 x 10^8 m^3 of lava has been extruded at Sinabung since the 22 September 2014 measurement from Chapter 5 of this dissertation and that the total volume of magma erupted during the entire Sinabung eruption as of July 2016 is nearly 2 x 10^8 m^3 (0.2 km^3).

6.3.3. Flow advance modeling

I applied each of the flow advance models of Castruccio et al. (2013) (eqs. 6.4-6.6) to the observed flow lengths during emplacement of the Sinabung lava flow (Figure 6.6). The Newtonian model (eq. 6.4) is able to fit only the first 6 data points (24 December 2013 to 13 March 2014), and I find a best fit of the model to those six data points with a viscosity μ = 1.5 x 10^{10} Pa·s (blue dashed line, Figure 6.6). When I use a constant eruption rate of 4.5 m^3 s^{-1} (Chapter 5, this dissertation) the crust-controlled model (eq. 6.5) is able to fit the first seven data points (through 6 April 2014) with a crust yield strength σ_c = 5.0 x 10^6 Pa (red dashed line, Figure 6.6). Neither model alone is able to account for the decrease in flow advance rate that occurred in March 2014 (Figure 6.2). I improved the fit by combining the crust-controlled model with the core-controlled model (eq. 6.6), with the transition between the two models occurring in late March 2014. The best fit for this model (purple dashed line, Figure 6.6) uses the same crust yield strength as the red-dashed line and a core yield strength σ_y = 1.0 x 10^6 Pa.

The best overall fit of any variation of the flow models to the observations occurs when I use a variable effusion rate. Based on the data presented above (Figure 6.5), I chose an initial effusion rate of 7.0 m^3 s^{-1} decreasing to 3.0 m^3 s^{-1} on 15 March 2014. Applying this with the crust-controlled model fits the first eight data points (through 13

June 2014) with σ_c = 1.1 x 10^7 Pa and can account for the initial decrease in flow advance rate (yellow line, Figure 6.6). Combining this model with a transition from crust-controlled to core-controlled models in June 2014 results in a decreasing flow advance rate in the later half of 2014, matching well the observational data (green line, Figure 6.6). This model (green line, Figure 6.6) results in the best overall fit to the data when σ_y = 1.5 x 10^6 Pa. In 2015, this model deviates from the data as the flow stopped advancing due to the first lava collapse and breakout event on the upper flanks that began in October 2014 (Global Volcanism Program, 2014b; 2015a).

Given the better fit of the model when I include a decrease in effusion rate in mid-March 2014, I favor a change in effusion rate as the cause of the decrease in flow advance rate in March (Figure 6.2) as opposed to a change in the controlling mechanism of flow emplacement or the underlying topographic slope. I attribute further but subtler decrease in average advance rate in June 2014 to the transition between flow advance being controlled by the yield strength of the crust to the yield strength of the core. Crust-controlled flow advance is also correlated to uniform advance of the flow front, while core-controlled advance is dominated by breakout lobes along the flow front (lobes discussed in Chapter 5 of this dissertation).

6.4. Discussion

This study supports and advances previous work on the Sinabung eruption and other viscous lava flows. In Chapter 5 of this dissertation I used ground-based photogrammetry and topographic differencing to find that during a field campaign in September 2014, flow advance at the front was located at two separate breakout lobes

with an advance rate of 3-11 m d^{-1}. This observation was supported by ground-based thermal images showing thermal anomalies in these same locations, and is further confirmed by the 22 September 2014 ASTER image (Figure 6.2b) that also shows regions of relatively high temperature in the breakout lobe regions identified in Chapter 5 of this dissertation. Breakout lobes along the flow margins were also observed in the later stages of the 2011-2012 rhyolite eruption of Cordón Caulle (Tuffen et al., 2013). The Cordón Caulle advance rate of the lobes was a few meters per day while the average advance rate of the flow front was ~1 m d^{-1} (Tuffen et al., 2013), similar to rates I observe at Sinabung (Figure 6.2).

My measurements of flow advance rate, crust thickness, and flow surface temperature are similar to observations from the lava flows at Santiaguito. Harris et al. (2002) reported a flow advance rate of 12.5 m d^{-1}, similar to the average rate at Sinabung for the first 8 months of the eruption. Santiaguito flow surface temperatures were 40-111 °C compared to 50-110 °C at Sinabung that I observe in ASTER images from January and February 2014. Harris et al. (2002) also use eq. 6.3 to estimate crust thicknesses of 1.9-3.4 m at Santiaguito, compared to my estimates of crust thickness at Sinabung increasing from 1 to 5 meters during 2014. Harris et al. (2002) noted that thickening crust insulated the flow at Santiaguito, which I also observe at Sinabung and limits the use of thermal data for observing activity, especially during the inflation phase (Figure 6.4). The lack of thermal anomalies and the significant underestimation of effusion rate from MODIS images in April-September 2014 (Figure 6.4, Figure 6.5), despite continued effusion, is a result of insulation from the thickening crust.

My results suggest a decreasing effusion rate as the eruption progressed. Wessels & Griswold (2014) used radar images of Sinabung to observe effusion rates as high as 20 $m^3 s^{-1}$ in early 2014 and report an average effusion rate of 6 $m^3 s^{-1}$ for January-August 2014, similar magnitudes to both the maximum observed effusion rates from MODIS images (10 $m^3 s^{-1}$) and the long-term average from Chapter 5 of this dissertation (4.4 $m^3 s^{-1}$) (Figure 6.5). Nakada et al. (2014) report an average eruption rate of 5 $m^3 s^{-1}$ and a total volume of erupted magma of 0.1 km^3 as of summer 2014, also in agreement with my results in this dissertation. A decreasing trend in effusion rate is typical of long-lived effusive eruptions (e.g., Wolpert et al., 2016). Furthermore, Bayesian statistical models developed by Wolpert et al. (2016) from multiple historical effusive eruptions of viscous lava gives a 50% probability that the Sinabung eruption will continue until 2019. This prediction suggests that the eventual total volume of extruded magma for the Sinabung eruption may reach 0.3-0.5 km^3, based on my current volume estimate of 0.15-0.2 km^3 and assuming an average effusion rate of 1-2 $m^3 s^{-1}$ from my MODIS estimates.

My estimates for the yield strengths of the crust ($\sigma_c = 1.1 \times 10^7$ Pa) and core ($\sigma_y = 1.5 \times 10^6$ Pa) (Figure 6.6) of the Sinabung lava flow are an order of magnitude greater than the yield strengths found by Castruccio et al. (2013) for flows of similar composition at Santiaguito and Colima, as well as yield strengths estimated for silicic flows in general by Fink & Griffiths (1998) and Lyman et al. (2004). I attribute these differences to the flow at Sinabung being less insulated than the Santiaguito and Colima flows, allowing the core to cool more quickly and the yield strength to increase as a result. This condition may in part be caused by the lack of a flow channel and corresponding insulating channel walls at Sinabung (as were observed at Santiaguito, Harris et al., 2002). The absence of a

channel also allowed the flow at Sinabung to spread laterally to 1 km in width at the flow front. The spreading decreases the flow advance rate compared to a channelized flow where flow growth is directed only downslope. The spreading at the flow front also affects the validity of applying of eqs. 6.4-6.6, which assume a rectangular flow geometry in map view. The lava flows at Santiaguito (Harris et al., 2002; 2004), Colima (Navarro-Ochoa et al., 2002), and Cordón Caulle (Tuffen et al., 2013) were also more mobile, with final lengths of 3.5 and 4.0 km, and thinner than the Sinabung lava flow. This comparison further supports the idea that the Sinabung lava flow cooled more rapidly than the other silicic flows discussed here, leading to higher yield strengths, decreased flow advance rates, and flow inflation.

Castruccio et al. (2013) find a best fit of their models to the flow advance data for Santiaguito and Colima using only eq. 6.6 for flow advance controlled by the yield strength of the flow interior. On the other hand, I use a combination of crust- and core-controlled advance to best fit the Sinabung data. Effusion rates during the first three months of the Sinabung eruption were higher than those at Santiaguito (~0.5 m^3 s^{-1}, Harris et al., 2004) and Colima (4.4 m^3 s^{-1}, Navorro-Ochoa et al., 2002). Crust-controlled advance and high effusion rates early in the Sinabung eruption agree with the experimental results of Lyman et al. (2004) which show that higher effusion rates favor crust-controlled flow advance. The observed correlation between higher effusion rate and higher PDC frequency (Calder et al., 2002; Nakada et al., 1999; Chapter 2, this dissertation) may then imply that lava collapse-generated PDCs are more common when flow advance is crust-controlled. This correlation is consistent with observations at Sinabung where PDCs where most frequent in January-March 2014. Alternatively, this

trend may be the result of slope steepness, as lava collapse-generated PDCs are more likely when slope is steeper (Harris et al., 2002) and crust-controlled flow advance is also more likely on steeper slopes (Lyman et al., 2004).

Both Harris et al. (2002; 2004) and Tuffen et al. (2013) describe viscous lava flows with lengths of a few kilometers that resemble basaltic flows in both flow advance mechanisms and morphology. The Sinabung lava flow does not show the same mobility as these flows, however, it does share characteristics more commonly associated with inflated basaltic flows. The primary example occurs during the later months of flow emplacement in 2014. When advance rate slowed, flow advance began to occur via individual breakout lobes and a majority of the volume erupted was accommodated by flow inflation rather than further advance of the flow front. The observation of similar processes at lava flows of both basaltic and silicic composition suggests that flow emplacement occurs via common mechanisms regardless of lava type. The general observation noted by Tuffen et al. (2013) that silicic lava flows are shorter, thicker, and slower than basaltic flows is thus solely a result of variable flow rheology and is not related to different emplacement processes.

The results of this study allow me to describe the emplacement of the Sinabung lava flow in detail (Table 6.1, Figure 6.7). The effusive eruption began in late December 2014 and the lava flow advanced at a rate of 20-40 m d^{-1} (Figure 6.2) as effusion rates fluctuated between 5-10 m^3 s^{-1} (Figure 6.5). Flow advance rate decreased from late March through early June as the effusion rate decreased to ~3 m^3 s^{-1} (Figure 6.5) in late March and the crust thickened to 4 m by June (Figure 6.3). During this period flow advance was controlled by the yield strength of the thickening crust (Figures 6.7a &

6.7b). As flow advance slowed, the style of advance changed from uniform along the front (Figure 6.2a) to isolated breakout lobes (Figure 6.2b, Figure 6.7c). In mid-June the flow transitioned from crust-controlled to core-controlled as flow advance rate decreased further (Figure 6.2) and the flow inflated to accommodate the increasing volume from continuing effusion (Figure 6.7d). Flow advance remained controlled by the yield strength of the flow interior until the flow stopped advancing in late 2014-early 2015. Inflation of the flow caused the lava to overtop ridges that had originally confined the flow to a valley on the upper flanks of the volcano (Chapter 5, this dissertation). This overtopping led to large gravitational instabilities in the flow that collapsed in October 2014 and June 2015 (Figure 6.7e). New lava lobes grew out of these collapses, cutting off the flow of fresh magma feeding the original flow lobe. As of this writing, a relatively low effusion rate of ~1 m^3 s^{-1} (Figure 6.5) continues to feed these new lobes, which frequently collapse and generate PDCs (Global Volcanism Program, 2016).

6.5. Conclusions

I document in detail the 2014-2016 emplacement of a 2.9 km long lava flow and two small summit breakout lava lobes at Sinabung volcano. The main flow was active from December 2013 to late 2014-early 2015 before multiple collapses of the upper flow redirected fresh magma into the new lava lobes near the vent (Global Volcanism Program, 2015a). More than 80% of the flow's current length of 2.95 km was emplaced in January-March 2014, during which time flow advance rates were > 20 m d^{-1} and the average effusion rate was ~7 m^3 s^{-1}. A decrease in flow advance rate in late March was a result of a decrease in effusion rate to ~3 m^3 s^{-1}. From December 2013 to June 2014, flow

advance was controlled by the yield strength of a growing flow crust with yield strength $\sigma_c = 1.1 \times 10^7$ Pa. Further decrease of the flow advance rate in June 2014 was a result of flow advance transitioning to being controlled by the yield strength of the flow's core, $\sigma_y = 1.5 \times 10^6$ Pa. The decreasing flow advance rate also caused the flow to inflate to accommodate new lava from continued effusion. Flow advance during the middle and later parts of 2014, when advance was core-controlled, was characterized by individual breakout lobes along the flow front in contrast to uniform flow advance observed when advance was crust-controlled and effusion rates were higher.

These processes are similar to those observed at other viscous lava flows such as those at Santiaguito Volcano, Colima Volcano, and Cordón Caulle Volcano, and like those eruptions, also show similarities to processes of flow emplacement observed at basaltic eruptions, despite estimated yield strengths at Sinabung that are three orders of magnitude greater than typical values for basalt and one order of magnitude greater than other silicic eruptions at Santiaguito and Colima (Castruccio et al, 2013). This study provides a remote sensing-based workflow of documenting lava flow emplacement during ongoing eruptions that can be used to better understand lava flow processes and associated hazards at other current and future effusive eruptions, regardless of lava composition.

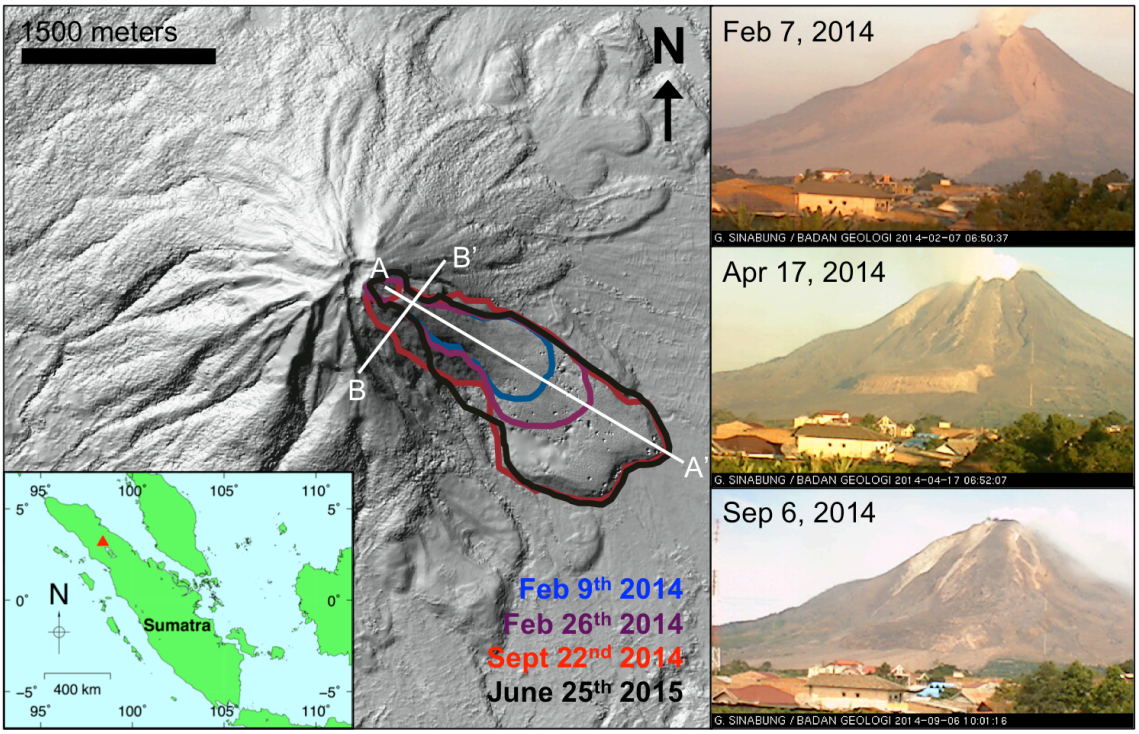

Figure 6.1. Location map of Sinabung Volcano, North Sumatra, Indonesia. Sinabung is the red triangle in the inset image. Colored outlines show the location of the lava flow as it advanced. Photos on the right are from the Sinabung Observatory web camera and show the flow increasing in length and thickness with time. Base image is a 5 m pre-eruption DEM combined with the DEM of the lava flow on September 22, 2014 from Chapter 5. Line A-A' is the profile shown in Figure 6.2 and Figure 6.7a-d. Line B-B' is the profile shown in Figure 6.7e.

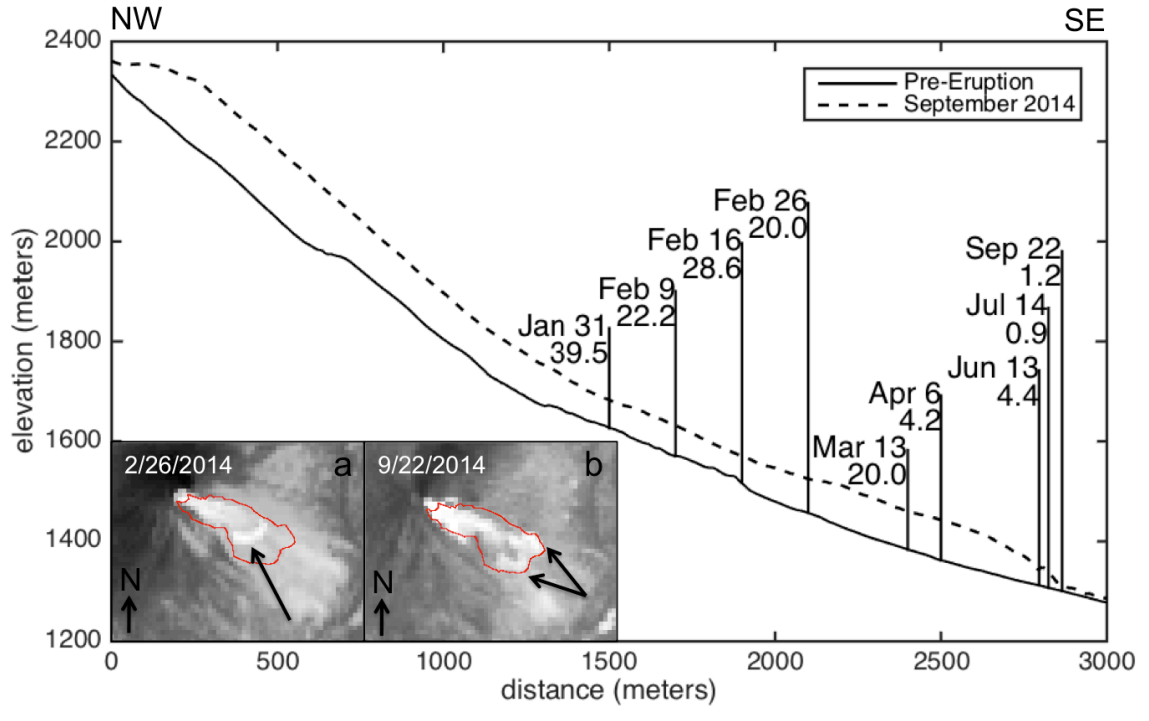

Figure 6.2. Flow advance of the 2014 Sinabung lava flow. The length of the lava flow at different times is shown on a topographic profile along the axis of the flow (line A-A', Figure 6.1). The solid line is the pre-eruption surface and the dashed line is the lava flow surface from a DEM created using ground-based photogrammetry in September 2014 (Chapter 5, this dissertation). Labels are the date of the flow length measurement and the flow advance rate in the interval prior to that date. Flow advance slowed significantly between March 13 and April 6 and again between June 13 and July 14. Thermal anomalies in ASTER images along the flow front show the style of flow advance changed from uniform along the flow front (arrow, A) to isolated in breakout regions along the front (arrows, B). Red outline in A and B is the flow extent on September 22nd, 2014 from Chapter 5 of this dissertation.

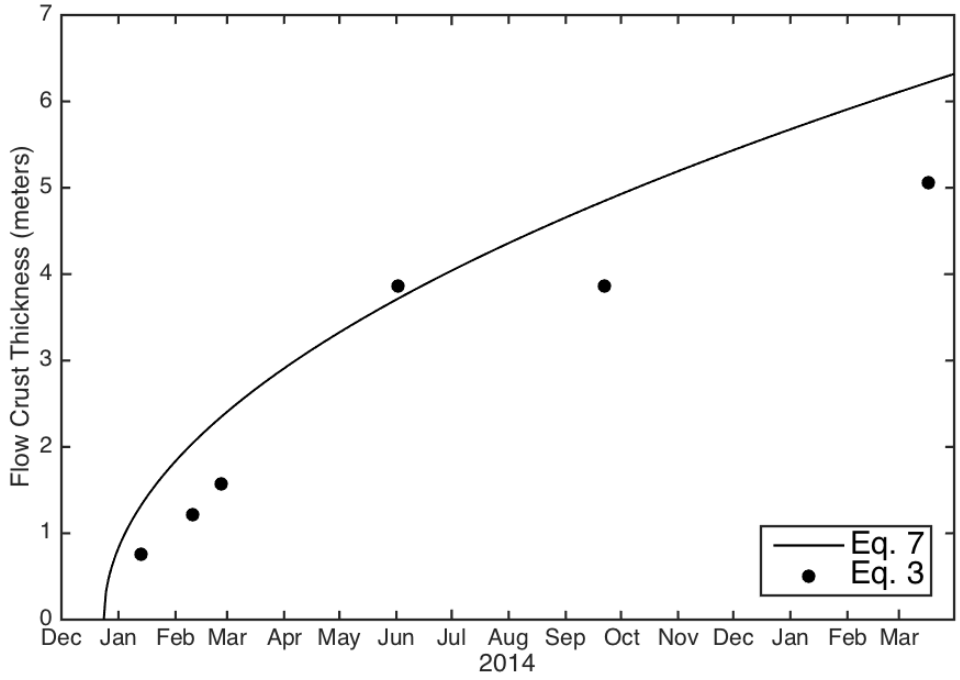

Figure 6.3. Estimated thickness of lava flow crust. I estimated the thickness of the lava flow crust by two different methods. Points are thicknesses calculated from ASTER-derived flow surface temperatures using eq. 6.3. Solid line is from assuming constant conductive cooling as in eq. 6.7. Both methods produce similar thickness estimates and similar trends.

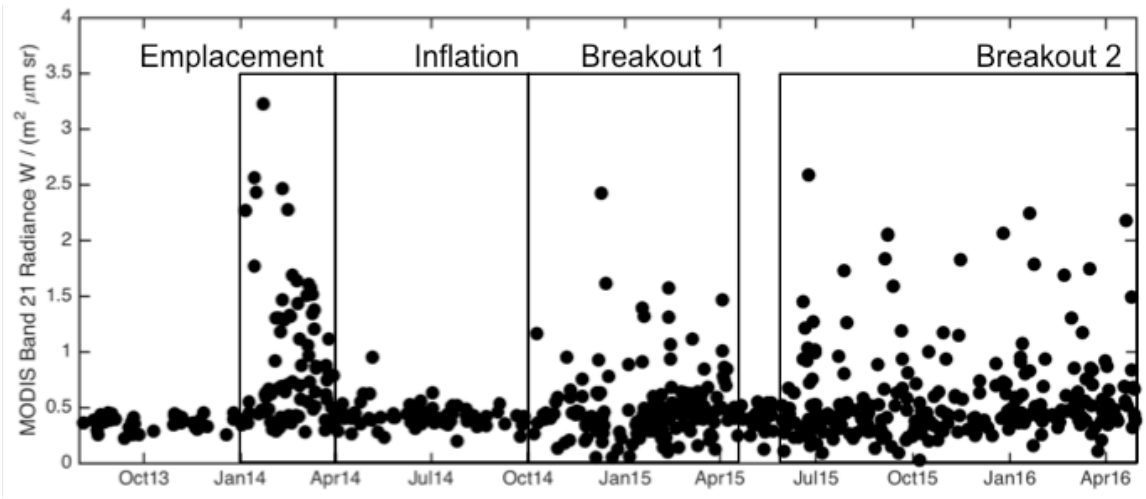

Figure 6.4. Radiance of the Sinabung lava flow from MODIS imagery. The maximum MODIS Band 21 radiance over Sinabung shows variable intensity and identifies 4 phases of the Sinabung eruption (black boxes, see text and Table 6.1 for details of each phase).

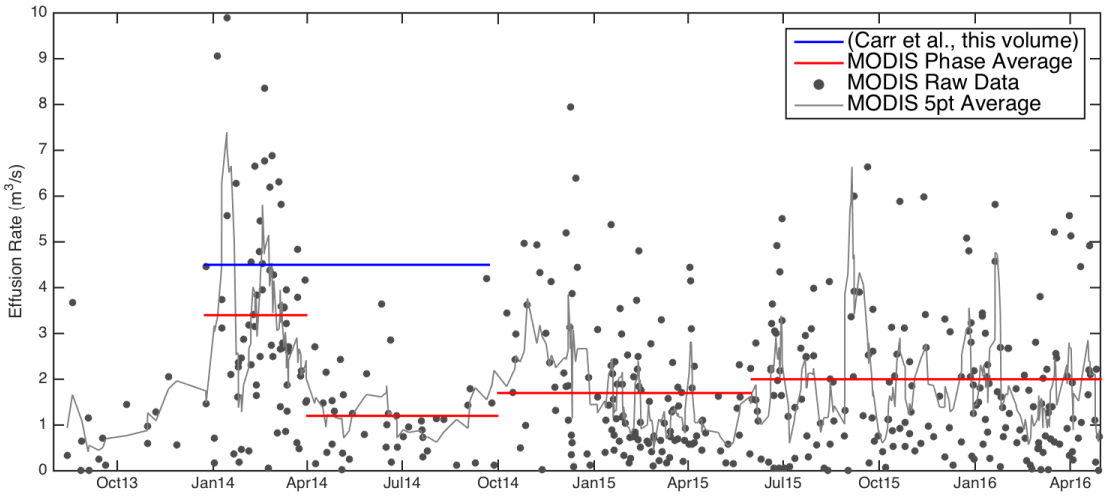

Figure 6.5. Effusion rates of the Sinabung lava flow. Multiple methods were used to estimate the effusion rate at Sinabung. Horizontal lines are long-term averages from photogrammetry (blue, Chapter 5 of this dissertation) and averages of each phase derived from MODIS data using T_{surf} = 110 °C (red) for the flow surface temperature. Black dots are raw data and the line is a 5-point running average of the time-averaged effusion rates for each MODIS image corresponding to T_{surf} = 110 °C.

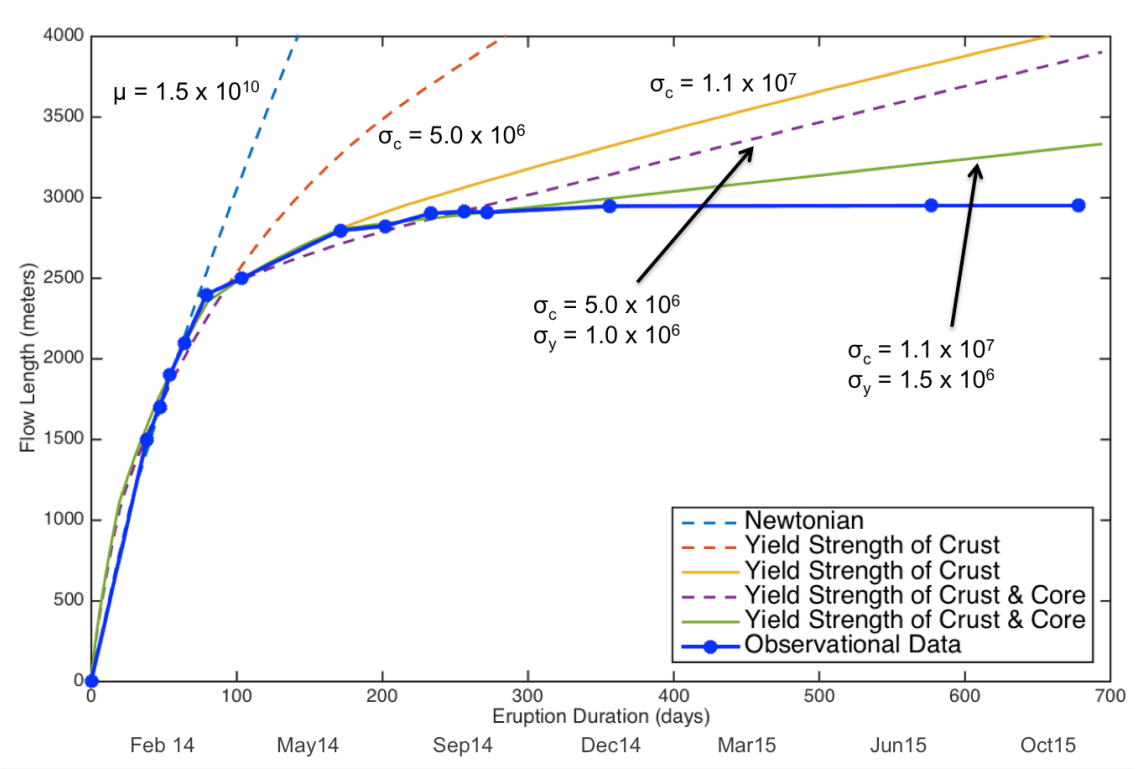

Figure 6.6. Modeling of the Sinabung lava flow advance. I applied models for lava flow advance as in Castruccio et al. (2013) to determine the mechanism controlling flow advance. Blue line and points are observational data from the Sinabung Observatory (GVP, 2014a; 2014b), satellite images, and photogrammetry (Chapter 5, this dissertation). Curves show the best fit to the observations for each model type. Dashed lines are models with a constant effusion rate and solid lines are models with a variable effusion rate (see text for details). Newtonian viscosity (μ) units are Pa-s and units for yield strength of the crust (σ_c) and core (σ_y) are Pa. The model with the best overall fit to the data is a crust- and core-controlled model with a transition between controls in mid-June 2014 (green line). This line deviates from the observations in late 2014 (~day 350), when erupting lava stopped feeding the main flow (eruption day 300-350).

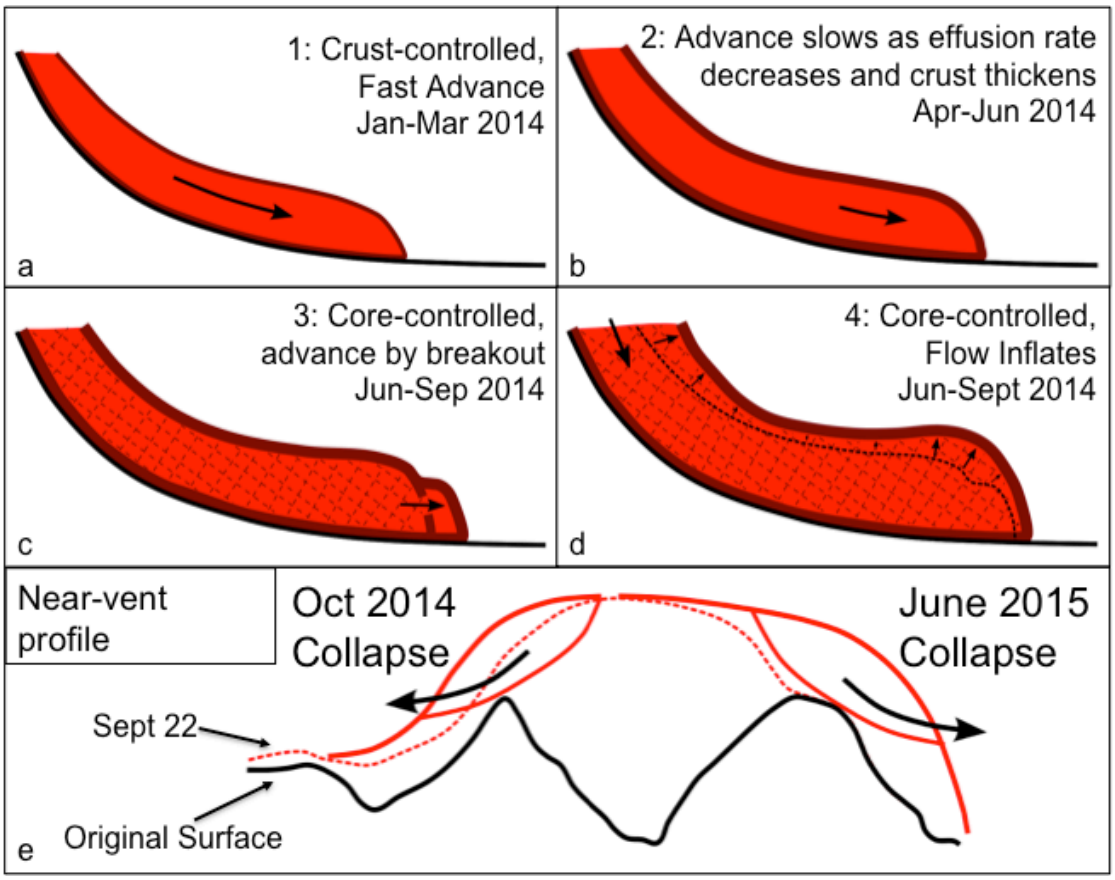

Figure 6.7. Conceptual model of the emplacement of the Sinabung lava flow.

Cartoons show the lava flow in cross-section along line A-A' (a – d) or B-B' (e) from Figure 6.1. Flow advance was initially controlled by the yield strength of the flow crust from January through June 2014 (a). A decrease in effusion rate in March 2014 and the thickening flow crust led to lower flow advance rates in April-June 2014 (b). In July 2014 the controlling mechanism switched from the yield strength of the crust to the yield strength of the core and the flow stopped advancing uniformly and began advancing in isolated breakouts (c). During this time the flow also inflated to accommodate increasing volume (d). The lava collapse and breakout events in October 2014 and June 2015 were caused by the upper flow becoming unstable as the flow inflated above confining topography (e).

Phase	Dates	Activity	Effusion Rate ($m^3 s^{-1}$)	Flow Advance Rate ($m d^{-1}$)	Flow Front Advance Style	Mechanism Controlling Flow Advance
(1) Emplacement	24/12/2013 – 31/3/2014	Rapid emplacement of lava flow, PDCs	4.4 – 7[2]	30.4	Uniform	Yield strength of flow crust
(2a) Inflation	1/4/2014 – 13/6/2014	Flow inflation	3 – 4.4[2]	4.3	Breakout lobes	Yield strength of flow crust
(2b) Inflation	14/6/2014 – 29/9/2014	Flow inflation	3 – 4.4[2]	1.1	Breakout lobes	Yield strength of flow interior
(3) Collapse & Breakout 1	30/9/2014 – 1/6/2015	PDCs, growth of new lava lobe	1 – 2[3]	NA	NA	NA
(4) Collapse & Breakout 2	2/6/2015 – present[1]	PDCs, growth of new lava lobe	1 – 2[3]	NA	NA	NA

1: as of July 2016

2: from Ch. 5 (this dissertation) & this chapter, based on photogrammetry & satellite thermal images

3: this chapter, from satellite thermal images

Table 6.1. Phases of the Sinabung Eruption.

CHAPTER 7

CONCLUSIONS

This dissertation describes multiple types of silicic volcanic eruptions, focusing on recent events at Merapi and Sinabung volcanoes in Indonesia. I present new insights on these eruptions through a combination of satellite remote sensing (**Chapter 2** and **Chapter 6**), numerical modeling (**Chapter 3** and **Chapter 4**), and photogrammetry (**Chapter 5**) techniques. The primary contributions of this work relate to the variability of silicic volcanic eruptions, the utility of various remote sensing methods for documenting volcanic activity, factors controlling the generation of pyroclastic density currents (PDCs) during effusive eruptions, and the importance of small-scale processes in affecting eruption style.

7.1. A Tale of Two Eruptions: Summary of Study Sites and Techniques

The recent eruptions at Merapi and Sinabung demonstrate how silicic volcanism can vary between volcanoes located in similar tectonic settings (the Sunda Arc subduction zone, Figure 1.5) and of similar lava composition (basaltic andesite at Merapi and andesite at Sinabung). Effusive eruptions may form lava domes as at Merapi (**Chapter 2, Chapter 3,** and **Chapter 4**) or lava flows as at Sinabung (**Chapter 5** and **Chapter 6**) and eruptions may or may not include explosive phases – each style of activity presents its own unique hazards (**Chapter 1**). Therefore, it is important to place what I have learned about these eruptions in a broader context of global volcanic activity. Similar eruptive processes–particularly lava dome formation–are observed at many silicic

subduction zone volcanoes around the world (e.g. Nakada et al., 1999; Calder et al., 2002; Harris et al., 2004).

In **Chapter 2** I use satellite thermal remote sensing data to track the Merapi eruption in detail by estimating the extrusion rate and the activity style. I show that the extrusion rate is correlated to the occurrence of PDCs (Figure 2. 8) and that periods of increased dome growth are often followed by dome collapse (Figure 2.7). I apply these techniques to Sinabung in **Chapter 6** and show that building time series from nightly thermal images is a broadly applicable method of documenting prolonged eruptions. However, the extrusion rate and activity style methods I apply or develop in **Chapter 2** for Merapi were less effective at Sinabung due to the insulating properties of the lava flow.

In **Chapter 3** and **Chapter 4** I use a numerical model of magma ascent in a volcanic conduit to explain variations in eruption style that were observed at Merapi (e.g. Walter et al., 2007; Surono et al., 2012; Ratdomopurbo et al., 2013). I show that a variety of processes can affect the observed volcanic activity; these processes include dome growth and collapse, magma ascent from depth into a shallow storage system, and external tectonic events such as earthquakes. The identification and quantification of the effect of these processes becomes possible when the modeling is combined with detailed observations of eruptive activity.

In **Chapter 2**, **Chapter 3**, **Chapter 5**, and **Chapter 6** I apply multiple remote sensing and photogrammetry techniques to document and describe silicic volcanism and demonstrate their utility for scientific purposes. Satellite thermal remote sensing images from the low-spatial (1 km per pixel) high-temporal (2 images per night) MODIS

instrument can be used to generate daily time series of thermal radiance (Figure 6.4), time-averaged discharge rate (Figures 2.4, 2.8, 3.4, and 6.5), and activity style (Figure 2.5) in order to track an eruption in detail (**Chapter 2** and **Chapter 6**). These time series can be used to identify variations in eruptive activity and inform potential hazards. Higher spatial resolution images from the ASTER instrument (90 m per pixel) show details of eruptive deposits from domes, flows, and PDCs, which I use in combination with other observations to describe eruption processes (**Chapter 2** and **Chapter 6**). In **Chapter 5** I show that structure-from-motion (SfM) photogrammetry allows for the accurate, frequent, high-resolution, cost-effective, and safe measurement of active volcanic features. The generation of digital elevation models (DEMs) from SfM photogrammetry enables the estimation of volumes of erupted material and the measurement of changes in volcanic features between the creation of DEMs–both important results to obtain in order to describe effusive activity.

7.2. Pyroclastic Density Currents (PDCs)

The biggest hazard from effusive eruptions is PDCs. I show that these dangerous events can be triggered by a number of processes. At Merapi in 2006, the frequency of PDCs was correlated with the extrusion rate, though later in the eruption larger PDCs were generated when part of the crater wall collapsed (**Chapter 2** and **Chapter 3**). At Sinabung in early 2014, PDC frequency was correlated with effusion rate but also the rate of advance of the lava flow (**Chapter 5**). Later in the eruption, large, frequent PDCs occurred due to the collapse of instabilities generated by the flow inflating over ridges that initially confined the flow to a valley. The collapses occurred with no observable

increase in effusion rate or flow advance rate. **Chapter 5** and **Chapter 6** demonstrate the necessity of understanding all of these factors (effusion rate, flow advance rate, and underlying topography) in order to accurately assess the hazard posed by PDCs during an effusive eruption.

7.3. Small-Scale Processes

In **Chapter 4** I describe the potential effect of small-scale processes on controlling volcanic activity. Numerical modeling suggests that under the right conditions, heterogeneities in the magma, small variations in the dome height, or changes in the degassing characteristics of the volcano can have significant effects on eruption style and thus eruption hazards. The implications of these results suggest that some volcanic systems can exist in a type of critical state that promotes these effects, as may have been the case at Merapi in 2010, while other volcanoes may erupt under more stable conditions, as is likely for the prolonged eruption at Sinabung. Further investigation of these critical states is required to better understand the processes involved, but was outside the scope of this dissertation. While I show that these conditions were physically possible as an explanation for activity at Merapi, I leave unanswered questions regarding the duration of critical states, the effects of degassing on critical states, and processes aside from the ascent of new magma that may generate these conditions. Particularly, it will be important to learn if critical conditions can be generated through processes related to the long-term storage or steady eruption of magma in a volcanic system. In this scenario, a change in eruption style could occur without precursory seismic or

deformation signals related to magma ascent and may be triggered by external forces such as tectonic earthquakes.

7.4. Volcano-Tectonic Interactions

In **Chapter 3** I address the effect of a tectonic earthquake on an ongoing effusive eruption. However, this is only a small aspect of potential volcano-tectonic interactions. Linde & Sacks (1998) and Delle Donne et al. (2010) show that volcanic eruptions are statistically more likely to occur in the days immediately following a large earthquake. This correlation suggests that earthquakes can trigger eruptions in addition to increasing the intensity of an ongoing event as Walter et al. (2007), Harris & Ripepe (2007), Troll et al. (2012), and I describe at Merapi in 2006. Linde & Sacks (1998) and Delle Donne et al. (2010) also show that certain volcanoes are more likely to be triggered than others and that the proximity of a volcano to an epicenter does not necessarily increase the likelihood of a change in activity. Though many theories have been proposed (Manga & Brodsky, 2006), it remains unknown exactly how earthquakes affect magmatic systems and whether similar or different process are involved in triggering an eruption versus changing the eruption rate an ongoing eruption. Future investigation of these processes and a complete study to understand which volcanoes are most likely to be affected by tectonic events will greatly benefit both the understanding of volcano-tectonic interactions and regional hazard assessment.

7.5. Future Directions

My work in this dissertation treats the Merapi and Sinabung eruptions as individual events. In my future research, it is my goal to address these and other eruptions within a larger context. Both Merapi and Sinabung are located along the Sunda Volcanic Arc (Figure 1.5), and their activity may serve as insight into volcanic processes at other (less active) volcanoes along the arc. The different styles of their eruptions can be used to better understand arc-scale processes and the variability in volcanic activity that is observed in these tectonic settings.

One way to expand the scope of my investigations of silicic volcanic activity is to utilize the wealth of satellite data relevant to the observation of volcanic activity. In addition to thermal data that I have used and discussed in depth, satellite instruments can observe volcanic gas emissions (e.g. Carn et al., 2008), deformation (e.g. Chaussard et al., 2013), and topographic changes (e.g. Poland, 2014). Combining multiple data sources to observe different types of concurrent volcanic unrest will improve understanding of the relationships between observable volcanic signals and the processes that generate them (e.g. Pritchard et al., 2014). The global coverage of satellite data facilitates the observation of multiple volcanoes so that these processes can be compared along an entire volcanic arc or between different arcs. Increased utilization of multiple types of satellite remote sensing will improve understanding of both volcanic eruption processes and volcano-tectonic interactions.

A future application of SfM photogrammetry with great potential is multiple repeat observations of active volcanic features. I showed the ability of SfM to capture changes in a lava flow between two models in **Chapter 5**, but my field campaign was not

long enough to show further progression through time. Repeating SfM surveys for an extended period of time would produce a unique dataset that could show how lava flows or domes advance or grow. Repeat observations would also better capture the development and collapse of unstable regions to improve hazard assessment and estimation of PDC volumes. Related to the advancement of photogrammetric techniques is the advancement of unmanned aerial vehicle (UAV) technology. The use of UAVs to capture the photographs needed for SfM will provide new perspectives and increased detail in the photogrammetric models, making possible studies of volcanic features in unprecedented detail.

A final goal of my research is to make the techniques and tools I use and develop more accessible to the greater volcanological community. Many of the methods I described in this dissertation will be at their most effective in the hands of staff at volcano observatories. Real-time implementation of satellite and photogrammetric observations at an active or restless volcano can indicate increasing risk of PDCs and other possible changes in eruptive activity, as I demonstrated in **Chapter 2** and **Chapter 5**. Continued use and recording of data with the techniques I have described will also create a detailed resource for future study including numerical modeling that can improve understanding of different volcanic processes. The work I have presented here and aim to conduct in the future will improve the monitoring, understanding, and hazard assessment of silicic volcanic eruptions.

REFERENCES

Adams, B. M., Bauman, L. E., Bohnhoff, W. J., Dalbey, K. R., Ebeida, M. S., Eddy, J. P., Eldred, M. S., Hough, P. D., Hu, K. T., Jakeman, J. D., Stephens, J. A., Swiler, L. P., Vigil, D. M. & Wildey, T. M., 2014, Dakota, A Multilevel Parallel Object-Oriented Framework for Design Optimization, Parameter Estimation, Uncertainty Quantification, and Sensitivity Analysis: Version 6.0 User's Manual, Sandia Technical Report SAND2014-4633.

Albino, F., Smets, B., d'Oreye, N. & Kervyn, F., 2015, High-resolution TanDEM-X DEM: An accurate method to estimate lava flow volumes at Nyamulagira Volcano, D. R. Congo, Journal of Geophysical Research: Solid Earth 120, 4189-4207.

Ali, S. T. & Feigl, K. L., 2012, A new strategy for estimating geophysical parameters from InSAR data: Application to the Krafla central volcano in Iceland, Geochemistry Geophysics Geosystems 13, 6, Q06005.

Anderson, S. W., Fink, J. H. & Rose, W. I., 1995, Mount St. Helens and Santiaguito lava domes: The effect of short-term eruption rate on surface texture and degassing processes, Journal of Volcanology and Geothermal Research 69, 105-116.

Barclay, J., Carroll, M. R., Rutherford, M. J., Murphy M. D., Devine, J. D., Gardner, J., Sparks, R. S. J., 1998, Experimental phase equilibria constraints on pre-eruptive storage conditions of the Soufrière Hills magma, Geophys. Res. Lett., 25, 3437– 3440.

Besl, P. J. & McKay, N. D., 1992, A Method for Registration of 3-D Shapes, IEEE Transactions on Pattern Analysis and Machine Intelligence 14, 2, 239-256.

Bird, P., 2003, An updated digital model of plate boundaries, Geochemistry Geophysics Geosystems, 4(3):1027.

Brodsky, E. E., Sturtevant, B. & Kanamori, H., 1998, Earthquakes, volcanoes, and rectified diffusion, Journal of Geophysical Research 103, B10, 23827-23838.

Brown, R. J. & Andrews, G. D. M.Sigurdsson, H., ed., 2015, Encyclopedia of Volcanoes, Academic Press, Deposits of Pyroclastic Density Currents, pp. 631-648.

Bull, K. F. & Buurman, H., 2013, An overview of the 2009 eruption of Redoubt Volcano, Alaska, Journal of Volcanology and Geothermal Research 259, 2-15.

Calder, E. S., Luckett, R., Sparks, R. S. J. & Voight, B.Druitt, T. H. & Kokelaar, B. P., ed., 2002, The Eruption of Soufriere Hills Volcano, Montserrat, from 1995 to 1999, Geological Society, London, Memoirs, chapter Mechanisms of lava dome instability and generation of rockfalls and pyroclastic flows at Soufriere Hills Volcano, Montserrat, pp. 173-190.

Carn, S. A., Krueger, A. J., Arellano, S., Krotkov, N. A. & Yang, K., 2008, Daily monitoring of Ecuadorian volcanic degassing from space, Journal of Volcanology and Geothermal Research 176, 141-150.
Castruccio, A., Rust, A. C. & Sparks, R. S. J., 2013, Evolution of crust- and core-dominated lava flows using scaling analysis, Bulletin of Volcanology 75:681.

Charbonnier, S. J., Germa, A., Connor, C. B., Gertisser, R., Preece, K., Komorowski, J. C., Lavigne, F., Dixon, T. & Connor, L., 2013, Evaluation of the impact of the 2010 pyroclastic density currents at Merapi volcano from high-resolution satellite imagery, field investigations and numerical simulations, Journal of Volcanology and Geothermal Research 261, 295-315.

Charbonnier, S. J. & Gertisser, R., 2008, Field observations and surface characteristics of pristine block-and-ash flow deposits from the 2006 eruption of Merapi Volcano, Java, Indonesia, Journal of Volcanology and Geothermal Research 177, 971-982.

Chaussard, E. & Amelung, F., 2012, Precursory inflation of shallow magma reservoirs at west Sunda volcanoes detected by InSAR, Geophysical Research Letters 39, L21311.

Chaussard, E., Amelung, F. & Aoki, Y., 2013, Characterization of open and closed volcanic systems in Indonesia and Mexico using InSAR time series, Journal of Geophysical Research 118, 3957-3969.

Clarke, A. B., Stephens, S., Teasdale, R., Sparks, R. S. J. & Diller, K., 2007, Petrologic constraints on the decompression history of magma prior to Vulcanian explosions at the Soufriere Hills volcano, Montserrat, Journal of Volcanology and Geothermal Research 161, 261-274.

Cole, P. D., Neri, A. & Baxter, P. J.Sigurdsson, H., ed., 2015, Encyclopedia of Volcanoes, Academic Press, Hazards from Pyroclastic Density Currents, pp. 943-956.

Coppola, D., Piscopo, D., Laiolo, M., Cigolini, C., Donne, D. D. & Ripepe, M., 2012, Radiative heat power at Stromboli volcano during 2000-2011: Twelve years of MODIS observations, Journal of Volcanology and Geothermal Research 215-216, 48-60.

Costa, A., 2005, Viscosity of high crystal content melts: Dependence on solid fraction, Geophysical Research Letters 32, L22308.

Costa, F., Andreastuti, S., de Maisonneuve, C. B. & Pallister, J. S., 2013, Petrological insights into the storage conditions, and magmatic processes that yielded the centennial 2010 Merapi explosive eruption, Journal of Volcanology and Geothermal Research 261, 209-235.

De Beni, E., Behncke, B., Branca, S., Nicolosi, I., Carluccio, R., Caracciolo, F. D. & Chiappini, M., 2015, The continuing story of Etna's New Southeast Crater, 2012-2014: Evolution and volume calcuations based on field surveys and aerophtogrammetry, Journal of Volcanology and Geothermal Research 303, 175-186.

Deegan, F. M., Troll, V. R., Freda, C., Misiti, V., Chadwick, J. P., McLeod, C. L. & Davidson, J. P., 2010, Magma-Carbonate Interaction Processes and Associated CO2 Release at Merapi Volcano, Indonesia: Insights from Experimental Petrology, Journal of Petrology 51, 5, 1027-1051.

Degruyter, W., Bachmann, O., Burgisser, A. & Manga, M., 2012, The effects of outgassing on the transition between effusive and explosive silicic eruptions, Earth and Planetary Science Letters 349-350, 161-170.

Delgado, F. J., Pritchard, M. E., Lohman, R. & Naranjo, J. A., 2014, The 2011 Hudson volcano eruption , Southern Andes, Chile: Pre-eruptive inflation and hotspots observed with InSAR and thermal imagery, Bulletin of Volcanology 76, 815.

de' Michieli Vitturi, M., Clarke, A. B., Neri, A. & Voight, B., 2013, Extrusion cycles during dome-building eruptions, Earth and Planetary Science Letters 371-372, 37-48.

de' Michieli Vitturi, M., Clarke, A. B., Neri, A. & Voight, B., 2010, Transient effects of magma ascent dynamics along a geometrically variable dome-feeding conduit, Earth and Planetary Science Letters 295, 541-553.

de' Michieli Vitturi, M., Clarke, A. B., Neri, A. & Voight, B., 2008, Effects of conduit geometry on magma ascent dynamics in dome-forming eruptions, Earth and Planetary Science Letters 272, 567-578.

Diefenbach, A. K., Crider, J. G., Schilling, S. P. & Dzurisin, D., 2012, Rapid, low-cost photogrammetry to monitor volcanic eruptions: an example from Mount St. Helens, Washington, USA, Bulletin of Volcanology 74, 579-587.

Diller, K., Clarke, A. B., Voight, B. & Neri, A., 2006, Mechanisms of conduit plug formation: Implications for vulcanian explosions, Geophysical Research Letters 33, L20302.

Eichelberger, J. C., Carrigan, C. R., Westrich, H. R. & Price, R. H., 1986, Non-explosive silicic volcanism, Nature 323, 598-602.

Favalli, M., Fornaciai, A., Mazzarini, F., Harris, A., Neri, M., Behncke, B., Pareschi, M. T., Tarquini, S. & Boschi, E., 2010, Evolution of an active lava flow field using a multitemporal LIDAR acquisition, Journal of Geophysical Research 115, B11203.

Fink, J. H. & Griffiths, R. W., 1998, Morphology, eruption rates, and rheology of lava domes: Insights from laboratory models, Journal of Geophysical Research 103, B1, 527-545.

Fink, J. H., Malin, M. C. & Anderson, S. W., 1990, Intrusive and extrusive growth of the Mount St Helens lava dome, Nature 348, 435-437.
Gertisser, R., Charbonnier, S. J., Keller, J. & Quidelleur, X., 2012, The geological evolution of Merapi volcano, Central Java, Indonesia, Bulletin of Volcanology 74, 1213-1233.

Giberti, G., Jaupart, C. & Sartoris, G., 1992, Steady-state operation of Stromboli volcano, Italy: constraints on the feeding system, Bulletin of Volcanology 54, 535-541.

Gillespie, A., Rokugawa, S., Matsunaga, T., Cothern, J. S., Hook, S. & Kahle, A. B., 1998, A temperature and emissivity separation algorithm for Advanced Spaceborne Thermal Emission and Reflection Radiometer , ASTER images, IEEE Transactions of Geoscience and Remote Sensing 36, 4, 1113-1126.

Griffiths, R. W. & Fink, J. H., 1997, Solidifying Bingham extrusions: a model for the growth of silicic lava domes, Journal of Fluid Mechanics 347, 13-36.

Hammer, J. E., Cashman, K. V., Hoblitt, R. P. & Newman, S., 1999, Degassing and microlite crystallization during pre-climactic events of the 1991 eruption of Mt. Pinatubo, Philippines, Bulletin of Volcanology 60, 355-380.

Hammer, J. E., Cashman, K. V. & Voight, B., 2000, Magmatic processes revealed by textural and compositional trends in Merapi dome lavas, Journal of Volcanology and Geothermal Research 100, 165-192.

Harris, A. J. L. & Baloga, S. M., 2009, Lava discharge rates from satellite-measured heat flux, Geophysical Research Letters 36, L19302.

Harris, A. J. L., Blake, S., Rothery, D. A. & Stevens, N. F., 1997, A chronology of the 1991 to 1993 Mount Etna eruption using advanced very high resolution radiometer data: Implications for real-time thermal volcano monitoring, Journal of Geophysical Research 102, B4, 7985-8003.

Harris, A. J. L., Flynn, L., Matias, O. & Rose, W. I., 2002, The thermal stealth flows of Santiaguito dome, Guatemala: Implications for the cooling and emplacement of dacitic block-lava flows, GSA Bulletin 114, 5, 533-546.

Harris, A. J. L., Flynn, L., Matias, O., Rose, W. I. & Cornejo, J., 2004, The evolution of an active silicic lava flow field: an ETM+ perspective, Journal of Volcanology and Geothermal Research 135, 147-168.

Harris, A. J. L. & Ripepe, M., 2007, Regional earthquake as a trigger for enhances volcanic activty: Evidence from MODIS thermal data, Geophysical Research Letters 34, L02304.

Harris, A. J. L., Dehn, J., Calvari, S., 2007, Lava effusion rate definition and measurement: a review, Bulletin of Volcanology 70, 1-22,

Harris, A. J. L., Rose, W. I. & Flynn, L. P., 2003, Temporal Trends in lava dome extrusion at Santiaguito 1922-2000, Bulletin of Volcanology 65, 77-89.
Hess, K.-U. & Dingwell, D. B., 1996, Viscosities of hydrous leucogranitic melts: A non-Arrhenian model, American Mineralogist 81, 1297-1300.

James, M. R., Applegarth, L. J. & Pinkerton, H., 2012, Lava channel roofing, overflows, breaches and switching: insights from the 2008-2009 eruption of Mt. Etna, Bulletin of Volcanology 74, 107-117.

James, M. R., Pinkerton, H. & Applegarth, L. J., 2009, Detecting the development of active lava flow fields with a very-long-range terrestrial laser scanner and thermal imagery, Geophysical Research Letters 36, L22305.

James, M. R. & Robson, S., 2014, Sequential digital elevation models of active lava flows from ground-based stereo time-lapse imagery, ISPRS Journal of Photogrammetry and Remote Sensing 97, 160-170.

James, M. R. & Robson, S., 2012, Straightforward reconstruction of 3D surfaces and topography with a camera: Accuracy and geoscience application, Journal of Geophysical Research 117, F03017.

James, M. R. & Varley, N., 2012, Identification of structural controls in an active lava dome with high resolution DEMs: Volcán de Colima, Mexico, Geophysical Research Letters 39, L22303.

Jaupart, C. & Allègre, C. J., 1991, Gas content, eruption rate and instabilities of eruption regime in silicic volcanoes, Earth and Planetary Science Letters 102, 413-429.

Jay, J. A., Delgado, F. J., Torres, J. L., Pritchard, M. E., Macedo, O. & Aguilar, V., 2015, Deformation and seismicity near Sabancaya volcano, southern Peru, from 2002 to 2015, Geophysical Research Letters 42, 2780-2788.

Jeffery, A. J., Gertisser, R., Troll, V. R., Jolis, E. M., Dahren, B., Harris, C., Tindle, A. G., Preece, K., O'Driscoll, B., Humaida, H. & Chadwick, J. P., 2013, The pre-eruptive magma plumbing system of the 2007-2008 dome-forming eruption of Kelut volcano, East Java, Indonesia, Contributions to Mineralogy and Petrology 166, 275-308.

Komorowski, J.-C., Jenkins, S., Baxter, P. J., Picquout, A., Lavigne, F., Charbonnier, S. J., Gertisser, R., Preece, K., Cholik, N., Budi-Santoso, A. & Surono , 2013, Paroxysmal dome explosion during the Merapi 2010 eruption: Processes and facies relationships of associated high-energy pyroclastic density currents, Journal of Volcanology and Geothermal Research 261, 260-294.

Kozono, T. & Koyaguchi, T., 2012, Effects of gas escape and crystallization on the complexity of conduit flow dynamics during lava dome eruptions, Journal of Geophysical Research 117, B08204.

Kristiansen, N. I., Prata, A. J., Stohl, A. & Carn, S. A., 2015, Stratospheric volcanic ash emissions from the 13 February 2014 Kelut eruption, Geophysical Research Letters 42, 588-596.

La Spina, G., Burton, M. R. & de' Michieli Vitturi, M., 2015, Temperature evolution during magma ascent in basaltic effusive eruptions: A numerical application to Stromboli volcano, Earth and Planetary Science Letters 426, 89-100.

La Spina, G., de' Michieli Vitturi, M. & Romenski, E., 2014, A compressible single-temperature conservative two-phase model with phase transitions, International Journal for Numerical Methods in Fluids 76, 282-311.

Lejeune, A. M. & Richet, P., 1995, Rheology of crystal-bearing silicate melts: An experimental study at high viscosities, Journal of Geophysical Research 100, B3, 4215-4229.

Linde, A. T., Sacks, I. S., Johnson, M. J. S., Hill, D. P. & Bilham, R. G., 1994, Increased pressure from rising bubbles as a mechanism for remotely triggered seismicity, Nature 371, 408-410.

Llewellin, E. W., Mader, H. M. & Wilson, S. D. R., 2002, The constitutive equation and flow dynamics of bubbly magmas, Geophysical Research Letters 29, 24 23-1-23-4.

Llewellin, E. W. & Manga, M., 2005, Bubble suspension rheology and implications for conduit flow, Journal of Volcanology and Geothermal Research 143, 205-217.

Lyman, A. W., Koenig, E. & Fink, J. H., 2004, Predicting yield strengths and effusion rates of lava domes from morphology and underlying topography, Journal of Volcanology and Geothermal Research 129, 125-138.

Manga, M. & Brodsky, E., 2006, Seismic Triggering of Eruptions in the Far Field: Volcanoes and Geysers, Annual Reviews in Earth and Planetary Science 34, 263-291.

Massonnet, D. & Feigl, K. L., 1998, Radar interferometry and its application to changes in the earth's surface, Reviews of Geophysics 36, 4, 441-500.

Mastin, L. G., 2007, A user-friendly one-dimentional model for wet volcanic plumes, Geochemistry Geophysics Geosystems 8, 3, Q03014.

Mastin, L. G., 2002, Insights into volcanic conduit flow from an open-source numerical model, Geochemistry Geophysics Geosystems 3, 7.

Melnik, O. & Sparks, R. S. J.Druitt, T. H. & Kokelaar, B. P., ed., 2002, Dynamics of magma ascent and lava extrusion at Soufrière Hills Volcano, Montserrat, Geological Society, London, Memoirs, pp. 153-171.

Melnik, O. & Sparks, R. S. J., 1999, Nonlinear dynamics of lava dome extrusion, Nature 402, 37-41.

Micheletti, N., Chandler, J. H. & Lane, S. N., 2015, Investigation the geomorphological potential of freely available and acessible structure-from-motion photogrammetry using a smartphone, Earth Surface Processes and Landforms 40, 473-486.

Nakada, S., Shimizu, H. & Ohta, K., 1999, Overview of the 1990-1995 eruption at Unzen Volcano, Journal of Volcanology and Geothermal Research 89, 1-22.

Nakada, S., Yoshimoto, M., Maeno, F., Iguchi, M., Zaenudin, A. & Hendrasto, M., 2014, Recent two distinct eruptions at Sinabung and Kelud, Indonesia, Fall Meeting abstract V33E-06, American Geophysical Union.

Nakano, M., Kumagai, H., Miyakawa, K., Yamashina, T., Inoue, H., Ishida, M., Aoi, S., Morikawa, N. & Harjadi, P., 2006, Source estimates of the May 2006 Java earthquake, EOS Transactions 87, 45, 493-494.

Navarro-Ochoa, C., Gavilanes-Ruíz, J. C. & Cortés-Cortés, A., 2002, Movement and emplacement of lava flows at Volcán de Colima, México: November 1998-February 1999, Journal of Volcanology and Geothermal Research 117, 155-167.

Newhall, C. G., Bronto, S., Alloway, B., Banks, N. G., Bahar, I., del Marmol, M. A., Hadisantono, R. D., Holcomb, R. T., McGeehin, J., Miksic, J. N., Rubin, M., Sayudi, S. D., Sukhyar, R., Andreastuti, S., Tilling, R. I., Trimble, D. & Wirakusumah, A. D., 2000, 10,000 Years of explosive eruptions of Merapi Volcano, Central Java: archaeological and modern implications, Journal of Volcanology and Geothermal Research 100, 9-50.

Newhall, C. G. & Self, S., 1982, The Volcanic Explosivity Index , VEI: An Estimate of Explosive Magnitude for Historical Volcanism, Journal of Geophysical Research 87, C2, 1231-1238.

Ogburn, S. E., Loughlin, S. C. & Calder, E. S., 2015, The association of lava dome growth with major explosive activity , VEI?4: DomeHaz, a global dataset, Bulletin of Volcanology 77:40, 40.

Oppenheimer, C., 2011, Eruptions That Shook The World, Cambridge University Press, New York.

Oppenheimer, C., 1991, Lava Flow Cooling Estimated from Landsat Thematic Mapper Infrared Data: the Lonquimay Eruption , Chile, 1989, Journal of Geophysical Research 96, B13, 21,865-21,878.

Oppenheimer, C., Francis, P. W., Rothery, D. A., Carlton, R. W. T. & Glaze, L. S., 1993, Infrared Image Analysis of Volcanic Thermal Features: Láscar Volcano, Chile, 1984-1992, Journal of Geophysical Research 98, B3, 4269-4286.

Pallister, J. S., Schneider, D. J., Griswold, J. P., Keeler, R. H., Burton, W. C., Noyles, C., Newhall, C. G. & Ratdomopurbo, A., 2013a, Merapi 2010 eruption- Chronology and extrustion rates monitored with satellite radar and used in eruption forecasting, Journal of Volcanology and Geothermal Research 261, 144-152.

Pallister, J. S., Diefenbach, A. K., Burton, W. C., Muñoz, J., Griswold, J. P., Lara, L. E., Lowenstern, J. B. & Valenzuela, C. E., 2013b, The Chaitén rhyolite lava dome: Eruption sequence, lava dome volumes, rapid effusion rates and source of the rhyolite magma', Andean Geology 40, 2, 277-294.

Papale, P., 1999, 'Strain-induced magma fragmentation in explosive eruptions', Nature 397, 425-428.

Pieri, D. C. & Baloga, S. M., 1986, 'Eruption rate, area, and length relationships for some Hawaiian lava flows', Journal of Volcanology and Geothermal Research 30, 29-45.

Poland, M. P., 2014, Time-averaged discharge rate of subaerial lava at Kilauea Volcano, Hawai'i, measured from TanDEM-X interferometry: Implications for magma supply and storage during 2011-2013, Journal of Geophysical Research: Solid Earth 119, 5464-5481.

Prambada, O., Zaenudin, A., Iryanto, Santosa, I., Nakada, S. & Yoshimoto, M., 2010, Peta geologi gunungapi Sinabung, kabupaten tanah Karo, Sumatera Utara, Technical report, Kementerian Energi dan Sumberdaya Mineral, Badan Geologi, Pusat Vulkanologi dan Mitigasi Bencana Geologi.

Prata, A. J., 2009, Satellite detection of hazardous volcanic clouds and the risk to global air traffic, Natural Hazards 51, 303-324.

Preece, K., Barclay, J., Gertisser, R. & Herd, R. A., 2013, Textural and micro-petrological variations in the eruptive products of the 2006 dome-forming eruption of Merapi volcano, Indonesia: Implications for sub-surface processes, Journal of Volcanology and Geothermal Research 261, 98-120.

Pritchard, M. E., Henderson, S. T., Jay, J. A., Soler, V., Krzesni, D. A., Button, N. E., Welch, M. D., Semple, A. G., Glass, B., Sunagua, M., Minaya, E., Amigo, A. & Clavero, J., 2014, Reconnaissance earthquake studies at nine volcanic areas of the central Andes with coincident satellite thermal and InSAR observations, Journal of Volcanology and Geothermal Research 280, 90-103.

Ramsey, M. S. & Harris, A. J. L., 2013, Volcanology 2020: How will thermal remote sensing of volcanic surface activity evolve over the next decade?, Journal of Volcanology and Geothermal Research 249, 217-233.

Ratdomopurbo, A., Beauducel, F., Subandrio, J., Nandaka, I. M. A., Newhall, C. G., Suharna, Sayudi, D. S., Suparwaka, H. & Sunarta , 2013, Overview of the 2006 eruption of Mt. Merapi, Journal of Volcanology and Geothermal Research 261, 87-97.

Ratdomopurbo, A. & Poupinet, G., 2000, An overview of seismicity of Merapi volcano , Java, Indonesia, 1983-1994, Journal of Volcanology and Geothermal Research 100, 193-214.

Romenski, E., Drikakis, D. & Toro, E., 2010, Conservative Models and Numerical Methods for Compressible Two-Phase Flow, Journal of Scientific Computing 42, 68-95.

Rose, S. & Ramsey, M. S., 2009, The 2005 eruption of Kliuchevskoi volcano: Chronology and processes derived from ASTER spaceborne and field-based data, Journal of Volcanology and Geothermal Research 184, 367-380.

Ruprecht, P. & Bachmann, O., 2010, Pre-eruptive reheating during magma mixing at Quizapu volcano and the implications for the explosiveness of silicic arc volcanoes, Geology 38, 10, 919-922.

Siebert, L., Simkin, T. & Kimberly, P., 2010, Volcanoes of the World, University of California Press, Berkeley and Los Angeles, California & London, England.

Siswowidjoyo, S., Suryo, I. & Yokoyama, I., 1995, Magma eruption rates of Merapi volcano, Central Java, Indonesia during one century, 1890-1992, Bulletin of Volcanology 57, 111-116.

Smets, B., d'Oreye, N., Kervyn, M. & Kervyn, F., 2016, Gas piston activity of the Nyiragongo lava lake: First insights from a Stereographic Time-Lapse Camera system, Journal of African Earth Sciences.

Snavely, N., Seitz, S. M. & Szeliski, R., 2008, Modeling the World from Internet Photo Collections, International Journal of Computer Vision 80, 189-210.

Sparks, R. S. J., 1986, The dimensions and dynamics of volcanic eruption columns, Bulletin of Volcanology 48, 3-15.

Sparks, R. S. J., Young, S. R., Barclay, J., Calder, E. S., Cole, P., Darroux, B., Davies, M. A., Druitt, T. H., Harford, C., Herd, R., James, M., Lejeune, A. M., Loughlin, S., Norton, G., Skerrit, G., Stasiuk, M. V., Stevens, N. S., Toothill, J., Wadge, G. & Watts, R., 1998, Magma production and growth of the lava dome of the Soufriere Hills Volcano, Montserrat, West Indies: November 1995 to December 1997, Geophysical Research Letters 25, 18, 3421-3424.

Surono, S., Jousset, P., Pallister, J., Boichu, M., Buongiorno, M. F., Budisantoso, A., Costa, F., Andreastuti, S., Prata, F., Schneider, D., Clarisse, L., Humaida, H., Sumarti, S., Bignami, C., Griswold, J., Carn, S., Oppenheimer, C. & Lavigne, F., 2012, The 2010 explosive eruption of Java's Merapi volcano- A '100-year' event, Journal of Volcanology and Geothermal Research 241-242, 121-135.

Troll, V. R., Hilton, D. R., Jolis, E. M., Chadwick, J. P., Blythe, L. S., Deegan, F. M., Schwarzkopf, L. M. & Zimmer, M., 2012, Crustal CO2 liberation during the 2006 eruption and earthquake events at Merapi volcano, Indonesia, Geophysical Research Letters 39, L11302.

Tuffen, H., James, M. R., Castro, J. M. & Schipper, C. I., 2013, Exceptional mobility of an advancing rhyolitic obsidian flow at Cordón Caulle volcano in Chile, Nature Communications 4:2709.

Voight, B., Constantine, E. K., Siswowidjoyo, S. & Torley, R., 2000, Historical eruptions of Merapi Volcano, Central Java, Indonesia, 1768-1998, Journal of Volcanology and Geothermal Research 100, 69-138.

Voight, B. & Davis, M. J., 2000, Emplacement temperatures of the November 22, 1994 nuee ardente deposits, Merapi Volcano, Java, Journal of Volcanology and Geothermal Research 100, 371-377.

Walter, T. R., Wang, R., Zimmer, M., Grosser, H., Lühr, B. & Ratdomopurbo, A., 2007, Volcanic activity influenced by tectonic earthquakes: Static and dynamic stress triggering at Mt. Merapi, Geophysical Research Letters 34, L05304.

Wessels, R. L. & Griswold, J. P., 2014, High resolution satellite remote sensing of the 2013-2014 eruption of Sinabung Volcano, Sumatra, Indonesia, Fall Meeting 2014, abstract V41B-4804, American Geophysical Union.

Wheaton, J. M., Brasington, J., Darby, S. E. & Sear, D. A., 2010, Accounting for uncertainty in DEMs from repeat topographic surveys: improved sediment budgets, Earth Surface Processes and Landforms 35, 136-156.

Wolpert, R. L., Ogburn, S. E. & Calder, E. S., 2016, The longevity of lava dome eruptions, Journal of Geophysical Research: Solid Earth 121.

Woods, A. W., 1988, The fluid dynamics and thermodynamics of eruption columns, Bulletin of Volcanology 50, 3, 169-193.

Woods, A. W. & Koyaguchi, T., 1994, Transitions between explosive and effusive eruptions of silicic magmas, Nature 370, 641-644.

Wooster, M. J. & Kaneko, T., 1998, Satellite thermal analyses of lava dome effusion rates at Unzen Volcano, Japan, Journal of Geophysical Research 103, B9, 20,935-20,947.

Wooster, M. J., Kaneko, T., Nakada, S. & Shimizu, H., 2000, Discrimination of lava dome activity styles using satellite-derived thermal structures, Journal of Volcanology and Geothermal Research 102, 97-118.

Wright, R., Blake, S., Harris, A. J. L. & Rothery, D. A., 2001, A simple explanation for the space-based calculation of lava eruption rates, Earth and Planetary Science Letters 192, 223-233.

Wright, R., Cruz-Reyna, S. D. L., Harris, A. J. L., Flynn, L. & Gomez-Palacios, J. J., 2002, Infrared satellite monitoring at Popocatepetl: Explosions, exhalations, and cycles of dome growth, Journal of Geophysical Research 107 , 8, 2-16.

Wright, R., Flynn, L. P., Garbeil, H., Harris, A. J. L. & Pilger, E., 2004, MODVOLC: near-real-time thermal monitoring of global volcanism, Journal of Volcanology and Geothermal Research 135, 29-49.

APPENDIX A

DETAILED DESCRIPTION OF STRUCTURE-FROM-MOTION PROCESSING TECHNIQUES

This appendix describes the workflow of my photogrammetric analysis from the acquisition of photographs through calculation of the volumetric error. The sections are organized by the order in which I performed the analysis, starting with the creation of structure-from-motion point clouds and georeferencing (A.1), then point cloud alignments and cloud-to-cloud distances (A.2), digital surface modeling and analysis (A.3), volume calculation (A.4), and lastly the determination of the error (A.5).

A.1. Structure-from-Motion Point Clouds and Georeferencing (Agisoft Photoscan™ 1.0.4)

I performed the photogrammetric analysis using Agisoft Photoscan Pro™ software. After taking pictures in the field, the photos were loaded into Photoscan and grouped by date and camera used (Models 1-4, Table A.1). The photos were then aligned at medium accuracy with pair preselection disabled to begin building each model. In some cases poor visibility prevented these photo groups from completely aligning and the photos needed to be further divided into smaller sub-groups to make alignment possible. Six or seven control points on the volcano that were visible in the photos and identifiable in Google Earth™ were used for georeferencing (Figure A.1). I chose control points to be evenly distributed across the field of view and in locations unlikely to be affected by volcanic activity. The coordinates and elevation of each point were obtained from Google Earth™, which has a location error of $\sim 10^0$ - 10^1 meters. More accurately measured control points on Sinabung were not possible to obtain due to the ongoing eruption. The main source of error in this process was the difficulty of manually placing the control points in the precise location on both the oblique field photograph and Google Earth™

aerial image, which I estimated to be ~10^1 - 10^2 meters. The root mean square (RMS) errors of the control points for each Photoscan aligned and georeferenced model (Table A.1) are between 70 and 155 meters. I also used the control points to help align the sub-groups of photos to create complete models of the volcano.

Following the complete alignment and addition of spatial information for each model, I created the dense point cloud (medium quality and moderate depth filtering) and mesh (arbitrary surface type and medium face count) for each model. The mesh can be used to create a DEM or 3D model, so as a preliminary check I viewed each 3D model in Google Earth™ and found the alignment of my models to the same features in Google Earth™ was on the order of 10^1 - 10^2 meters. I exported the point clouds as .las files (binary point cloud format) for further alignment analysis. I used Global Mapper™ software to convert the 5 meter pre-eruption 2010 DEM of Sinabung shared with me by the Badan Informasi Geospasial and the Center for Volcanology and Geological Hazard Management (CVGHM) in Indonesia to a point cloud saved in .las format (no modifications were made; simply the DEM nodes become equally spaced points in the point cloud).

A.2. Point Cloud Alignment and Cloud To Cloud Distances (Cloud Compare)

I used the Cloud Compare open source software (http://www.danielgm.net/cc/) to improve the spatial accuracy of my models by aligning each post eruption point cloud to the pre-eruption point cloud. This alignment is a rigid-body transformation and was done manually using 7 to 8 control points identified in each cloud. I chose control points using the same method discussed in the previous section (that is selecting them in easily

identifiable areas that had not changed on account of the eruption). The RMS error, translation, rotation, and scale adjustment for each alignment are shown in Table A.2, the RMS errors ranged from 25 to 51 meters. I did not try to do a global alignment of all of the data because the lava flow occupies a large fraction of each of my models. The automated iterative closest point (ICP) method would have attempted to average the lava flow into the transformation and created large errors.

I also aligned Model 4 to Model 2 to observe changes that occurred in the flow between photo acquisition periods in the field (September 18th- September 22nd, 2014). I used the ICP method for this alignment, as the difference between the clouds is minor compared to the size of clouds. This relative size relationship preserves cloud-to-cloud distances caused by changes in the lava flow surface as they are generally not large or widespread enough in this case to significantly contribute to the averaging that occurs during ICP alignment of the dense point clouds. Small amounts of averaging may occur such that the distances represent low estimates, but this averaging error is minimal compared to the ICP alignment RMS error (Table A.2). In future applications that may have larger cloud-to-cloud changes, the averaging effect of ICP will need to be considered. The best method to avoid this effect is calculating the ICP alignment based only on unchanged regions of the model and then applying the transformation data to the model as a whole. Transformation data for out Model 4 to Model 2 alignment are shown in Table A.2.

To visualize the lava flow changes I calculated the cloud-to-cloud distances (absolute value) for both my point clouds to the pre-eruption cloud and also Model 4 to

Model 2. I show the Model 4 point cloud, with the points colored by cloud-to-cloud distance, in Figures 5.5 and 5.6.

A.3. Digital Surface Model Construction and Analysis (ArcGIS™ 10.2)

For each model, I converted the .las point cloud file to .csv and loaded the x, y, and z data for each point into ArcGIS™ as a point feature class in a new shapefile. I then used the "Topo-to-Raster" tool found under 3D Analyst Tools → Raster Interpolation in ArcToolbox™ (discretized thin plate spline) to create a DEM from each point cloud with a 5 meter cell spacing to compare with the pre-eruption DEM. I then used the "Raster Calculator" to subtract the pre-eruption DEM from my Model DEM and thus created a raster file of the elevation differences between my models and the pre-eruption DEM. I used the 3D analyst tool to create topographic profiles across each model and the pre-eruption DEM.

I next computed the volume, and it error, for each of my DEMs. I began by dividing each DEM into the flow and non-flow areas. I drew two shapefiles for each model: 1) the outline of the flow as determined by examining the hillshade of the DEM in ArcMap™ and the point cloud in Photoscan, and 2) the non-flow area of the DEM (Figure A.2). I drew the outer boundary of the non-flow region such that the point density of the corresponding point clouds (Figure 5.2) is ~> 0.01 points/m^2 (see Table A.1) for average point density for each model) and concavities in the boundary were minimized. I calculated the point density for each cloud using the LAStools "lasgrid" tool (http://rapidlasso.com/lastools/). I then used the "clip" tool in ArcGIS™ under Data Management Tools → Raster → Raster Processing in ArcToolbox™ to clip the elevation

difference file for each model to each of the shapefiles and exported them as separate .txt files using the "Raster-to-ASCII" tool found under "Conversion Tools" in ArcToolbox™. This created two sets of .txt files: 1) the vertical differences in the flow region representing the thickness of the lava flow for each pixel which I use for the volume calculation and 2) the vertical differences in the non-flow region which I use for the error calculation.

A.4. Volume Computation (Matlab™ 2014b)

I loaded the grid files of the elevation differences for each model into Matlab™. For the region containing the lava flow, I multiplied each elevation difference by the cell area (25 m^2) and summed them together to calculate the volume (Table 5.1). The surface area was determined by multiplying the number of cells within the flow region by the cell area. The long-term average eruption rate was calculated by dividing the volume by the time elapsed between the first day of photo acquisition (Sept 17, 2014 for Models 1 & 2; Sept 22, 2014 for Models 3 & 4) and the day effusion began (Dec 24, 2013).

A.5. Error Determination

I used the vertical differences in the non-flow region for each model to estimate the error, following approaches explained by Wheaton et al. (2010) and Albino et al. (2015). As in Wheaton et al. (2010), I know the x, y, and z errors for the points in my point cloud are of similar magnitude, but the horizontal component has a negligible contribution to the total volumetric error due to the relatively low and uniform slopes on the pyroclastic flow plain surrounding the lava flow. Horizontal errors have a greater

effect on error in high slope angle regions on the upper edifice, as slight horizontal misalignments can result in large vertical errors. This is shown in Figure A.3, where I plot the absolute value of the average vertical difference between my DEMs and the pre-eruption DEM in non-flow regions along each of the topographic profiles shown in Figure 5.5. These errors range from 10^0 - 10^1 meters and decrease downslope (from profile b to profile f). These errors are also distributed around a near-zero mean (Table A.3), showing no systematic error due to horizontal misalignment. Therefore, I followed Wheaton et al. (2010) and focus only on the vertical differences as the source of error in my volume calculation. Additionally, I calculated all errors relative to the pre-eruption DEM and do not account for error that may exist in that DEM. As all my volumes are relative differences between two DEMs, the absolute position error of the DEMs is not a significant concern.

To determine the error in my point cloud elevations, I followed the methodology of Albino et al. (2015). The approach is valid provided the set of vertical differences in the assumed unchanged area for each model shows a generally normal distribution about its mean and can be assumed to be spatially uniform. The standard deviation of these differences can then be used as the estimate for the vertical error (Wheaton et al, 2010; Albino et al., 2015). The mean vertical differences in the unchanged areas relative to the pre-eruption DEM are 4.9 m, -2.9 m, 1.4 m, and 0.4 m and the standard deviations are 14.8 m, 15.6 m, 10.6 m, and 8.2 m for Model 1, Model 2, Model 3, and Model 4, respectively (Table A.4). I subtracted these mean values from the set of vertical differences within the flow area (Figure A.2) to correct for any overall elevation bias and then recalculated the volume (Eq. 5.1). These results are shown in Table A.4. Histograms

of the non-adjusted vertical difference distributions are shown in Figure 5.3- all approximate a normal distribution. From Figure A.3 and Table A.4, it is clear Model 4 is my most accurate model. To calculate the final volumetric error, I multiplied the single standard deviation of the non-flow vertical differences by the surface area of the flow (Eq. 5.2). For Model 4, this error is a volume of 0.14×10^8 m^3, or ~14% of my calculated lava flow volume of 1.03×10^8 m^3 (Table A.4.). In terms of eruption rate, this error is ± 0.6 m^3 s^{-1}. Complete results for each model are shown in Table A.4.

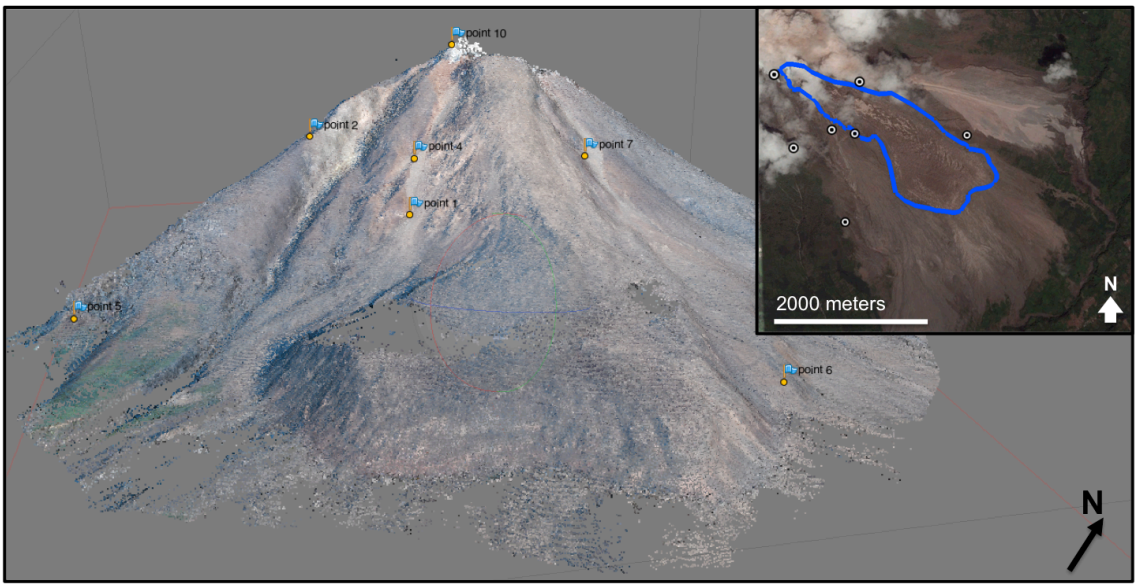

Figure A.1. Location of Control Points. The control points used to add spatial information to the point clouds for each model are shown on the dense point cloud for Model 4 in Agisoft Photoscan Pro™ (flags, main image) and in Google Earth™ (circles, inset). The RMS error of using these points to add spatial information to my models is shown in Table A.1. Blue outline in the inset image is the flow extent on September 22, 2014.

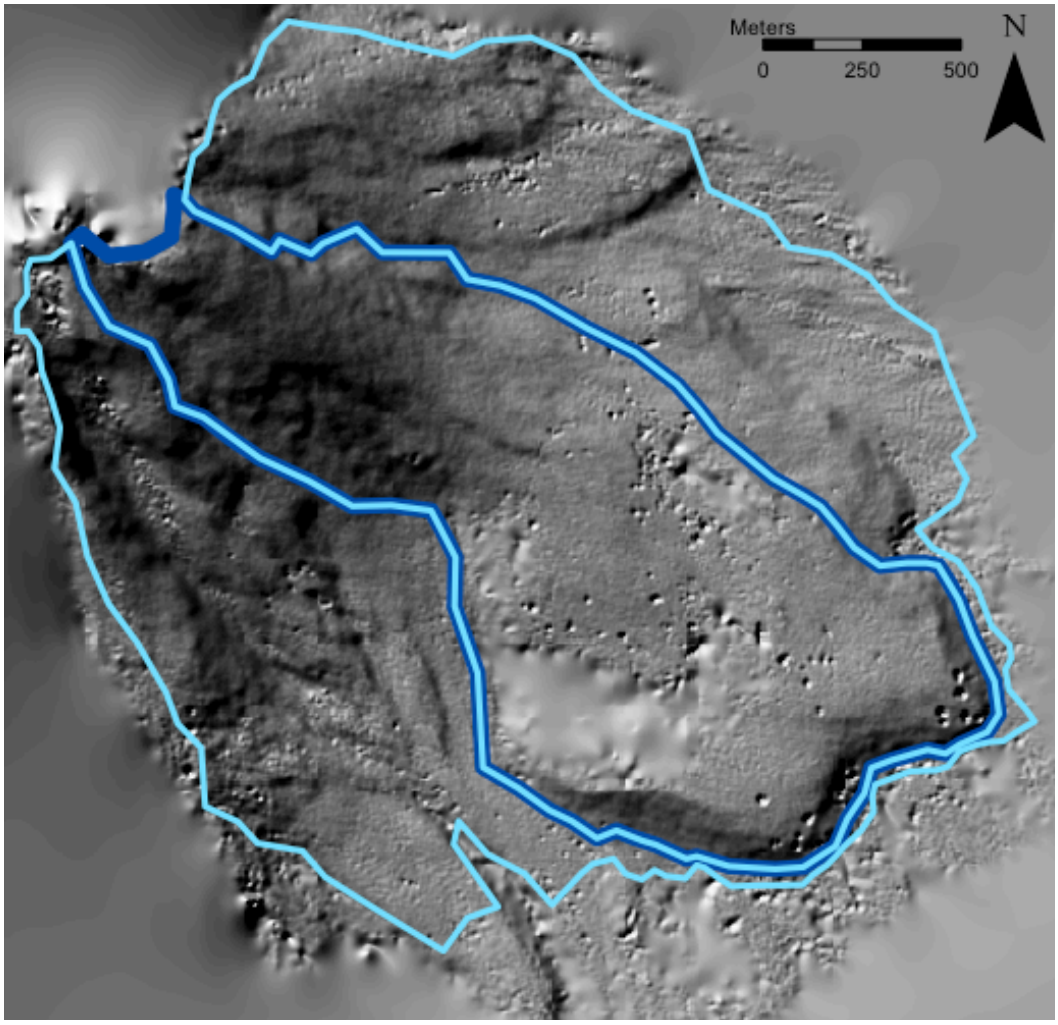

Figure A.2. Location of Flow and Non-Flow Regions. The DEM for Model 4 is shown with the shapefiles that outline the lava flow region (dark blue) and the non-flow (unchanged) region (light blue) that are used to clip the vertical difference grids into two separate files for calculation of the lava flow volume and estimate its error.

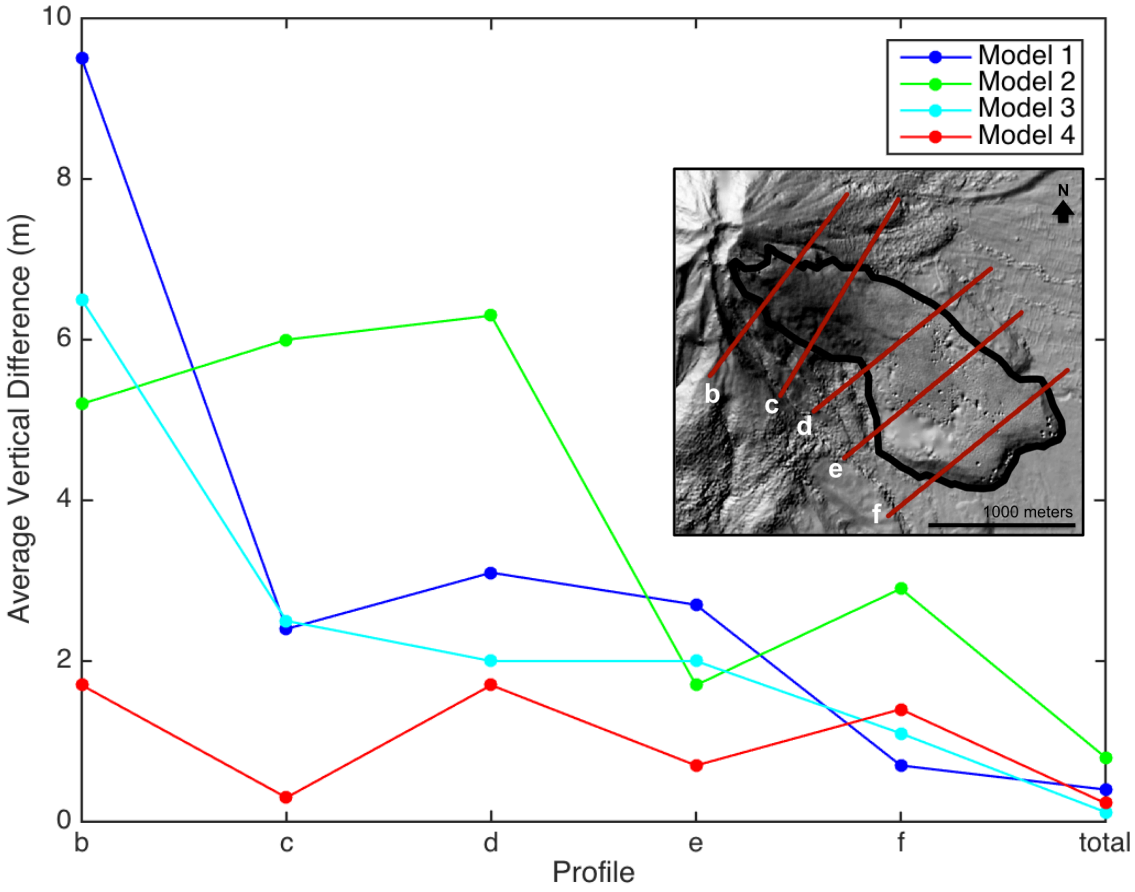

Figure A.3. Average Vertical Difference for Sinabung Profiles. I subtracted the pre-eruption DEM profile lines from the profile line elevations for each of my models and averaged the values for non-flow regions (located along the red lines but outside of the black flow outline in the inset image). This plot shows the absolute value of the average difference for each profile (b-f) for each model and the combined (total) average for each model from all of the profile differences. The average generally decreases down slope.

Model Name	**iPhone1**	**Loyc1**	**iPhone2**	**Loyc2**
Model Number	**1**	**2**	**3**	**4**
Camera	iPhone 5	Nikon D40X	iPhone 5	Nikon D40X
Date	Sept 17-18, 2014	Sept 17-18, 2014	Sept 22, 2014	Sept 22, 2014
Weather	Hazy & Cloudy	Hazy & Cloudy	Clear	Clear
# of Photos	27	39	54	54
DEM Resolution (meters/pixel)	5.27	3.37	6.51	3.84
Point Density (pts/m^2)	0.036	0.088	0.024	0.068
Dense Cloud Points	134,060	425,607	188,367	386,883
# Control Points	6	6	7	7
RMS Error (m)	94.0	153.1	73.6	82.8

Table A.1. Photogrammetric Model Data from Agisoft Photoscan Pro™. Basic information for each model including data from photo acquisition and Agisoft Photoscan Pro™ processing. The RMS error is the georeferencing error for the projection of the control points selected from Google Earth™ onto my 3D model in Agisoft Photoscan Pro™.

Model	**1**	**2**	**3**	**4**	**4**
Aligned to	Pre-eruption DEM	Pre-eruption DEM	Pre-eruption DEM	Pre-eruption DEM	Model 2
# Control Points	7	7	8	8	NA (used ICP)
RMS Error (m)	50.65	31.4	31.46	26.3	19.707
Scale	0.975	1.04	0.98	1.0016	1.0
Translation: x (m)	-131.3	-72.96	-86.2	-91.1	-110.5
Translation: y (m)	90.05	-138.2	22.6	-24.3	10.66
Translation: z (m)	24.1	30.5	13.8	25.2	8.24
Rotation: a (rad)	0.026	-0.043	0.014	-0.008	-0.014
Rotation: b (rad)	0.030	0.023	0.027	0.028	0.018
Rotation: g (rad)	-0.20	-0.007	0.011	-0.008	0.001

Table A.2. Cloud Compare Alignments. Data from the alignments performed in Cloud Compare to align my point clouds to the pre-eruption DEM and my Model 4 to Model 2. By saying the model is "aligned to" another point cloud, I mean the "aligned to" cloud is used as the reference and its position remains unchanged while the other cloud's position is adjusted. The alignment to the pre-eruption DEM was done manually using 7-8 control points located at unchanged locations on the Sinabung edifice. I allowed the scale to vary to improve the alignments to the pre-eruption DEM. I fixed the scale for the ICP alignment to prevent errors in my models from changing the scale after I had aligned the models to the pre-eruption DEM. Rotation values **a, b,** and **g** are the rotations in radians about the x, y, and z axes, respectively.

Model	**1**		**2**		**3**		**4**	
	Mean	±s	Mean	±s	Mean	±s	Mean	±s
Profile b (m)	9.5	5.2	5.2	8.6	6.5	5.6	1.7	5.5
Profile c (m)	-2.4	6.5	6.0	9.0	2.5	7.7	-0.3	5.9
Profile d (m)	-3.1	7.5	-6.3	7.3	-2.0	6.8	-1.7	2.5
Profile e (m)	-2.7	6.5	1.7	7.3	-2.0	7.2	-0.7	3.7
Profile f (m)	-0.7	4.4	-2.9	3.9	-1.1	3.4	-1.4	1.8
Total (m)	-0.4	7.85	-0.8	9.1	0.12	7.3	-0.23	4.7

Table A.3. Vertical Difference Errors Along Sinabung Profiles. The mean and standard deviation of vertical difference between each of my models and the pre-eruption DEM for non-flow regions is shown for each profile line. The totel is the mean and standard deviation for all non-flow profile data combined.

Model	**1**	**2**	**3**	**4**
Flow surface area (m^2)	1.83 x 10^6	1.86 x 10^6	1.81 x 10^6	1.74 x 10^6
Mean of vertical differences (m)	4.9	-3.0	1.40	0.44
Standard deviation (s) of vertical differences (m)	**14.8**	**15.6**	**10.7**	**8.2**
Non-adjusted volume (m^3)	1.23 x 10^8	1.05 x 10^8	1.12 x 10^8	1.03 x 10^8
Adjusted Volume (m^3) (used in Chapter 5)	**1.14 x 10^8**	**1.11 x 10^8**	**1.09 x 10^8**	**1.03 x 10^8**
Volume error (±s , m^3)	**0.27 x 10^8**	**0.29 x 10^8**	**0.19 x 10^8**	**0.14 x 10^8**
% Error	22.1%	27.6%	17.2%	13.8%
Volume range (m^3)	0.87 - 1.41 x 10^8	0.82 - 1.40 x 10^8	0.90 – 1.29 x 10^8	0.88 – 1.17 x 10^8
Eruption Rate (m^3/s)	4.9	4.7	4.7	4.4
Eruption rate error (,±s m^3/s)	1.2	1.3	0.8	0.6
Eruption rate range (m^3/s)	3.7 – 6.1	3.4 – 6.0	3.9 – 5.5	3.8 – 5.0

Table A.4. Volume Calculation and Error. Agisoft Photoscan Pro™ Error and volume calculation data from calculating the mean and standard deviation of the set of non-flow vertical differences for each model. The non-adjusted volume is the initial volume I calculated, prior to error correction. The adjusted volume is calculated after correcting the vertical differences by the mean of the vertical differences (i.e the elevation bias) (Eq. 5.1). The standard deviation of the vertical differences is used as the elevation error, and multiplied by the flow surface area to calculate the volume error (Eq. 5.2). Model 4 has the smallest error and is thus the model I use for presenting my results. However, all of the adjusted volumes are within the error of Model 4, demonstrating the consistency of my technique.